

DISSERTATION

Element-specific investigation of
4*f*-magnetism: graphene-covered
surface alloys and sandwich-molecular
nanowires

From the Faculty of Physics
the University of Duisburg-Essen
approved *dissertatio*
to obtain the degree
Dr. rer. nat.
from

M. Sc. Alexander Herman
from Markdorf

Advisor:
Prof. Dr. Heiko Wende
Co-advisor:
Prof. Dr. Thomas Michely

Duisburg, Germany
03.08.2022

UNIVERSITÄT
DUISBURG
ESSEN

Offen im Denken

DISSERTATION

Elementspezifische Untersuchungen
des Magnetismus der $4f$ -Metalle:
graphenbedeckte
Oberflächenlegierungen und
organometallische Nanodrähte

Der Fakultät für Physik
der Universität Duisburg-Essen
vorgelegte Dissertation
zur Erlangung des Grades
Dr. rer. nat.
von

Alexander Herman
aus Markdorf

Gutachter:
Prof. Dr. Heiko Wende
Zweitgutachter:
Prof. Dr. Thomas Michely

Duisburg, Deutschland
Tag der Disputation: 03.08.2022

Abstract

The precise control of the magnetic properties of $4f$ metals is not only crucial for many applications in our daily lives, like heavy-duty permanent magnets in generators and electric motors, but is also the key to realizing future nanosized and energy-efficient spintronic devices. In this work, we will contribute to this field with two different approaches.

By incorporating $4f$ metals into a long-range ordered two-dimensional iridium surface alloy, we provide a proof-of-concept system, that allows us to tailor its magnetic properties by graphene adsorption. Our combined theoretical and experimental approach reveals, that graphene adsorption selectively lifts the $4f$ atoms out of the surface alloy, leading to a drastic increase in electronic and magnetic anisotropy, which we studied by X-ray absorption spectroscopy and X-ray magnetic circular dichroic measurements. A combined theoretical approach based on ligand field multiplet theory and *ab initio* calculations allows us to precisely model these systems and provide a deeper understanding of the changes in the magnetic and electronic properties. Including a whole set of $4f$ metals into this system allows us to generalize the graphene-induced selective skyhook effect and provides us insides into the changes with changing $4f$ occupation. This set of electronically similar, but magnetically tunable $4f$ graphene-covered surface alloys could be used as substrates for future spintronic applications.

Such organometallic spintronic components, namely europium cyclooctatetraene nanowires, are studied in the second part. By probing the electronic and magnetic properties of these wires on various substrates, we revealed the influence of global orientation, electronic doping, and interaction with a magnetic substrate on these systems, especially the magnetic susceptibility and the ferromagnetic order. The variation of the organic ligands, as well as the $4f$ metal, provides further insides. The "zero-dimensional" thulium cyclooctatetraene compounds however approach the limit of electronic and magnetic anisotropy and show strong evidence of significant interaction of the $4f$ shell with its local surrounding.

Kurzzusammenfassung

Die präzise Kontrolle der magnetischen Eigenschaften von $4f$ -Metallen ist nicht nur entscheidend für viele Anwendungen des täglichen Lebens, wie z.B. in Hochleistungsdauermagneten in Generatoren und Elektromotoren, sondern auch der Schlüssel zur Realisierung künftiger nanoskaliger und damit energieeffizienter spintronischer Bauelemente. Zu diesem Themenkomplex möchten wir in dieser Arbeit mit zwei unterschiedlichen Ansätzen beitragen.

Durch die Synthese von $4f$ -Iridium-Oberflächenlegierungen etablieren wir ein Prototypsystem, welches uns die gezielte Manipulation der magnetischen Eigenschaften durch Graphen-Adsorption ermöglicht. Unser kombinierter theoretischer und experimenteller Ansatz enthüllt, dass Graphen-Adsorption die $4f$ -Atome selektiv aus der Oberflächenlegierung herauszieht, was zu einer drastischen Erhöhung der elektronischen und magnetischen Anisotropie führt, die wir durch Röntgenabsorptionsspektroskopie und röntgenmagnetische zirkular dichroitische Messungen bestätigen können. Durch unseren kombinierten theoretischen Ansatz, der auf der Ligandenfeld-Multiplett-Theorie und *ab initio*-Berechnungen basiert, ist es uns möglich, diese Systeme präzise zu modellieren und ein tieferes Verständnis der Manipulation der magnetischen und elektronischen Eigenschaften zu gewinnen. Die Integration weiterer $4f$ -Metalle in dieses System ermöglicht es uns, den "graphene-induced selective skyhook" Effekt zu verallgemeinern. Desweiteren ermöglicht es die Veränderungen basierend auf der $4f$ -Besetzung genauer zu studieren. Mit diesem Set von elektronisch vergleichbaren, aber magnetisch variablen, graphenbedeckten $4f$ Oberflächenlegierungen bieten wir eine neue Klasse an Substraten für zukünftige spintronische Anwendungen.

Die relevanten Bauteile für solch eine Anwendung, in unserem Fall Europium-Cyclooctatetraen Nanodrähte, werden im zweiten Teil dieser Arbeit untersucht. Wir analysieren die elektronischen und magnetischen Eigenschaften dieser Nanodrähte auf verschiedenen Substraten und können dadurch den Einfluss der globalen Orientierung, der elektronischen Dotierung und der Wechselwirkung mit einem magnetischen Substrat auf diese untersuchen. Einen Fokus legen wir hierbei auf die magnetische Suszeptibilität und die ferromagnetische Ordnung. Die Variation der organischen Liganden, sowie des $4f$ Metalls, liefert weitere Erkenntnisse, wohingegen sich die "nulldimensionalen" Thulium-Cyclooctatetraen-Verbindungen der Grenze der elektronischen und magnetischen Anisotropie nähern und damit Hinweise auf eine signifikante Wechselwirkung der $4f$ -Schale mit ihrer lokalen Umgebung liefern.

Contents

Abstract	i
1. Introduction	1
2. Fundamentals	3
2.1. Graphene on Iridium(111)	3
2.2. Magnetic Properties of 4f-metals	7
2.3. 4f Surface Alloys	11
2.4. 4f-Based Organometallic Spintronics	14
3. Experimental and Computational Techniques and Setups	23
3.1. Low-Energy Electron Diffraction	23
3.2. Scanning Tunnelling Microscopy	24
3.3. X-ray Absorption Spectroscopy	24
3.4. X-ray Magnetic Circular and Linear Dichroism	25
3.5. X-ray Photoelectron Spectroscopy	27
3.6. Multiplet Calculation	29
3.7. Experimental Setups	34
4. Graphene-Covered 4f Surface Alloys	37
4.1. Synthesis of Graphene-Covered 4f Surface Alloys	37
4.2. <i>Ab Initio</i> Calculations of the Graphene-Covered Dysprosium Surface Alloy	43
4.3. Magnetic and Electronic Properties of the Graphene-Covered Dysprosium Surface Alloy	48
4.4. Variation of the 4f Metal - a Systematic Study	57
4.5. Conclusion and Outlook	66
5. Nanowires and Organometallic Compounds	69
5.1. EuCot Nanowires on Gr/Ir(110)	69
5.2. Variation of Substrate and Ligand for EuCot Nanowires	75
5.3. Thulium-Cyclooctatetraene Compounds	85
5.4. Conclusion and Outlook	91
6. Summary	93

A. Scientific Appendix	95
A.1. Graphene on Ir(110)	95
A.2. X-ray Induced Oxidation of <i>4f</i> Elements	98
A.3. XPS Examination of the Chemical Structure of PEGMUA Coated Gold Nanoparticles	100
A.4. Spin Crossover in a Cobalt Complex on Ag(111)	102
B. List of Beamtimes and Contributors	105
C. List of Publications	106
D. Conference Contributions	107
E. Danksagung	108
F. Erlahrung gema Promotionsordnung	109
Bibliography	110

1. Introduction

Magnetism has inspired and influenced mankind for hundreds of years. Starting from early utilization as compass needles to countless modern applications, magnetic materials have become an integral part of our today's society. With the rise of electromobility and the need for energy-efficient computing, the interest in $4f$ elements has risen over the last decades. While one tries to minimize the use of rare-earth elements in regular appliances due to the high costs and the lack of availability [1], they are indispensable for high-end systems, like heavy-duty permanent magnets [2] and future spintronic applications [3].

Their special character is not mainly based on the highest magnetic moments of all stable elements, which they can provide (Dy and Ho), but rather due to their large magnetic anisotropy, which allows high coercive fields in permanent magnets [4] and stable nanosized qubits, down to single-atom level [5]. Such nanosized qubits and other spintronic devices like spin-filters could be the key to future energy-efficient and high-performing computers [6]. The precise manipulation of the anisotropy in $4f$ systems and the understanding of the underlying mechanisms are central for further development.

One approach to manipulating the magnetic properties of $4f$ metals is tailoring its ligand field by organic ligands e.g. in single-molecule magnets [7]. By the variation of the ligands, one can influence the magnetic properties of the central atom. By inducing bistability of the magnetic moment, a spin-qubit can be realised, which allows high-density data storage [8]. Extending this principle to 1D systems, organometallic nanowires can be realized [9], which are proposed to be effective spin filters [10]. Such spin filters could allow the realization of nanosized logic gates [11].

Organic ligands are not the only approach to controlling the magnetic properties of $4f$ metals. Utilizing the symmetry of adsorption sites on surfaces allows to realise stable single-atom magnet arrays [5, 12], exhibiting theoretical data densities around 100 times larger than the one of today's regular hard drive data storage devices. The interaction with the surface, in general, plays a prominent role in all future spintronic applications [13]. It not only functions as a substrate but can strongly influence the magnetic and electronic properties of adsorbed systems [14]. Controlling the magnetic properties can be as important as the decoupling of the adsorbed systems from a metallic substrate, to sustain long-living quantum states [15]. In this work, we want to contribute to both topics by introducing a new set of magnetically anisotropic graphene-covered surface alloys as well as by investigating various organometallic systems on different substrates.

In chapter 2 we provide the scientific background for our work, focusing on the graphene on Ir(111) system, which is the base for our graphene-covered surface alloys, and other $4f$ surface alloys. The theoretical background of $4f$ magnetism is provided to give a basic understanding of its magnetism, anisotropy and the influence of the ligand field. An introduction to low-dimensional $4f$ organometallic compounds is given in order to put our organometallic samples into context as well as give an idea of possible applications of novel substrates.

In chapter 3 we introduce the methods and setups used for our investigations. Starting with surface-sensitive methods for structural analysis, namely low-energy electron diffraction and scanning tunnelling microscopy, followed by our element-specific synchrotron-based X-ray absorption spectroscopy techniques, including X-ray magnetic circular dichroism, and finally X-ray photoelectron spectroscopy. Accompanied by a detailed introduction to our multiplet calculations, based on the multiX code [16]. Simple examples visualize the effect of different ligand fields on the multiplet and fine structure. For the experimental setups, a home lab setup and a synchrotron endstation are described exemplarily.

The scientific contribution starts with chapter 4. We investigate the synthesis and the structure of the newly introduced $4f$ surface alloys and compare these findings to *ab initio* calculations. By probing $4f$ surface alloys on Ir(111) and their graphene-covered counterparts, direct comparison and the exposure of the influence of the graphene adsorption on the electronic and magnetic properties of the $4f$ metals is possible. We reveal a distinct lifting of the $4f$ atoms out of the surface alloy upon graphene adsorption, which we call the graphene-induced selective skyhook effect [17]. By synchrotron-based measurements, we uncover that the selective skyhook effect induces a strong electronic and magnetic anisotropy in the $4f$ metal. By including a number of different $4f$ metals into this system, the selective skyhook effect can be generalized and systematic changes within the $4f$ occupation are uncovered.

In chapter 5, the focus changed to organometallic systems. Europium-cyclooctatetraene nanowires proved to be ferromagnetic on graphene on Ir(111) [18] and are proposed spin filters [10]. In this work, we try to improve their magnetic properties by variation of the substrate, inducing global orientation and manipulating the doping level, and by variation of the organic ligand. Further, we investigated thulium based compounds, which display highly anisotropic behaviour and give us insights into the interactions between the $4f$ electrons and the ligand field.

Our element-specific experimental approach combined with *ab initio* and multiplet calculations gives deeper insight into the properties and the manipulation of $4f$ magnetism and with a set of graphene-covered surface alloys with electronically similar, but magnetically tunable properties, we provide substrates for future spintronic applications. This all will be summarised in chapter 6.

In the appendix, all the other projects to which I contributed during this work are briefly introduced and presented.

2. Fundamentals

As introduced in chapter 1, the electronic and magnetic properties of $4f$ -metals incorporated in surfaces, interacting with graphene, and in organometallic compounds are investigated in this work. To provide a proper background, the fundamentals are described in this chapter, starting with the iridium(111) surface, mainly used as a substrate in this work, and the properties of graphene on iridium(111). Further, the properties of the lanthanides, or $4f$ -elements, are described, with a focus on their magnetic properties. Recently discovered $4f$ -surface alloys on various metal surfaces will be introduced and an overview on organometallic compounds on single-crystal surfaces will be given, which are promising to contribute to future spintronic applications.

2.1. Graphene on Iridium(111)

With the rise of graphene (Gr) [19, 20], rewarded with the Nobel prize in 2010 [21], the development and application of 2D materials moved into the focus of the scientific community. Thereby, the outstanding mechanical and electronic properties of graphene are of special interest [22, 23].

In this work, we use Gr as a substrate and investigate its interaction with surface alloys. In order to conduct such measurements, Gr has to be supported by a substrate. Gr has been intensively studied on a variety of metal substrates, as they allow scale-able growth of high quality Gr. However the intrinsic properties of Gr are influenced through the interaction with the substrate [24]. A system, which combines the ability of large-scale single-crystalline Gr growth without strong distortion of the Gr's properties is Gr on iridium(111) (Gr/Ir(111)) [25, 26], which properties will be discussed in detail below.

Atomic structure of graphene on Ir(111)

As suggested above, Gr/Ir(111) combines a number of useful properties. Starting with the growth process, the catalytic surface of Ir(111), enabled by the partially open d -shell, allows self-limiting chemical vapour deposition (CVD) growth of Gr on Ir(111) by using hydrocarbon precursor molecules [27]. While the Gr growth on weakly interacting metal surfaces like Cu(111) [28] and Pt(111) [29] leads to multiple domains, strongly interacting substrates

like Ru(0001) [30] lead to strong interaction and corrugation and a loss of the Gr free-standing properties [31].

Gr/Ir(111) combines single-crystal Gr without rotated domains while mostly keeping the graphene free-standing properties. The structure of Gr/Ir(111) is presented in Fig. 2-1.

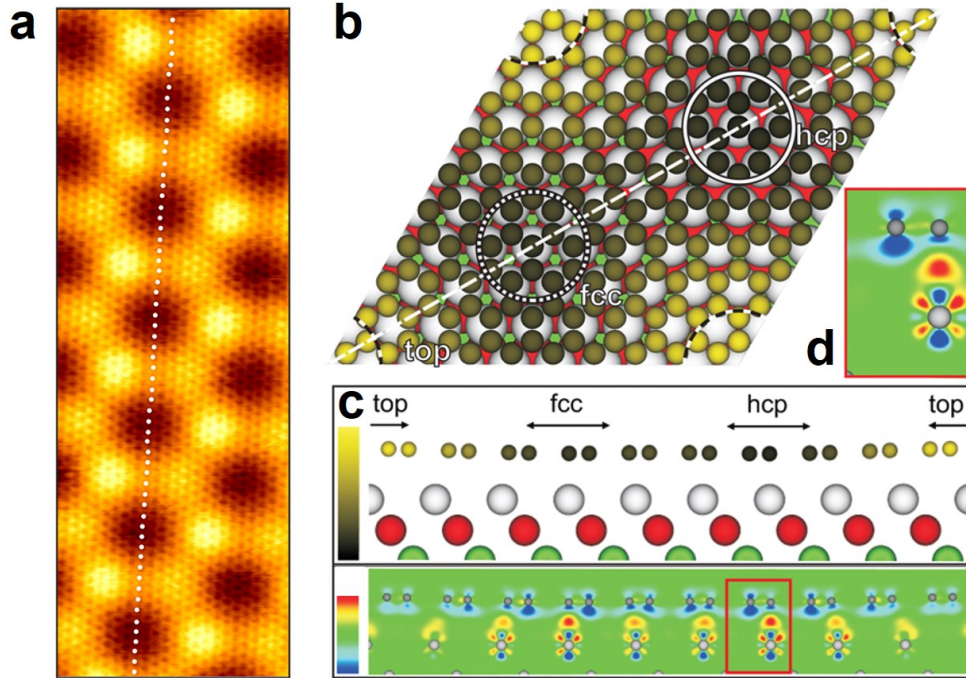


Figure 2-1.: **a** STM topograph of Gr/Ir(111) ($15 \text{ nm} \times 5.4 \text{ nm}$). An atomic carbon row is indicated by white dots. **b** Top view of the relaxed DFT structure of Gr/Ir(111). Regions of high-symmetry stacking are highlighted. **c** Side view of DFT structure. Cut indicated in **b**. The color code indicating the height over the Ir(111) substrates ranges from 3.20 \AA (dark) to 3.65 \AA (light). Charge density difference plot through the cut is depicted below. The color scale ranges from $\Delta\rho = -0.0138e \text{ \AA}^{-3}$ (blue) to $\Delta\rho = 0.013e \text{ \AA}^{-3}$ (red). The red square indicates the zoom-in shown in **d**. **a** adapted from [32], **b-d** from [33].

Fig. 2-1 **a** presents a STM topograph of Gr/Ir(111). On the one hand, the high quality of the Gr is visible, indicated by the large defect-free region. On the other hand, the moiré pattern of Gr/Ir(111) is clearly visible. The moiré results from the incommensurate superstructure of (10.32×10.32) Gr unit cells on (9.32×9.32) Ir unit cells [32], which leads to a height corrugation of the different stacking regions. A deeper insight into this structure is given by DFT calculations, as presented in Fig. 2-1 **b-d**. To reduce the needed calculation time to an acceptable level, a commensurate supercell of (10×10) Gr unit cells on (9×9) Ir unit cells is utilised. Fig. 2-1 **b** presents a relaxed structure of this supercell. The high-symmetry stacking areas are indicated. The fcc and hcp areas are more strongly bound

and thus closer to the Ir substrate, whereas the top areas are further away. It is important to note, that STM topographs, depending on the tunnelling parameters, are more likely to show an contrast-inverted moiré, in which the top area appears lowest, while the fcc region appears highest [32], which is also present in Fig. **2-1 a**. A more detailed view of the height distribution is provided in the cut through the supercell in Fig. **2-1 c**. At the top region, the carbon atoms are up to 3.65 Å above the Ir surface, while this number decreases to 3.20 Å at the hcp region. On average, Gr/Ir(111) has a height of 3.4 Å which is similar to the lattice parameter of bulk graphite and in strong contrast to the situation on other metals, e.g. Gr/Ni(111) with about 2.1 Å [34]. The reason for this big difference is the type of interaction. While Gr is chemically bound to Ni(111), Gr/Ir(111) is mostly physisorbed with a small chemical modulation of the binding [33]. This can be seen in the CDD plot provided in Fig. **2-1 c**. While the change in the charge density varies over the different stacking areas, no chemical binding occurs between the C atom and the Ir substrate. The strongest interaction at the hcp area is highlighted in Fig. **2-1 d**. But even there, no direct chemical binding is indicated. Another observation is the charge depletion around the C atoms, which is present throughout the whole supercell. This leads to the slight p-doping of Gr/Ir(111), which will be discussed in more detail below.

Electronic properties and intercalation of Gr/Ir(111)

Gr/Ir(111) is a well-ordered system which is mostly physisorbed, indicating that Gr's properties are close to free-standing. One of the unique properties of free-standing graphene is the Dirac cone at the K point with the Dirac point exactly at the Fermi level, making it a gapless semiconductor [35]. This property is distorted by interaction with a substrate and can be specifically manipulated. Strongly interacting substrates even lead to a vanishing of the Dirac cone, as the strong interaction destroys the pure π -band character of the Gr [36, 37].

Fig. **2-2 a** shows an angle-resolved photoemission spectroscopy (ARPES) spectrum around the K -point of Gr/Ir(111). The Dirac cone is clearly visible as well as a small shift to lower binding energies, indicating a doping level of $E_B = -0.067$ eV [38]. This is very close to the value of free-standing graphene. An additional feature, caused by the adsorption of Gr on Ir(111) are the mini gaps visible at 0.7 eV. These are caused by the Dirac cone replicas due to the moiré lattice of Gr/Ir(111) [26].

One way to manipulate the properties of this "quasi free-standing graphene" is to change the interaction with the substrate by intercalation. Due to the low reactivity of Gr, it is energetically favourable for many species to intercalate in between the Gr and the metal substrate. Intercalation may be used for several applications, like decoupling the Gr from its substrate [39, 40], bringing it in contact with a magnetic material [41, 42, 43], or patterning the graphene in a self-organized way [44]. In this thesis, we will focus on the doping of graphene with electrons and holes by intercalation.

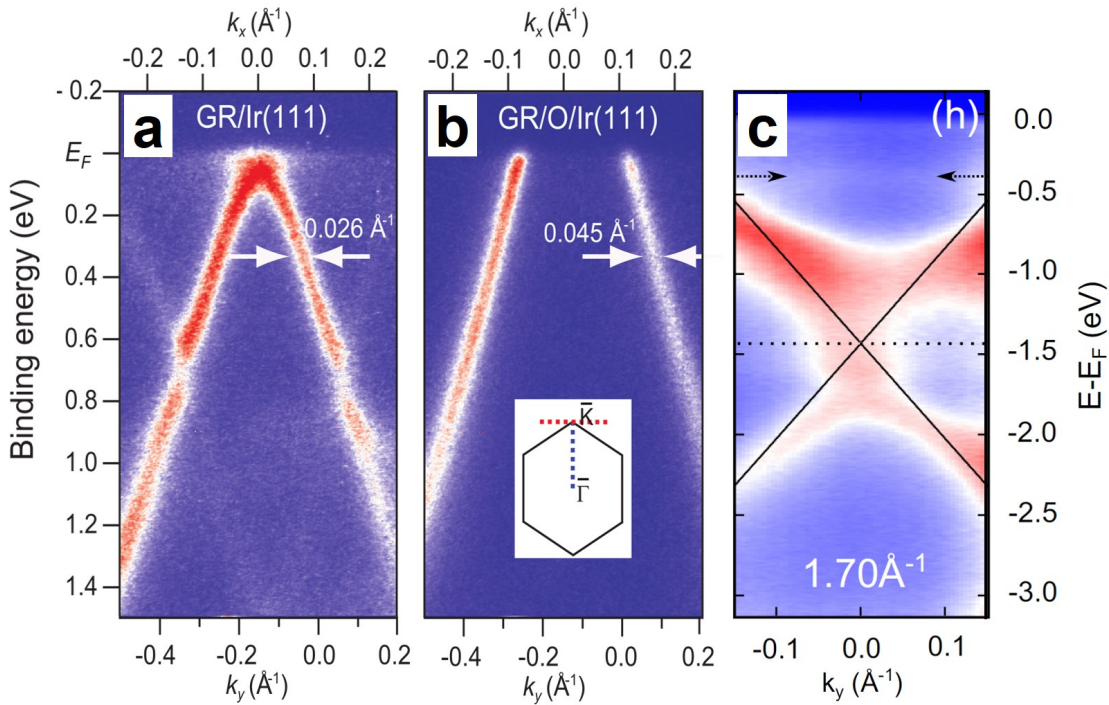


Figure 2-2.: ARPES measurements of the spectral function along a line orthogonal to the $\bar{\Gamma}\bar{K}$ direction, as indicated by the red dotted line in **b**. Dispersion of **a** Gr/Ir(111), **b** O intercalated Gr/Ir(111), and **c** Eu intercalated Gr/Ir(111). **a**, **b** adapted from [38], **c** from [45].

In Fig. 2-2 **b** the effect of O intercalation on the electronic structure of Gr/Ir(111) is presented. The Dirac point is shifted out of the occupied states and can therefore not be detected by ARPES measurements anymore. By extrapolation, the Dirac point and therefore the doping level can be determined as $E_B = -0.64$ eV [38]. This result shows on the one hand, that the Gr is strongly p-doped and on the other hand, that the Dirac cone and the electronic structure of the Gr are still intact [46]. For Eu intercalation, as presented in Fig. 2-2 **c**, a strong n-doping can be detected, shifting the Dirac point to $E_B = 1.43$ eV as indicated by the dotted line. The much worse experimental resolution can be explained by the home-lab approach in Ref. [45], whereas synchrotron-based measurements have been conducted in Ref. [38].

A number of different species can be used to tune the doping level of Gr/Ir(111) by intercalation. An overview is given in Ref. [47]. Of special interest is the intercalation with Li, as it allows a continuous shift of the doping level due to the lack of phase separation during the intercalation [48].

To summarize, Ir(111) is a substrate, that allows the growth of large-scale single-crystal Gr under UHV conditions. As it is mostly physisorbed, its properties are close to free-standing graphene, which is also valid for the doping level. The Gr doping level, as well as

other properties, can be tuned over a wide range by intercalation, which does not affect the structural integrity of the Gr layer. These properties make Gr/Ir(111) an ideal substrate for fundamental research on the topic of spintronics.

2.2. Magnetic Properties of 4f-metals

In this section, we would like to give a brief introduction into 4f magnetism. Starting with a general definition of 4f metals and magnetic moments, the focus shifts to the magnetic properties of 4f elements, especially their anisotropy, which will be presented by exemplary systems.

Before we discuss the magnetic properties of the 4f-metals, a brief definition of a 4f-metal is given. The 4f-metals or lanthanides are those elements, that have a partly filled 4f-shell, which includes the elements from Ce ($n = 58$) to Lu ($n = 71$). Some sources include La ($n = 57$) in the lanthanides, although its 4f-shell is not occupied [49]. Another term, sometimes used as a synonym is rare-earth elements. This group, based on similar chemical properties, includes the lanthanides with La as well as Sc ($n = 21$) and Y ($n = 39$). As the magnetic properties of the 4f-electrons are of special interest, we will focus on the 4f-metals in the following.

The most common application of 4f-metals in our daily life is heavy-duty permanent magnets, employed in e.g. generators or electric cars. Although they exhibit the highest magnetic moments of all naturally occurring elements (Ho), it is their anisotropy that makes them indispensable for such applications [1, 2]. Also for future applications in e.g. spintronics, which will be discussed in detail in section 2.4, the anisotropy of the 4f-shell is a central point. Therefore we will focus on the anisotropy below.

Before we go into detail about the 4f magnetism and its anisotropy, a brief definition of the quantum number used to describe the magnetic moments of electrons in an atom is given. Every electron in an atom exhibits an intrinsic spin angular momentum \mathbf{s} and an orbital angular momentum \mathbf{l} . They are coupled by the spin-orbit interaction $\zeta \mathbf{l} \cdot \mathbf{s}$ which gets stronger with the increasing atomic number Z [50]. The orbital angular momentum also interacts with the orbital momenta of the other electrons. Based on the relative strengths of these interactions, different coupling schemes occur. If the electron-electron interaction dominates the spin-orbit coupling, for example in 3d-metals, the individual spin \mathbf{s} and orbital \mathbf{l} angular momenta are coupled into atomic spin \mathbf{S} and orbital \mathbf{L} moments, which results in a total angular momentum \mathbf{J}

$$\mathbf{J} = \mathbf{L} + \mathbf{S} = \sum_i \mathbf{l}_i + \sum_i \mathbf{s}_i \quad [51].$$

This Russel-Saunders or LS coupling does not hold for heavy atoms, in which the strong spin-orbit coupling leads to a total angular momentum \mathbf{j} of the individual electrons. In the

so-called jj-coupling, the total angular momentum \mathbf{J} is defined as

$$\mathbf{J} = \sum_i \mathbf{j}_i = \sum_i (\mathbf{l}_i + \mathbf{s}_i).$$

In general, the magnetic moments can be derived from the atomic angular momentum by

$$\boldsymbol{\mu}_l = -g_l \mu_B \mathbf{L}, \quad \boldsymbol{\mu}_s = -g_s \mu_B \mathbf{S}, \quad \boldsymbol{\mu}_j = -g_j \mu_B \mathbf{J}.$$

The g-factors are given as $g_l = 1$, $g_s = 2.00232$ [52] and $g_j = 1 + \frac{J(J+1)+S(S+1)-L(L+1)}{2J(J+1)}$, also known as the Landé factor [53].

It is important to note here, that strong spin-orbit coupling leading to the jj-coupling allows the mixing of states, so that L and S are not good quantum numbers anymore, i.e. L^2 and S^2 are non-commuting observables, while J stays a good quantum number. This changes the complete set of commuting observables from L^2, S^2, J^2, J_z to J^2, J_z . The quantum-mechanical nature of J also forbids a full alignment with the quantisation axis z , as it would violate the uncertainty principle.

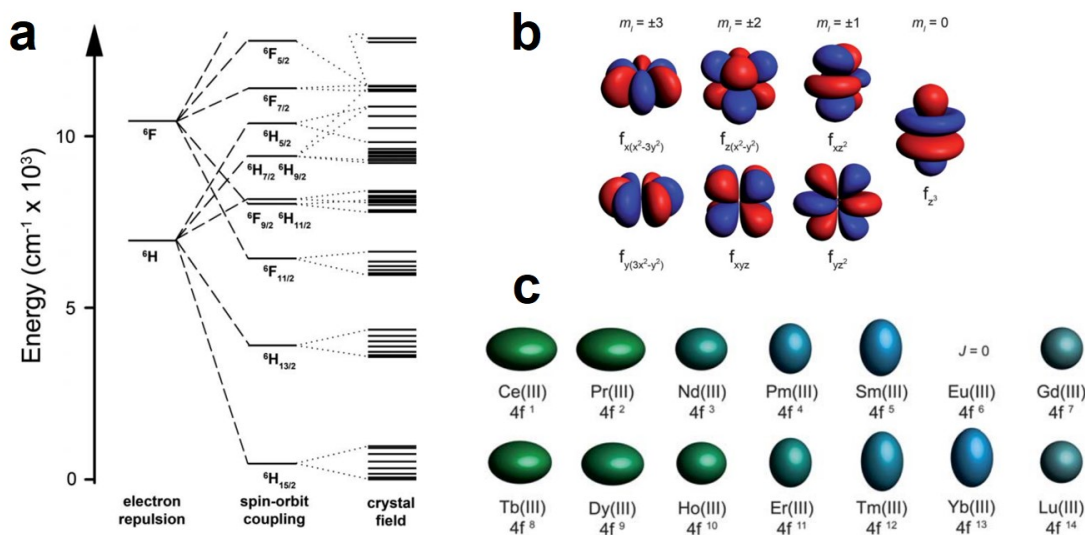


Figure 2-3.: **a** Low energy electronic structure of Dy within the complex $\text{Dy}[(\text{Me}_2\text{Si})_2\text{N}]_3$. **b** Representations of the $4f$ -orbitals for different magnitudes of m_l **c** Quadropole approximations of the $4f$ -shells for all lanthanides in the 3+ oxidation state. **a** adapted from [54], **b**, **c** adapted from [55].

The magnetic anisotropy is strongly correlated with the orbital angular momentum. While the orbital angular momentum is often quenched by the crystal field symmetry in $3d$ -metals, the much stronger spin-orbit coupling (SOC) and more localized nature of the $4f$ -shell allows a high angular momentum in these systems. Taking Dy^{3+} as an example, the 3+ oxidation state is the most stable for all $4f$ -elements, but some also exhibit 2+ and 4+ states, Hund's

rule results in $S = 5/2$, $L = 5$, and $J = 15/2$ for the $4f^9$ electron configuration. Citing textbook knowledge, the SOC is usually dominant over the crystal field in 4f-metals [54]. This can be observed in Fig. **2-3 a**, which presents the low energy electronic structure of Dy within a certain exemplary complex. In this example, the crystal field splitting has no energetic overlap with the SOC states. More recent findings in the last twenty years show, that one can manipulate the crystal field by design, e.g. in single-molecular magnets, that the crystal field indeed has a strong influence on the magnetic ground state [56], which we will present in this work. This includes the discussion about how localised and shielded by the outer electron-shells the 4f-electrons really are and how hybridisation [57, 58] and interaction with the crystal field [59, 60] influence their magnetic properties.

Depending on the ground state, a specific number of orbitals are occupied. Fig. **2-3 b** displays the 4f-orbitals. The 4f-orbitals with the highest magnitude m_l exhibit the most oblate shape, whereas the one with the lowest magnitude m_l show the most prolate shape. Depending on the occupations, this has a direct impact on the shape of the 4f-shell. Fig. **2-3 c** displays the quadrupole approximation of the 4f-shell for all lanthanides, which corresponds to the sum of all occupied orbitals.

The shape of the 4f-shell and therefore its anisotropy is of high importance for many applications. For instance, in the case of SmCo_5 , one of the strongest ferromagnets with a high coercive field, the magnetic anisotropy is created by the delocalized band structure of cobalt interacting with the localized electrons of the Sm ions [55]. The local structure and therefore the crystal field acting on the Sm is highly favouring the strongly prolate $\pm 5/2$ state, creating a highly anisotropic 4f-electron moment, coupling to the delocalised cobalt moment.

As emphasized by the SmCo_5 example, the early lanthanides are favoured in classical ferromagnets, due to their ferromagnetic coupling to delocalized transition metal electrons. In systems, where this coupling mechanism is not relevant, e.g. in single-molecular magnets, one can make use of the higher magnetic moments of the later lanthanides. A comprehensive overview on the effect of the anisotropy of the 4f-shell in such a molecule containing a single 4f-atom is displayed in Fig. **2-4**. A systematic study for all 4f-elements within a $\text{Na}[\text{LnDOTA}(\text{H}_2\text{O})]$ complex, with H_4DOTA = tetraazacyclododecane-N,N',N'',N'''-tetraacetic acid, is presented. The schematic pictures show the magnetic easy axis of the central atom, while the coloured 3D plots give a more detailed view of the susceptibility distributions. The similarity of the progression within the early lanthanides ($4f^n$ $n < 7$) with the later ones shows nicely, how the magnetic properties depend on the orbital angular momentum, which is similar for $4f^n$ and $4f^{n+7}$, e.g. for Ce and Tb. To the contrary Gd exhibits a nearly isotropic behaviour, originating from the lack of orbital angular momentum of the $4f^7$ state.

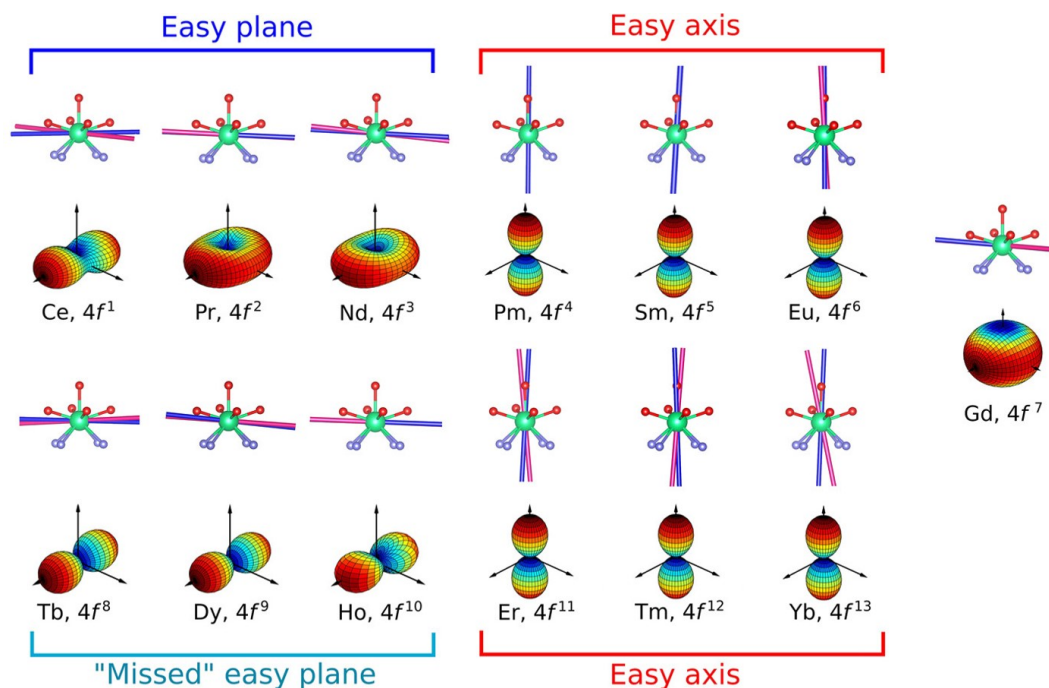


Figure 2-4.: Schematic side view of the local structure and the experimental (pink) and theoretical (blue) easiest axis of the different lanthanides within the $\text{Na}[\text{LnDOTA}(\text{H}_2\text{O})]$ complex. The coloured 3D shapes represent the *ab initio* calculated susceptibility tensor. Adapted from [61].

Within the series, a drastic change can be observed from Nd to Pm and Ho to Er. While the lower $4f$ occupations favour an easy plane in the molecular plane, the higher $4f$ -occupations exhibit an easy axis normal to the molecular plane. This is in line with the strong anisotropy induced by Sm in the SmCo_5 system. Comparing the susceptibility tensor of Ce, Pr, and Nd, with the one of Tb, Dy, and Ho, one can see, that the early lanthanides develop a real easy plane, whereas especially Tb and Dy show an easy axis like behaviour within the plane. This difference is of high relevance, especially when one thinks of possible applications in spintronics, where a defined easy axis is highly desirable.

To summarize, $4f$ -magnetism provides not only the highest magnetic moments of all stable elements but is also already present in our everyday lives, mainly in the form of strong permanent magnets. The unique feature, that makes $4f$ -elements also interesting for future nano-sized devices, is their large orbital angular moment, leading to a highly anisotropic behaviour. While early research suggested, that the $4f$ -electrons are so localised and shielded by their outer electrons, that there is no strong interaction with the local surrounding, the recent development in the last decades showed, that the magnetic properties can be strongly influenced by tailoring the local environment. The understanding of how the local crystal field and hybridisation influence the magnetic properties and how one can use this in order

to develop future devices based on 4f-metals is the topic of ongoing research and will be also discussed in this work.

2.3. 4f Surface Alloys

Sitting just at the crossing point in between 4f-bulk structures as discussed in section 2.2 and organometallic compounds described in section 2.4, the 4f-surface alloys manipulate the structural, electronic, and magnetic properties of a substrate just at the surface.

4f-surface alloys have been described for several transition metals single-crystal surfaces, including Ag(111) [62, 63, 64], Au(111) [65, 66, 67, 68], Cu(111) [69, 70], Pt(111) [71], and Mo(112) [72]. Including almost all of the 4f-metals within these surface alloys, they exhibit a number of interesting properties, including their electronic, catalytic, and their 2D magnetic properties, which will be introduced in detail below. It is important to mention, that nearly all of the surface alloys published so far have the ratio of one rare earth atom to two transition metal atoms (RETM_2), leading to a $(\sqrt{3} \times \sqrt{3})\text{R}30^\circ$ superstructure on a hexagonal surface. This is in strong contrast to the (2×2) superstructure we present in this work, which would translate to RETM_3 . A (2×2) superstructure of Tm on Ir(111) has been firstly described in the master thesis of S. Kraus [73] and is included in Ref. [74], which will be described in chapter 4.

An exemplary structure of such surface alloys is presented in Fig. 2-5. It is important to note, that the structures presented in the following are monolayer surface alloys. Different to the growth of Gr/Ir(111) presented in section 2.1, the growth is not self-limiting and an additional amount of 4f-metals leads to the growth of multilayer surface alloys [71].

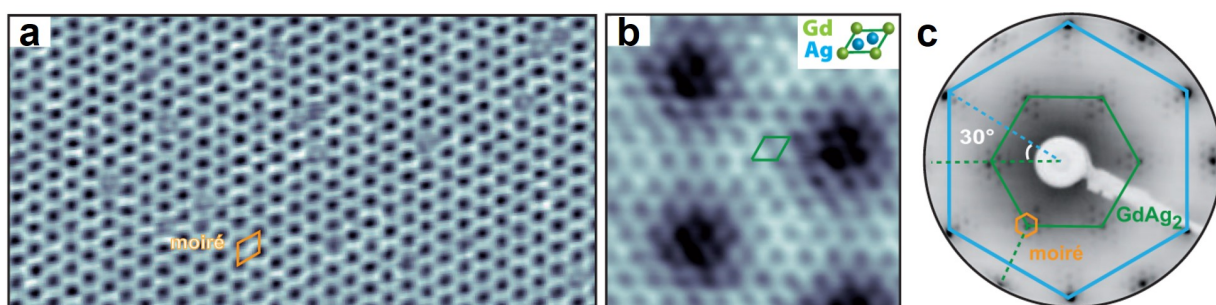


Figure 2-5.: **a** STM topograph of a GdAg_2 monolayer on Ag(111) ($95 \text{ nm} \times 47 \text{ nm}$). The moiré is indicated by the orange rectangle. **b** Atomic resolution STM topograph of the sample in **a** ($6 \text{ nm} \times 6 \text{ nm}$). The GdAg_2 unit cell is indicated in green and schematically sketched in the upper right corner. **c** Contrast-inverted LEED pattern of the sample in **a** at 50 eV primary electron energy. The coloured hexagons correspond to the first order reflexes of the structures indicated in **a** and **b** and blue corresponds to the Ag(111) surface. Adapted from [62].

Fig. **2-5 a** displays a STM topograph of a GdAg_2 surface alloy on $\text{Ag}(111)$. The RETM_2 surface alloys form a moiré structure, as indicated in the STM topograph. The close up in Fig. **2-5 b** displays the atomic structure of the surface alloy. It is shown, that growth of high quality and low defect density can be realized. The phase purity of this system is also supported by the LEED pattern presented in Fig. **2-5 c**. Only the principle $\text{Ag}(111)$ reflexes, the surface alloy and the moiré reflexes are visible. A growth temperature of 600 K is necessary on $\text{Ag}(111)$ to achieve this high quality. The temperature needed for the alloying depends on the single-crystal substrate. While for $\text{Au}(111)$ a significant amount of Gd diffuses into the substrate at 500 K [65], a growth temperature of 926 K has been reported for $\text{Pt}(111)$ [71].

The electronic properties of a similar system, namely DyAg_2 surface alloy on $\text{Ag}(111)$, are presented in Fig. **2-6**. Spin resolved ARPES measurements of the band structure around the $\Gamma^{(1)}$ point are presented in Fig. **2-6 a**. While the spectrum shows dispersion and strongly spin-split flat bands, a more detailed analysis is possible by comparing these results with theoretical band structure calculations presented in Fig. **2-6 b**.

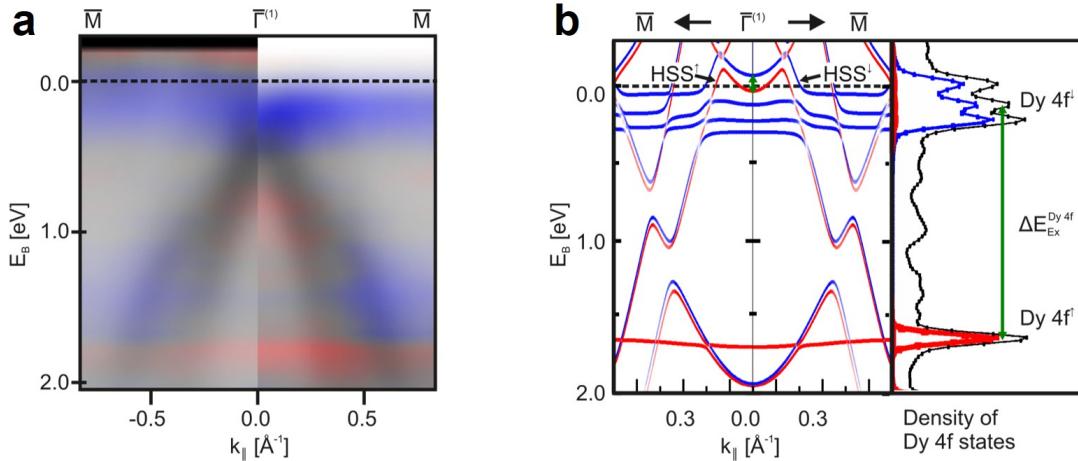


Figure **2-6**.: **a** Spin resolved band structure cut through the hybrid surface state along the $\bar{\Gamma}^{(1)}\bar{M}$ direction of a DyAg_2 monolayer surface alloy. Blue indicates the spin polarization of the minority electrons, red corresponds to the majority electrons. The left half is normalized in order to highlight the feature above E_F . **b** Respective spin-resolved band structure calculation and the spin-resolved density of the Dy 4f states. Adapted from [64].

The most obvious feature is the spin-split 4f-band of Dy. While the relatively narrow majority band sits at about $E_B = 1.8$ eV, the minority band has its center at $E_B = 0.2$ eV. The normalisation of the left side of Fig. **2-6 a** clearly shows, how the minority states extend in the region above the Fermi level. These two nearly non-dispersing bands correspond to the localised 4f-derived states. The existence of the two exchange split Dy 4f states with an

exchange energy of 1.6 eV is clear spectroscopic evidence of the ferromagnetic order of the Dy 4f magnetic moments [64]. Another interesting feature is the dispersing hybrid surface states, indicated as HSS in Fig. 2-6 b and also visible in the experimental spectrum. This Dy-Ag hybrid state corresponds to the sp-band of the Ag(111) surface, which is back folded at the Dy-Ag superstructure.

As mentioned above, the electronic structure indicates a ferromagnetic order of such surface alloys. For a deeper understanding of the magnetic properties of such surface alloys, Fig. 2-7 presents X-ray absorption near-edge spectroscopy (XANES), X-ray magnetic circular dichroism (XMCD), and magneto-optical Kerr effect (MOKE) measurements of the GdAg₂ and GdAu₂ surface alloys.

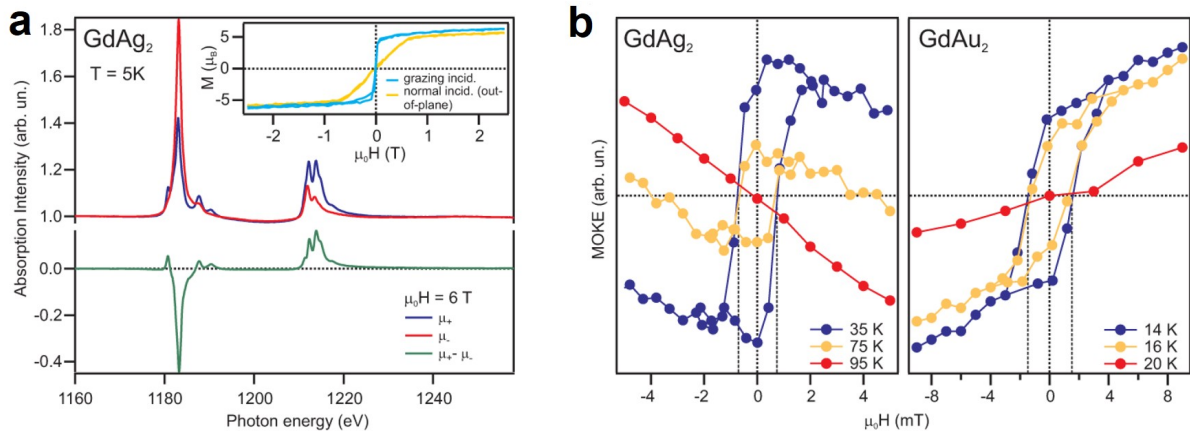


Figure 2-7.: **a** XANES and XMCD spectra of the Gd $M_{4,5}$ edge of a GdAg₂ monolayer surface alloy at a temperature of 5 K, a magnetic field of 6 T, and normal incidence. The inset presents the respective magnetisation curves for normal and grazing incidence. **b** MOKE loops for GdAg₂ and GdAu₂ monolayer surface alloys for different temperatures. Adapted from [62].

The low temperature and high field XANES and XMCD measurement in Fig. 2-7 a present a $4f^7$ state of Gd and a magnetisation close to saturation. The magnetisation curves show an anisotropic behaviour with an easy axis within the surface plane. Within the error, no opening of a hysteresis loop can be detected. The MOKE measurements in Fig. 2-7 b prove, that this is caused by the low resolution and large error caused by the superconducting magnets. Allowing a detailed view within the range of a few mT, the MOKE loops reveal an opening of a hysteresis loop. In line with the indication based on the electronic structure, a ferromagnetic order emerges below the Curie temperature of $T_C^{\text{GdAg}_2} = 75 \pm 5$ K for GdAg₂ and $T_C^{\text{GdAu}_2} = 19 \pm 5$ K for GdAu₂. Hereby, the coercive field lies in the range of $H_C \approx 1$ mT. This relatively small coercive field could be explained by the negligible in-plane anisotropy of this system.

Possible applications range from nano templates [65] to the tuning of the properties of absorbed systems by the interaction with a ferromagnetic substrate [75], but will not be discussed in detail in this introduction. In summary, $4f$ surface alloys provide well ordered exemplary model systems, in which the interaction of the $4f$ -elements with the local surrounding can be studied as well as the emergence of 2D ferromagnetic order. This ferromagnetic order and their structure make them interesting templates for organometallic spintronic applications, which will be discussed in the next section.

2.4. $4f$ -Based Organometallic Spintronics

In this section, we want to introduce different types of organometallic spintronics based on $4f$ -metals and their magnetic properties. These systems, which may be building blocks of future nanosized and energy-efficient spintronic applications, can be categorized by dimensionality. They range from "zero-dimensional" single-molecule magnets and single-atom magnets, over one-dimensional nanowires, to two-dimensional organometallic networks. For each of these systems, a brief introduction will be given in the following.

0D single-molecule magnets and single-atom magnets

The discovery of slow magnetic relaxation in coordinated lanthanide compounds containing a single magnetic ion [76], the so-called single-molecule magnets, gathered a lot of attention in the scientific community. The magnetic hysteretic behaviour of these systems makes them promising candidates for future spintronic applications, like spin qubits [77] and nano-sized spintronic devices [78, 79, 80]. Some of the first approaches to obtaining nano-sized magnetic structures have been transition-metal ion clusters [81]. In contrast to other magnetic materials, where the coupling to other spins leads to the hysteretic behaviour, the coordination of a single magnetic ion allows long-living magnetic states in $4f$ single-molecule magnets (therefore 0D). Thereby the precise manipulation of the $4f$ magnetic properties by coordination is the key to further boosting their development.

Their magnetic bistability is based on their anisotropy barrier, separating a degenerate ground state [55]. The blocking temperature defines for single-molecule magnets, below which temperature a hysteretic behaviour can be observed, comparable to the Curie temperature in ferromagnets. As discussed in section 2.2, $4f$ -metals can provide a strong electronic and magnetic anisotropy due to their high orbital angular momentum. From special interest are hereby the heavier lanthanides, as they combine large orbital moments with an overall large magnetic moment [82, 60].

An example for such a single-molecule magnet is presented in Fig. 2-8. The structure of the Dy-based metallocene penta-iso-propylcyclopentadienyl-Dy-pentamethylcyclopentadienyl $[(Cp^{iPr5})Dy(Cp^*)]^+$ is presented in Fig. 2-8 a. The magnetic ion Dy is coordinated in between two methyl rings, which have side groups attached, all being non-magnetic. It

is also indicated, that the molecule is charged and therefore needs a counter ion, namely $B(C_6F_5)_4$. This issue will be addressed below.

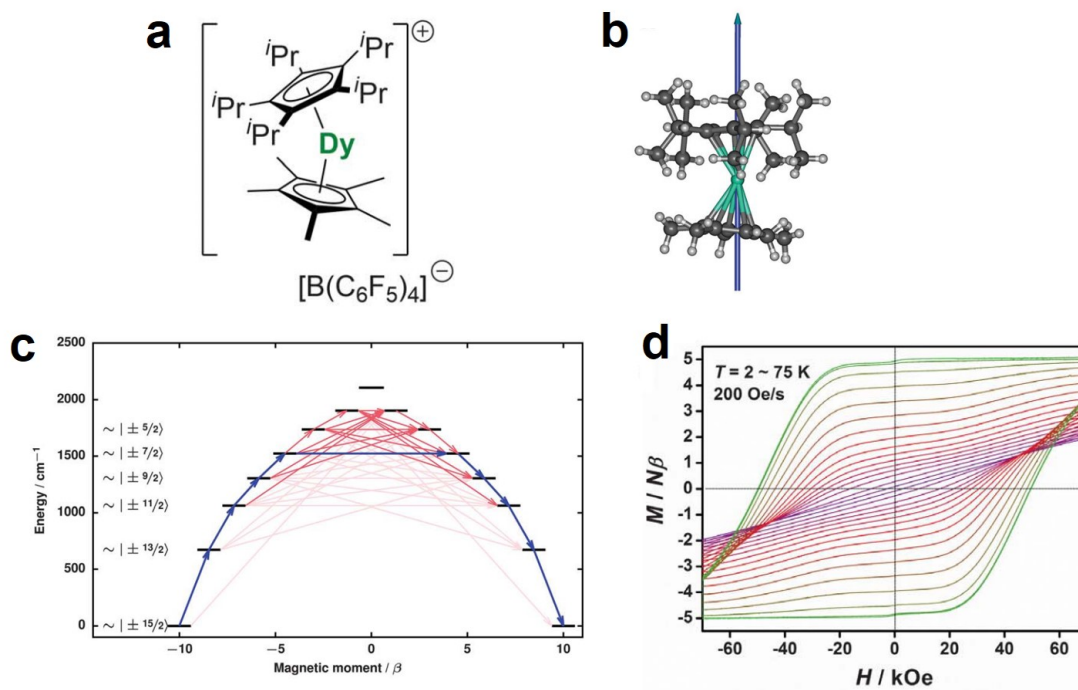


Figure 2-8.: **a** Chemical structural formula of the Dy metallocene cation pentameta-iso-propylcyclopentadienyl-Dy-pentamethylcyclopentadienyl $[(Cp^{iPr5})Dy(Cp^*)]^+$ **b** Structural sketch of $[(Cp^{iPr5})Dy(Cp^*)]^+$ with the principle magnetic axis of the ground Kramer's doublet indicated. **c** Multiplet level scheme and the relaxation mechanism of the Dy ion. Blue arrows indicate the most probable relaxation route, red arrows show less probable transitions, with lighter colours, indicate less probable transitions. **d** Field dependent magnetisation of $[(Cp^{iPr5})Dy(Cp^*)]^+$. Hysteresis loops from 2 K (green) to 75 K (purple) are presented. Adapted from [59].

A ball model of the structure with the principle magnetic axis of the ground state is presented in Fig. 2-8 b. The principle magnetic axis belongs to the $\sim |\pm 15/2\rangle$ degenerate ground state of the Dy presented in Fig. 2-8 c. With the precise manipulation of the local surrounding of the Dy in this molecule, i.e. the coordination and the crystal field, the energy barrier for the transition between the states is maximised. The most probable relaxation route is indicated in this scheme. This energy barrier leads to a relatively high blocking temperature in this system, evaluated in Fig. 2-8 d. While an open hysteresis is present for 2 K up to 75 K, further analysis revealed a blocking temperature of up to $T_B = 80$ K [59]. With this, the important barrier for applications of 77 K is surpassed, which corresponds to the boiling temperature of liquid nitrogen at ambient pressure. To the best of our knowledge, this is

the highest blocking temperature reported for $4f$ -based single-molecule magnets so far. Although this system seems to be a good fit for future applications due to its high blocking temperature, there is one big downside. The need for a counter ion for the stability of this complex not only complicates its use, but also limits the ordered distribution on a substrate, which is essential for future applications.

The interaction with a substrate leads to additional challenges, like additional decaying paths of the magnetic state due to the interaction with the substrate, e.g. quantum tunnelling of magnetisation [83]. Fig. 2-9 presents two different ordered single molecular magnet systems on surfaces.

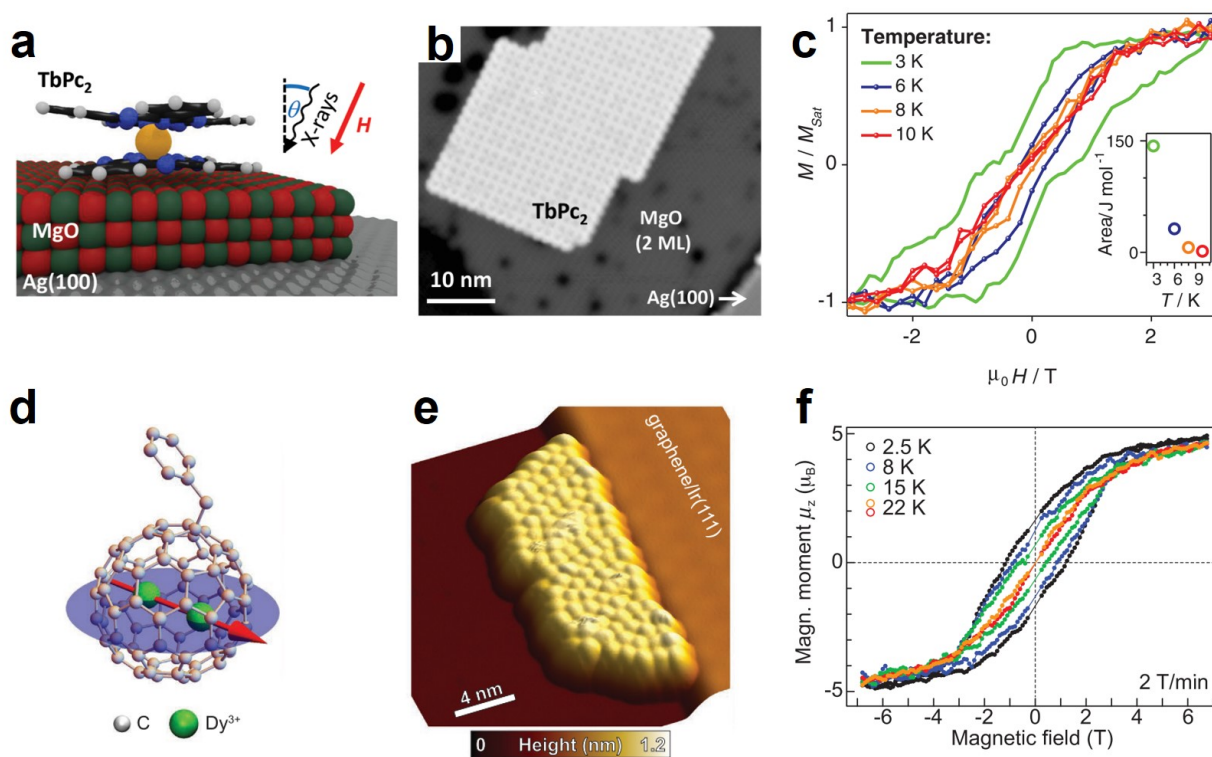


Figure 2-9.: **a** Sketch of TbPc_2 molecule on ultrathin MgO film on $\text{Ag}(100)$. The x-ray incidence angle and the external magnetic field are indicated. **b** STM topograph of TbPc_2 molecules on $\text{MgO}/\text{Ag}(100)$ **c** XMCD magnetisation loops of the $\text{Tb } M_5$ edge of TbPc_2 molecules on $\text{MgO}/\text{Ag}(100)$ for different temperatures. **d** Sketch of the molecular structure of $\text{Dy}_2@C_{80}(\text{CH}_2\text{Ph})$. The magnetic easy axis is indicated. **e** STM topograph of $\text{Dy}_2@C_{80}(\text{CH}_2\text{Ph})$ molecular island on $\text{Gr}/\text{Ir}(111)$. **f** XMCD magnetisation loops of the $\text{Dy } M_5$ edge of submonolayer $\text{Dy}_2@C_{80}(\text{CH}_2\text{Ph})$ islands on $\text{Gr}/\text{Ir}(111)$ for different temperatures. **a-c** adapted from [84], **d-f** from [85].

Fig. 2-9 **a** shows a schematic side view of a TbPc_2 single-molecule magnet on isolating MgO on $\text{Ag}(100)$. The Tb double-decker, sandwiched between two identical phthalocyanine (Pc)

molecules, is physisorbed on the MgO surface. The STM topograph in Fig. **2-9 b** displays well ordered TbPc₂ islands on the surface. The blocking temperature of this adsorbed system can be extracted out of Fig. **2-9 c** and lies at around 8 K, which has been the highest blocking temperature ever reported for surface-adsorbed single-molecule magnets in the year 2016 [84]. The drastically reduced blocking temperature corresponds to the interaction of the magnetic moment of the molecule with the substrate [86, 87]. The approach to decrease the electronic and phononic interaction with the substrate is to isolate the molecules from the substrate, e.g. by adding an insulating MgO layer. Another approach would be the coupling of the molecules to a ferromagnetic substrate [14].

Fig. **2-9 d** introduces a new type of single-molecule magnets. Radical bridged complexes [88] and 4f metallofullerenes [89, 85] include two magnetic ions, as depicted in Fig. **2-9 d**. Without going into detail about this type of single-molecule magnet, we want to introduce another substrate, that can be used to order the molecules and to significantly increase the blocking temperature: Gr/Ir(111). The STM topograph shows an island of Dy-based metallofullerenes (Dy₂@C₈₀(CH₂Ph)) on Gr/Ir(111), which has been introduced in section 2.1. The molecules order with respect to the moiré of Gr/Ir(111). The magnetisation curves in Fig. **2-9 f** reveal a blocking temperature of $T_B = 17$ K for this system.

The systems presented above would qualify as prototypes for high-density data storage devices. Thinking of even higher densities, one has to further reduce the size of the magnetic system, ultimately leading to single atoms. While single-molecule magnets are mostly physisorbed and therefore relatively isolated from the substrate, single atoms are in much closer contact with the substrate. In order to detect hysteretic behaviour on single atoms, the substrate and the coordination of the magnetic atom have to be chosen even more carefully.

Magnetic remanence above 1 K in single atoms has been recently detected in Ho atoms on MgO/Ag(100) [5]. An STM topograph of this system is provided in Fig. **2-10 a**. The single separated Ho atoms on the surface are shown. The corresponding schematic side view is presented in Fig. **2-10 b**. The Ho atom sits preferably on top of an O atom. The magnetisation loops in Fig. **2-10 c** show a hysteresis up to 30 K. The coercivity significantly increases with increasing MgO thickness and is constant above 3.6 ML [5]. The MgO layer is also responsible for the long-living states of the Ho atom. The C_{4v} symmetry of the O adsorption leads to a ground state doublet of the quantum states $J_z = \pm 7, \pm 3, \pm 1$, and ± 5 , which protects the states from first-order spin excitation ($\Delta m = 0, \pm 1$) at any magnetic field [90]. While this prevents magnetisation reversal by electron scattering, the first-order scattering with phonons ($\Delta m = \pm 1, \pm 2$) is suppressed by the low density of vibrational modes in the MgO layer [5]. Combining this with a considerable large energy gap of 4.5 meV to the first excited states leads to a characteristic lifetime of $\tau = 1586 \pm 131$ s at 10 K. The comparable lifetime at 2.5 K indicates, that the magnetic relaxation is driven by non-thermal processes in this regime.

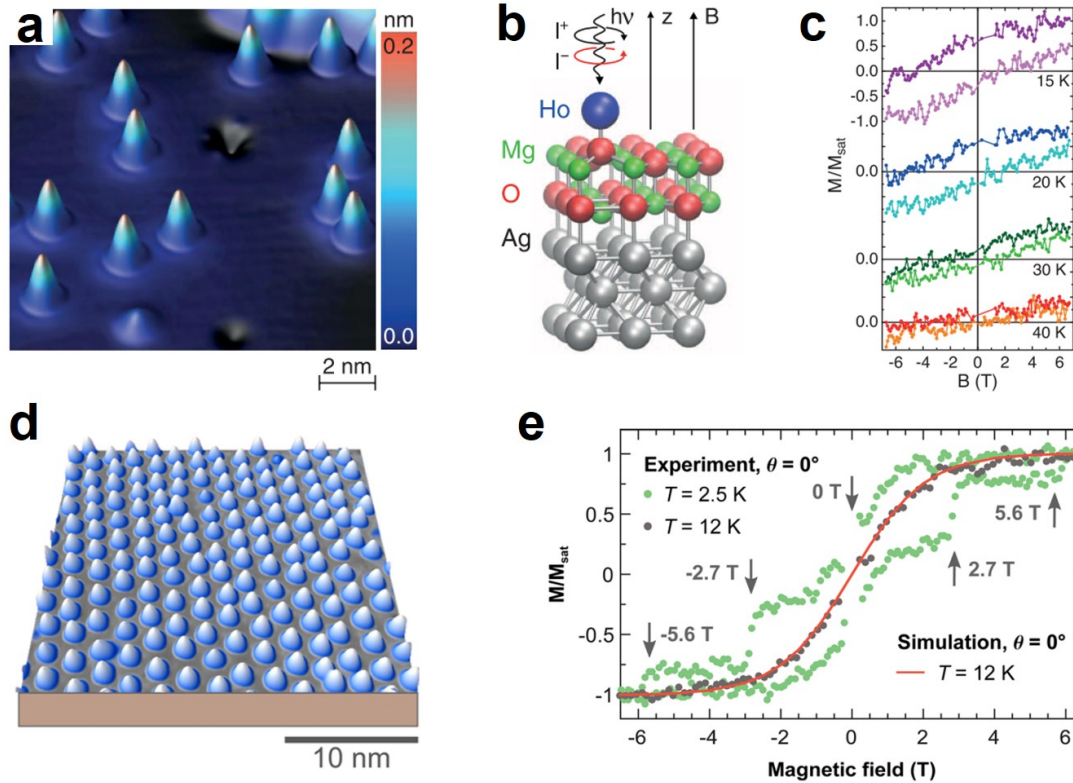


Figure 2-10.: **a** STM topograph of single Ho atoms on 2 ML MgO/Ag(100). A schematic sketch of the sample is shown in **b**. The X-ray incidence and the magnetic field direction are indicated. **c** XMCD magnetisation loops of the Ho M_5 edge of Ho/MgO/Ag(100) for different temperatures. **d** STM topograph of Dy atoms ordered with respect to the moiré of Gr/Ir(111) **e** XMCD magnetisation loops of the Dy M_5 edge of Dy/Gr/Ir(111) for different temperatures. The steps in the magnetisation loop corresponding to the magnetic level crossings are indicated with arrows. **a-c** adapted from [5], **d-e** from [12].

Similar to the two systems presented in Fig. 2-9, the second system presented in Fig. 2-10 uses Gr/Ir(111) as a substrate. A significant advantage compared to the MgO/Ag(100) substrate is visualized in the STM topograph presented in Fig. 2-10 d. The moiré lattice introduced in section 2.1 leads to separation and a well-ordered superlattice of single Dy atoms on Gr/Ir(111). Similar to the Ho/MgO system, a magnetic hysteresis can be obtained at low temperatures, as depicted in Fig. 2-10 e. The mechanism is similar, besides making use of the C_{6v} symmetry of the crystal field. Although the Dy/Gr/Ir(111) lifetimes are slightly smaller than for Ho/MgO/Ag(100), Gr/Ir(111) proves to be an excellent decoupling layer and substrate for possible spintronic applications.

As the systems described above mainly act as possible memory devices, we want to introduce another possible application very briefly, namely supramolecular spin valves [11].

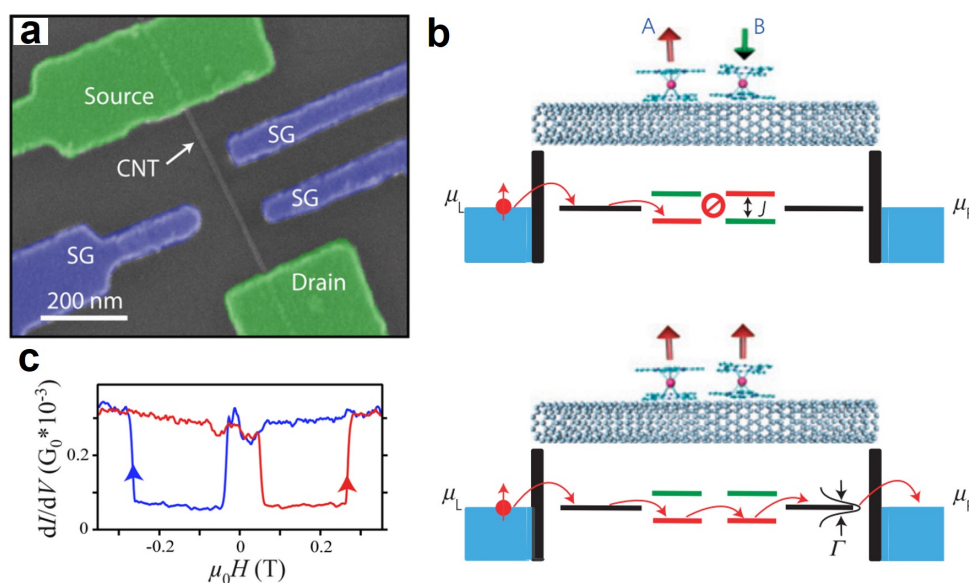


Figure 2-11.: **a** SEM micrograph of molecular spin-valve device. Source, drain, side-gates and the carbon nanotube are indicated. **b** Schematic side view of the molecular spin-valve device. The working principle of the spin valve is indicated by the magnetic moments A and B of the TbPc_2 molecules. While the conductance is lowest for opposing orientations of the spins, the conductance is highest for aligned spins. **c** Spin-valve features of the device. The red curve gives the differential conductance as a function of the magnetic field going from negative to a positive value, the blue curve from positive to negative values. **a**, **c** adapted from [91], **b** adapted from [11].

Fig. 2-11 **a** displays a scanning electron microscopy (SEM) image of a spin valve device. A schematic side view of this structure is presented in Fig. 2-11 **b**. It mainly consists of a carbon nanotube (CNT) with adsorbed TbPc_2 molecules in between a source and a drain. Side gates allow the manipulation of the spin filter properties. For such a long device, the TbPc_2 are diluted by YPc_2 , which are nonmagnetic, so that the spin filter consists of only two TbPc_2 molecules. The principle behind this spin-filter is indicated by this exemplary electron with spin up. While there is a barrier for anti-parallel alignment for spin-up and spin-down electrons, there is a high conductance for electrons with their spin parallel to both molecules. Such behaviour is presented in the conductance measurement in Fig. 2-11 **c**. Possible applications of such spintronic transistors are still limited today, as temperatures far below 1 K are necessary, for a stable operation.

1D organometallic nanowires

While the spin-filter presented in Fig. 2-11 was a mixture of 0D and 1D structures, we want to focus purely on 1D structures in the following. The early investigations of such

organometallic nanowires or sandwich molecular nanowires, consisting of alternating metal atoms and organic ligands, have been conducted on V-benzene wires [92, 93, 94]. They have been predicted to be ferromagnetic half metals with spin-filter properties [95] and have been experimentally synthesised in the gas phase by laser vapourisation and a ferromagnetic order was detected [96]. A number of combinations of various $3d$ -metals [97, 98] and organic ligands [99, 100] have been investigated, but will not be discussed in detail in this introduction. In this work, we want to focus on $4f$ -based organometallic nanowires. Lanthanide-based organometallic nanowires consist of alternating $4f$ -metal ions and cyclic organic ligands. While a number of different lanthanides can be incorporated, the reported ligands are mostly limited to cyclooctatetraene (Cot) [101]. Cot is a cyclic-eightfold carbon ring, which gets aromatic by accepting two electrons in its π system [102, 103]. Lanthanides provide mainly their two $6s$ electrons, but hybridization of the Eu $4f$ states with the Cot π orbitals have been reported based on *ab initio* calculations [104]. A 1D ferromagnetic order within the wire and spin-filter properties have been theoretically predicted [10]. It has also been reported, that the semiconducting properties of EuCot nanowires change to half-metallic when modifying the Cot ligand by B-doping [105].

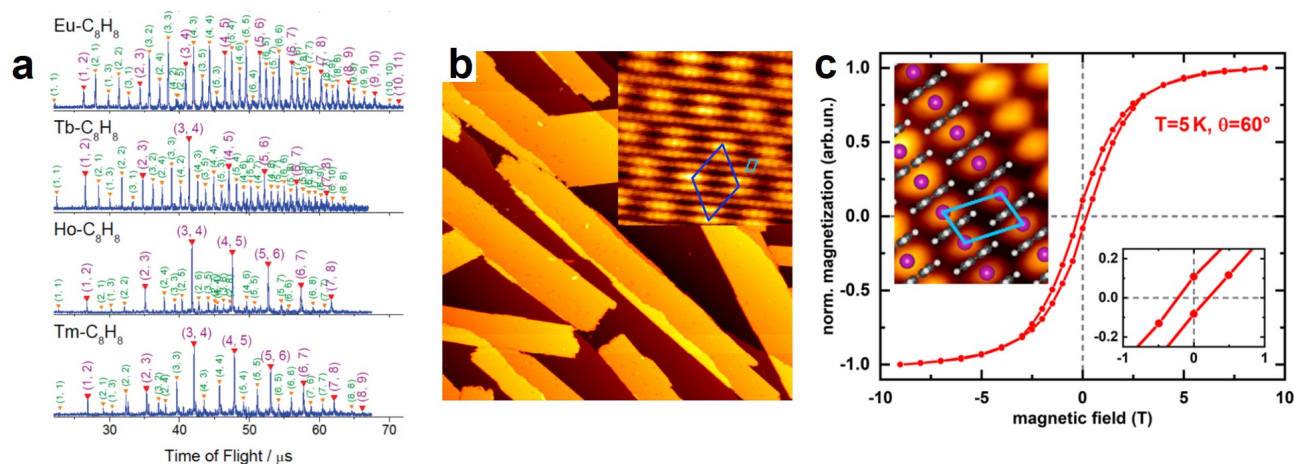


Figure 2-12.: **a** Time of flight spectra of photoionized Ln-Cot clusters at 100 K (Ln = Eu, Tb, Ho, Tm). Each peak of $\text{Ln}_n(\text{C}_8\text{H}_8)_m$ is labeled with the notation (n, m) . **b** Overview STM topograph of EuCot nanowire islands on Gr/Ir(111) ($260\text{ nm} \times 260\text{ nm}$). The inset displays a close-up of a nanowire island ($10\text{ nm} \times 10\text{ nm}$). The moiré cell and the nano-wire unit cell are indicated. **c** XMCD magnetisation loop of the Eu M_5 edge of EuCot nanowires on Gr/Ir(111) for grazing incidence at 5 K. The zoom-in on the right shows the behaviour around zero-field. The inset on the left shows a molecular resolution STM topograph of the wires ($5\text{ nm} \times 3\text{ nm}$). A ball model and the unit-cell of the nanowires are overlaid. **a** adapted from [101], **b**, **c** from [18].

Experimentally, LnCot nanowires have been firstly synthesised in gas-phase experiments [106, 101]. Fig. **2-12 a** presents time of flight spectra of Ln-Cot clusters, with the lanthanides Eu, Tb, Ho, and Tm. All systems exhibit wire growth of at least a few segments. The longest wires observed are EuCot nanowires. This can be explained by the energy difference between the 2+ and 3+ state, which is the smallest for Eu due to its half-filled 4*f*-shell [107]. This leads to chemically reactive wire ends for Eu, that allow further growth. Stern-Gerlach experiments observed a magnetic moment of $7 \mu_B$ per Eu atom increasing with the wire length [106], which is in line with the theoretical predictions of ferromagnetic coupling.

Similar to the situation described for 0D systems, a substrate is essential for possible applications. From the systems described above, EuCot nanowires are the only LnCot nanowires, which have been reportedly grown on a substrate [108]. Islands of EuCot nanowires on Gr/Ir(111) are presented in the STM topograph in Fig. **2-12 b**. The wires show exceptional quality, a bandgap of ~ 2.3 eV, and lengths up to the μm regime. The inset in Fig. **2-12 c** displays the molecular resolution, including a ball model of the wires. The interlocking of neighbouring wires results in the growth of nanowire islands. The measured hysteresis proved the theoretical predictions and confirmed a ferromagnetic order below 7 K [18].

2D organometallic networks

2D organometallic networks allow the exact distribution and coordination of metallic atoms within a surface plane [109]. By variation of the connecting molecules, the separation can be precisely tuned. By the modulation of the active binding site, the crystal field, as well as the electronic and magnetic properties of the metal ions, can be manipulated.

Fig. **2-13** presents two exemplary systems of 4*f*-based organometallic networks. The STM topograph in Fig. **2-13 a** shows a 4-fold coordinated Eu-based organometallic network. The structure and the binding to the metal ion is indicated in the ball model. The coordination of the Eu can be tuned by the ratio of Eu to para-quaterphenyl-dicarbonitrile, from threefold for a ratio of 2:3 up to sixfold for a ratio of 2:6 [110]. A Dy-based network is displayed in Fig. **2-13 b-d**. The STM topograph displays the 4-fold coordinated Dy atoms, connected by TDA molecules as highlighted in Fig. **2-13 b**. The Dy atoms are hereby coordinated by O atoms. The influence of the coordination by different molecules on the magnetic properties has been studied [111]. For the exemplary system presented here, the magnetisation curves in Fig. **2-13 d** indicate an increased anisotropy of the Dy atoms by the coordination. For other 2D systems containing 3*d*-metals, ferromagnetic coupling could be observed [112, 113].

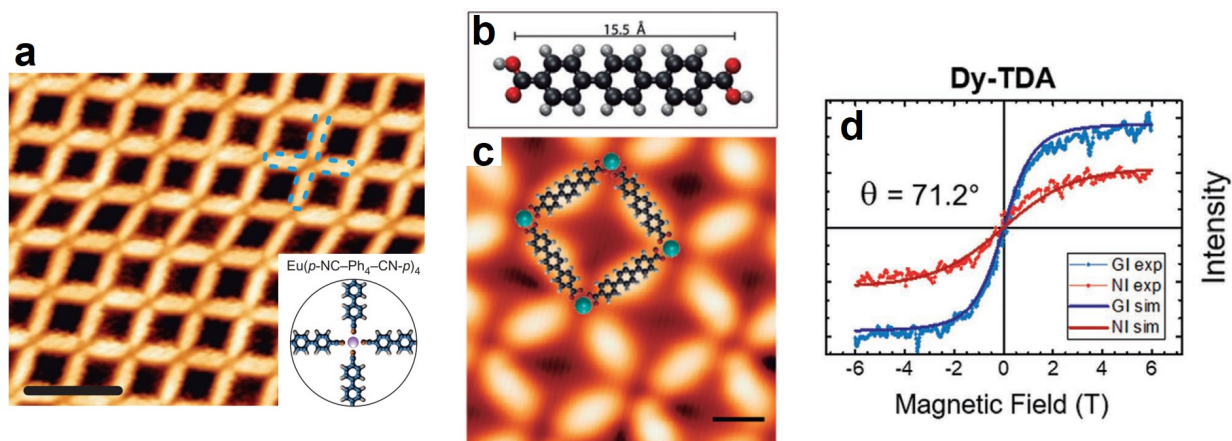


Figure 2-13.: **a** STM topograph of Eu MOCNs distinct coordination networks. The scale bar is 5 nm. An atomistic ball model of the $\text{Eu}(\text{p-NC-Ph}_4\text{-CN-p})_4$ structure including the para-quaterphenyl-dicarbonitrile ($\text{p-NC-Ph}_4\text{-CN-p}$) molecule is presented in the inset. **b** Ball model of p-terphenyl-4,4'-dicarboxylic acid (TDA). **c** STM topograph Dy-TDA network of Cu(111). A ball model is overlaid. Scale bar 1 nm. **d** XMCD magnetisation loop of the Dy M_5 edge of Dy-TDA network of Cu(111) for normal and grazing incidence at 6 K. **a** adapted from [110], **b-d** adapted from [111].

In summary, the coordination of $4f$ -metals by organic molecules provides a playground for future nanosized spintronic applications. The precise manipulation of the $4f$ magnetic properties by the organic ligands in single-molecule magnets leads to relatively stable magnetic configurations, which may be utilized as qubits. The selection of the right substrate is crucial to achieving long-living states, even in single-atom magnets, making use of geometries and favourable material properties. Gr/Ir(111) proved to be such a substrate. Spin-filter properties can be observed in sandwich-molecular nanowires and in combinations of 0D and 1D structures. EuCot nanowires can be grown on Gr/Ir(111) and provides a 1D ferromagnetic and semiconducting structure, which may be utilized for future spin-filter devices. Finally, the 2D organometallic networks underlined, that coordination is the key for the precise manipulation of $4f$ -magnetic properties.

3. Experimental and Computational Techniques and Setups

In this work, a wide range of surface sensitive methods have been used. For structural determination, low-energy electron diffraction (LEED) and scanning tunnelling microscopy (STM) was utilised. For electronic and magnetic measurements x-ray near-edge absorption (XANES), x-ray magnetic circular dichroism (XMCD), x-ray linear dichroism (XLD), and x-ray photoemission spectroscopy (XPS) were performed. The experiments have been accompanied by theoretical multiplet calculations. Our experimental setups used in this work are introduced in section 3.7.

3.1. Low-Energy Electron Diffraction

Low-energy electron diffraction (LEED) was not only the first proof of the wave nature of the electron [114], but is also the main method to analyse the structure of ordered surfaces. Hereby, as indicated by the name, a beam of monochromatic low-energy electrons with typical energies of $E = 20\text{-}500$ eV is directed perpendicular onto the sample surface. From the backscattered electrons the inelastically scattered electrons are filtered out by a hemispherical grid. The elastically scattered electrons get accelerated onto a fluorescent screen by a high voltage of typically $U_{screen} = 5$ kV which converts them into visible light, displaying the diffraction pattern of the surface.

In the case of a multi-channel plate (MCP) LEED, an additional multi-channel plate is placed between the retarding grid and the screen in order to amplify the incoming electrons. This allows reducing the current of the electron beam by several orders of magnitude, which is relevant for sensitive structures like molecular systems, but comes at the prize of a distorted diffraction pattern, as multi-channel plates can only be manufactured as flat discs.

The underlying physics are essentially similar to other forms of crystalline diffraction, besides the high surface sensitivity of LEED, which is caused by the small penetration depth of the electrons in the order of a few Å. As the translation symmetry normal to the surface is always broken at the surface, it relaxes the Laue condition leading to a two-dimensional treatment. The diffraction pattern hereby represents the 2D reciprocal space of the surface. A more detailed introduction to the LEED technique and the underlying physics is given in Ref. [115].

3.2. Scanning Tunnelling Microscopy

Scanning tunnelling microscopy (STM) is a surface science technique allowing the imaging of surfaces with atomic resolution. The fact that Binnig and Rohrer received the Nobel prize less than four years after their publication in 1982 [116] shows the outstanding opportunities of this technique which is indispensable in today's nano- and surface science.

The basic principle of this technique is to scan a conducting sample surface with a conducting tip and thereby make use of the quantum mechanical tunnelling of electrons through the vacuum gap between the sample and the tip. To enable the quantum tunnelling, the tip is held at a distance of about 1 nm above the sample and a bias voltage U_{Bias} in the order of meV up to a few V is applied. The resulting tunnel current I_t has an exponential dependence of the distance d in this regime, leading to a very high vertical sensitivity. To be more exact, the current depends on the local density of states of the tip ρ_T and the sample ρ_S , the Fermi function at a finite temperature $f(E)$, the applied bias voltage U_{Bias} and the tunnelling matrix element M

$$I \sim \int_{-\infty}^{+\infty} |M|^2 [f(E - eU) - f(E)] \rho_S(E_f - eU) \rho_T(E_f). \quad (3-1)$$

That shows, that STM neither measures the positions of the atomic nuclei, nor the topography rather than the local density of states. Nevertheless, they are of course strongly connected. But due to the variation of the asymptotic decay of the different states, this leads for example to the case, that localized $4f$ states are basically inaccessible to STM [117].

The precise manipulation for scanning the sample is provided by piezo elements. They allow sub-Å manipulation in the X-, Y-, and Z-direction. The most common scanning mode, also used in this work, is the constant current mode. The current is hereby set to a fixed value typically in the range of pA to nA and the output of the feedback loop controlling the Z-piezo is recorded as the topography while scanning the sample. A more detailed introduction into the field is given in Ref. [118].

3.3. X-ray Absorption Spectroscopy

The development of tunable, brilliant, and polarized synchrotron-based X-ray sources enabled a wide spectrum of new measurement techniques. X-ray absorption spectroscopy (XAS) makes use of the energy-dependent absorption of these X-rays in matter. From special interest are hereby the regions around the absorption edges, which can be divided into the X-ray absorption near-edge structure (XANES) providing information about the local electronic structure, the local chemical environment, and the magnetic properties and the extended X-ray absorption fine structure (EXAFS), contributing information about the local environment and the neighbouring atoms.

In this introduction, we will focus on the XANES. A detailed introduction to synchrotron radiation, XAS, and other synchrotron-based methods is given in Ref. [119]. Differing from photoelectron spectroscopy, XANES probes the unoccupied but bound states by the excitation of a core-shell electron into a valence state. As the dipolar transition is dominant, the difference in the angular momentum quantum number of the core and the valence shell is usually $\Delta L = \pm 1$. The processes dominating the line shape are also dependent on the transition. While transitions between shells with small principle quantum numbers (e.g. K edge) are dominated by the density of states of the valence band, the transition between shells with higher principal quantum numbers (e.g. M edge) is dominated by the multiplet structure caused by the interaction of the core hole with the valence electrons [120, 121]. A deeper insight into how the chemical environment and the local electronic structure influence the multiplet structure and therefore the fine structure is given in section 3.6.

Experimentally, XAS can be measured with different methods. While classic absorption, i.e. transmission measurements, can be applied for thin samples and high photon energies, fluorescence and total electron yield (TEY) make use of secondary processes. In TEY the excited states decay in secondary processes, mainly Auger, leading to the emission of electrons from the sample into the vacuum. The sample is virtually grounded via a current amplifier and the measured current is proportional to the number of absorbed photons [122]. This relation only holds for an X-ray penetration depth much larger than the mean electron escape depth, valid for all our monolayer and sub-monolayer systems [123]. As the mean free path of such secondary electrons is in the nanometer range, this method is highly surface sensitive and therefore used in this work. A limitation of this method is the necessity of a conductive substrate.

3.4. X-ray Magnetic Circular and Linear Dichroism

The high potential of XAS is revealed, as soon as one includes polarization in the experiment. By using circularly polarized light, magnetic properties of the sample can be measured element-specifically and by utilizing linear polarized light, charge anisotropies of the investigated electron shell are exposed.

X-ray magnetic circular dichroism (XMCD) is based on the magnetisation-dependent absorption of circularly polarised light. A circularly polarized photon has an angular momentum of $\pm\hbar$ dependent on the polarisation direction (left/right). Its angular momentum is transferred to the excited electron during the absorption process, leading to different transition probabilities for the two polarisations. While calculating these transition probabilities is relatively simple in the case of $L_{2,3}$ -edges, it gets rather complex for $M_{4,5}$ edges [124]. For simplification, the case of $L_{2,3}$ -edges of Co is presented in Fig. **3-1**.

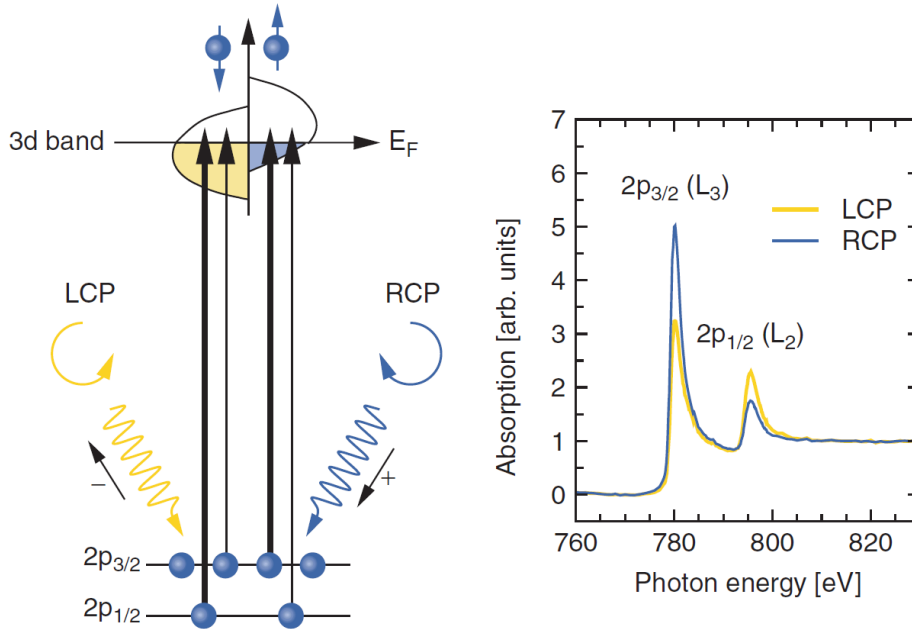


Figure 3-1.: Left: Sketch of the adsorption processes of left and right circular polarized light (LCP/RCP) by a magnetised sample at the Co $L_{2,3}$ -Edge. The line thickness represents the transition probability. Right: Absorption spectra for LCP and RCP of the $L_{2,3}$ -Edge of Co. Adapted from Ref. [119]

The magnetisation of the sample leads to a relative shift of the states close to the Fermi level depending on their spin. Combined with the different transition probabilities, this leads to a dichroic signal in the X-ray absorption. Although theoretically proposed in 1975 [125] and experimentally verified in 1987 [126], the breakthrough of this technique was the establishment of sum rules [127, 128], which allow to quantitatively measure the magnetic moment and disentangle the contribution of the spin and orbital magnetic moments. The resulting magnetic moments are hereby the projection of the moment along the beam direction.

The sum rules are well defined for all transitions (comp. Ref [128]), but we will focus on the sum rule for the $M_{4,5}$ edges in this work. At this point, it is important to state, how XANES and XMCD are defined in this work. The XANES is defined as the average of left- and right-circularly polarized light $(\sigma^+ + \sigma^-)/2$, whereas the XMCD corresponds to the difference $(\sigma^+ - \sigma^-)$. This is only valid under the approximation of a neglectable linear magnetic dichroism. The sum rules for a transition from the $3d$ - to the $4f$ -shell are dependent on the integral of the XANES r , the XMCD of the M_5 edge p , and the XMCD of the M_4 edge q . The expectation value of the angular momentum along the z -direction $\langle L_Z \rangle$ is defined as

$$\langle L_Z \rangle = \frac{2(p+q)}{r} n_h \quad (3-2)$$

and the expectation value of the effective spin $\langle S_Z^{\text{eff}} \rangle$ as

$$\langle S_Z^{\text{eff}} \rangle \equiv \langle S_Z \rangle + 3\langle T_Z \rangle = \frac{2p - 3q}{2r} n_h \quad [128]. \quad (3-3)$$

n_h is the number of holes in the $4f$ shell and $\langle T_Z \rangle$ corresponds to the dipolar term.

The dipolar term is not neglectable for a number of $4f$ metals. One approach is to calculate the T_Z term with the help of a multiplet code. Alternatively, one refers to literature values e.g. Teramura et al. [129]. In the special case of Dy^{3+} one can make use of $\frac{\langle S_Z \rangle}{\langle L_Z \rangle} = 1$ leading to $\langle T_Z \rangle = \frac{-5q}{6r} n_h$ [130].

The relationship between the projected magnetic moments and the expectation values along the quantization axis z is given as $\mu_l = -\langle L_Z \rangle \mu_B$ and $\mu_s = -2\langle S_Z \rangle \mu_B$.

The XMCD magnetisation curves in this work were obtained by evaluating the maximum of the XMCD response at given photon energy as a function of the external magnetic field normalized to the pre-edge intensity.

Similar to XMCD, X-ray linear dichroism (XLD) makes use of the polarisation dependent absorption of light. The observation of XLD generally indicates an asymmetry in the electron charge density of the probed shell. Differing from the sum rule employed in XMCD, there is not an easy way to quantitatively describe the charge anisotropy based on XLD spectra. Conclusions can be drawn out of the comparison of the experimental spectra with theoretically calculated ones. XLD can be split into X-ray natural linear dichroism (XNLD) and X-ray magnetic linear dichroism (XMLD). XNLD probes the intrinsic charge anisotropy of the measured sample, which could be caused e.g. by the crystal field, while XMLD tracks the response of the charge density on an external or intrinsic magnetic field. This allows to investigate e.g. the domain structure of antiferromagnetic materials [131].

A more detailed introduction to this topic is given in Ref. [119] and Ref. [132].

3.5. X-ray Photoelectron Spectroscopy

The x-ray photoelectron spectroscopy (XPS) is a versatile method for element-specific studies of surfaces and interfaces. Based on the photoelectric effect, firstly discovered by Hertz in 1887 [133] and explained by Einstein in 1905 [134], who was awarded with the Nobel Prize in 1921, XPS utilizes the electrons excited by a monochromatic x-ray source. The spectroscopy of the emitted electrons reveals their binding energy. The binding energy is not only element specific, but also contains information about the oxidation state and the chemical environment of the emitting atom. Limited by the mean free path of the excited electrons in the material, this method is surface sensitive. By varying the photon energy or repeated ion sputtering, even a depth dependent measurement can be realised [135].

Typical x-ray sources in the lab use Mg- and Al- and Cu-anodes, leading to linewidths for K_α emission below 1 eV (2.55 eV for Cu K_α), sufficient for standard XPS measurement.

Using synchrotron radiation as a source allows more complex measurements, e.g. angle-resolved photoemission spectroscopy and photoemission tomography.

The emitted electrons are usually detected by a hemispherical electron-energy analyser. It consists of several electronic and magnetic lenses followed by a hemispherical capacitor leading to a CCD detector. The energy resolution can be controlled by the pass energy, which defines the energy range of the electrons allowed to reach the detector.

Using an Al- K_α source with a photon energy of $h\nu = 1486,6$ eV, we are effectively able to measure the $3d_{5/2}$ and $3d_{3/2}$ of the rare-earth elements up to Dy, while most of the remaining elements are covered.

As stated above, XPS element specifically provides information about the oxidation state and the chemical environment, e.g. chemical binding or doping. To extract this information out of the experimental spectra, a spectral analysis of the peaks can be performed. In addition to the chemical environment and the oxidation state, XPS allows a quantitative analysis of the atomic ratio of the sample, making it a versatile tool not only widely used in physics, but also in chemistry, biology, and other disciplines. A more detailed introduction in XPS is provided in Ref. [136].

3.6. Multiplet Calculation

As described above, the comparison of the X-ray absorption spectra with theory is one way to extract additional information out of experimental results. In this section we will briefly introduce the basics of multiplet calculations followed by a more detailed introduction to the special features of the multiX code [16] used in this work.

For nearly 100 years it has been known, that the energy levels of electrons in an open shell form multiplets under the effect of electron-electron interaction, spin-orbit coupling, and the crystal field [137]. Although many aspects of the splitting could be discussed by making use of symmetry considerations and a central field model, a quantitative approach was dependent on the development of computers. In the late 1980s, several works calculating X-ray absorption lines and magnetic x-ray dichroism of 3*d*- and 4*f*-metals were published [138, 139, 128], which paved the way to modern multiplet calculations.

In the simplest approach, the multiplet Hamiltonian \mathcal{H}_{mult} for n electrons in an open shell consists of the intra-atomic electrostatic interactions and the spin-orbit coupling.

$$\mathcal{H}_{mult} = \sum_{i,j}^n \frac{e^2}{|\mathbf{r}_i - \mathbf{r}_j|} + \sum_i^n \epsilon_i \quad (3-4)$$

As this description of a free atom alone is mostly not very helpful in describing the reality, additional terms are added to the Hamiltonian if applicable, representing the crystal field, external (magnetic) fields, exchange fields, and ligand hybridisation. A more detailed description of the atomic multiplet theory and the handling of those terms in different codes are given in Ref. [140] and [16, 141, 142].

The result of such calculations does not only reveal the multiplet structure of an atom but is also the basis to simulate absorption spectra using Fermi's Golden rule.

$$I(\omega) \propto \sum_i |\langle \psi_i | \hat{O} | \psi_0 \rangle|^2 \delta(\hbar\omega + E_0 - E_i) \quad (3-5)$$

$|\psi_0\rangle$ is hereby the groundstate and E_0 its eigenvalue, $|\psi_i\rangle$ and E_i all possible eigenvectors and energies of the excited core hole state, and $\hbar\omega$ the energy of the absorbed photon. The transition parameter \hat{O} depends on the polarisation of the incoming light and is therefore decisive for evaluating XMCD or XLD. To compare the spectra with real experiments considering the finite experimental resolution, a Lorentzian broadening has to be applied to the result.

An example of such calculated spectra is presented in Fig. **3-2**. The XANES and XMCD spectra of Tm for different 4*f*-occupations are calculated in an external magnetic field of 6 T and a temperature of 2 K, without crystal field. The temperature is hereby relevant for the occupation of the lowest-lying states only if the energy difference lies within the thermal energy.

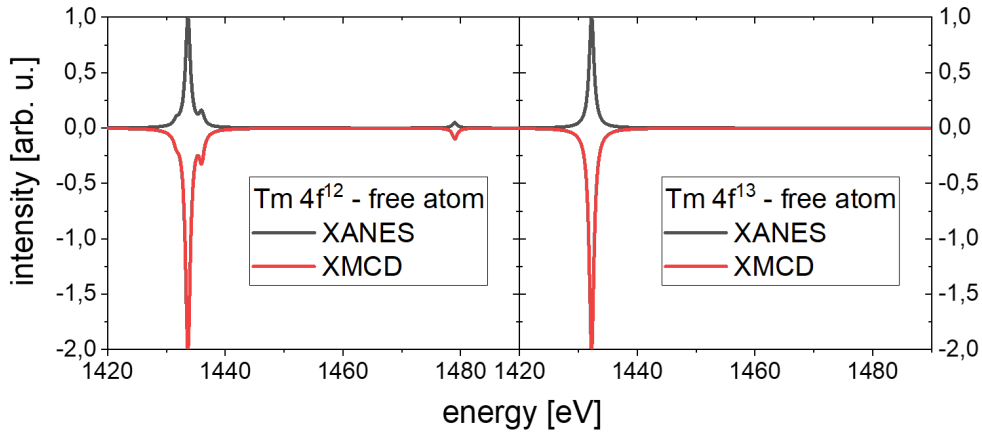


Figure **3-2**: Multiplet calculations of XANES and XMCD spectra of free Tm atoms at a temperature of 2 K and a magnetic field of 6 T for $4f^{12}$ and $4f^{13}$ $4f$ electron configuration, using the multiX code.

The spectra in Fig. **3-2** display the influence of the oxidation state, more exactly the $4f$ -occupation on the fine structure nicely. With a spin moment of $-2\mu_B$ and an orbital moment of $-5\mu_B$ for Tm in the $4f^{12}$ configuration ($\mu_S = -1\mu_B$ and $\mu_L = -3\mu_B$ for $4f^{13}$), the calculated values are in line with Hund's rule.

If one now wants to compare the spectra with a real sample, including a crystal field in the calculation is fundamental. While most of the available multiplet codes work with crystal symmetry groups and crystal field parameters, which works fine for most of the bulk samples, the multiX code allows one to create a custom crystal field by utilizing point charges. This allows one to properly simulate crystal fields for broken symmetries, e. g. at the surface. The crystal field potential is hereby given as

$$V_{xtal} = \sum_{m=1}^{N_{ions}} \frac{Q_m}{|\mathbf{r} - \mathbf{R}_m|} \quad (3-6)$$

with a number of N_{ions} point charges Q_m at the position \mathbf{R}_m from the atom [16]. In order to understand how such a crystal field parametrisation is constructed in this work, such a process is presented in Fig. **3-3**.

We start with the DFT results of our structure, in this example case, a graphene-covered Tm 2×2 surface alloy on Ir(111). We extract the position of the neighbouring atoms as well as the total charge out of the DFT structure. It is important to note, that the charge attributed to the point charges does not quantitatively describe the charge of the atoms but rather can be used for qualitative statements [143]. On the right part of Fig. **3-3** such a crystal field parametrisation is presented. Please note, that the central atom is only displayed as a guide to the eye.

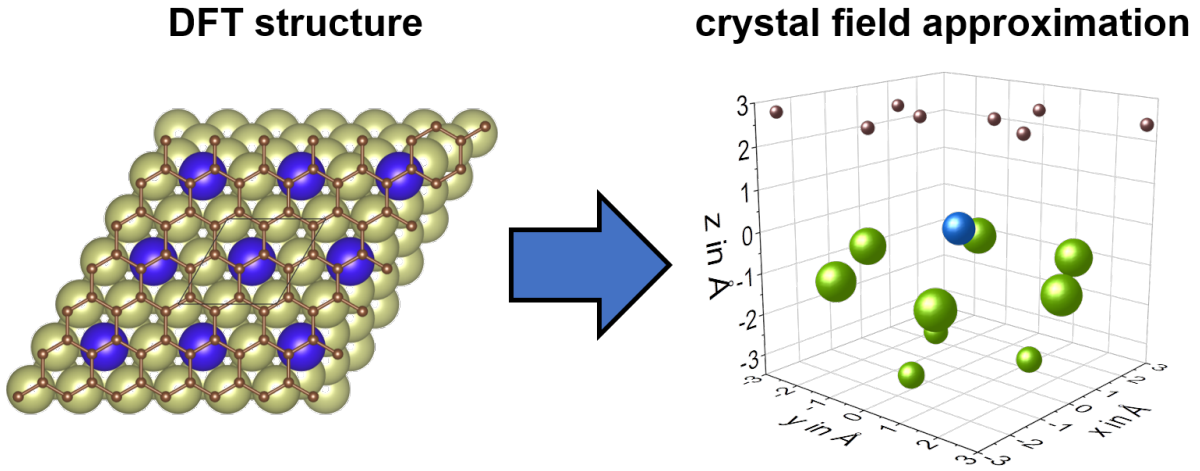


Figure **3-3.**: Left: Top view of the ground state geometry for graphene covered Tm atoms embedded within a (2x2) in-plane unit cell of the first surface layer of Ir(111) calculated by DFT. Right: Representation of point-charge crystal-field scheme employed in the multiplet calculation. The Ir atoms are indicated in green, the Dy atoms in blue, and the C atoms in brown. The size of the spheres in the crystal field scheme represents the charge assigned to its lattice position.

Besides the charge attributed to the atom positions, presented in table **3-1**, there is an additional scaling factor for the crystal field, which is 0.77 in this example.

x (Å)	y (Å)	z (Å)	q (e)	Element	x (Å)	y (Å)	z (Å)	q (e)	Element
1.367	0.789	-3.143	-0.2	Ir	-3.466	-2.001	2.597	-0.1	C
0.008	-1.561	-3.143	-0.2	Ir	-0.726	-2.003	2.588	-0.1	C
-1.348	0.788	-3.143	-0.2	Ir	-0.729	-0.421	2.611	-0.1	C
2.737	-0.005	-0.989	-0.3	Ir	2.014	-0.421	2.587	-0.1	C
-1.373	2.367	-0.989	-0.3	Ir	-2.097	0.372	2.588	-0.1	C
1.390	2.359	-0.995	-0.3	Ir	0.645	0.372	2.610	-0.1	C
-1.373	-2.367	-0.989	-0.3	Ir	0.642	1.955	2.587	-0.1	C
1.390	-2.359	-0.995	-0.3	Ir	3.382	1.952	2.599	-0.1	C
-2.737	-0.005	-0.989	-0.3	Ir					

Table **3-1.**: Crystal field parametrization for the effective ligand field of the graphene-covered (2x2) Tm surface alloy.

To reveal the potential of the crystal field parametrisation by point charges, an example is presented in Fig. **3-4**. We compare the XANES of the M_5 -peak of Tm for different charges attributed to the carbon atoms in our example. In this case, we could qualitatively

compare the attributed charge to the doping level of graphene. It is important to note, that the changes presented here are exaggerated and not expected in nature with this magnitude, but they can nicely show the mechanism behind the change of the fine structure and therefore are ideal for this example.

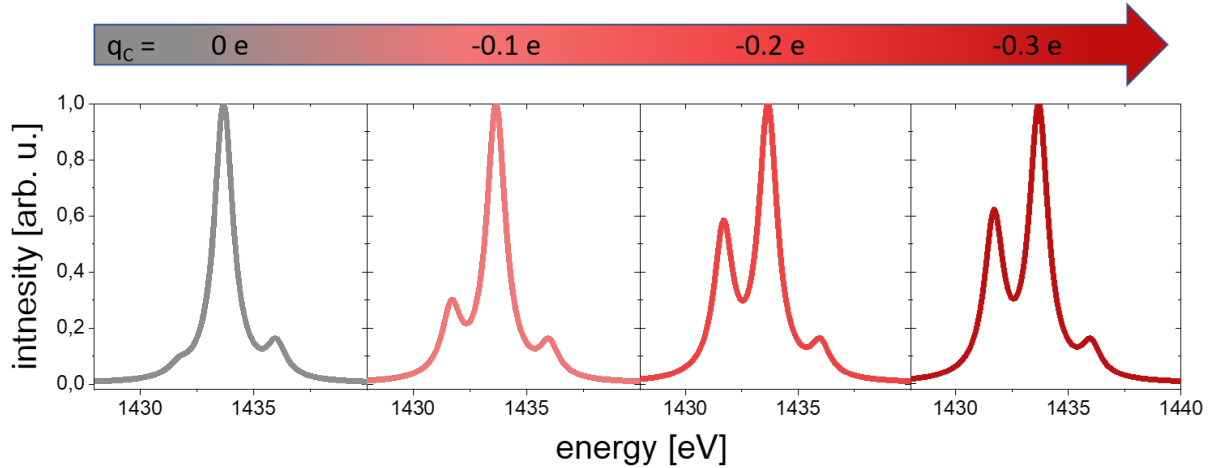


Figure 3-4.: Calculated XANES of the M_5 peak of Tm at $T = 2$ K, $B = 6$ T, and 0° incidence angle for different carbon point charges (q_C) within the crystal field parametrisation defined in table 3-1.

The change in Fig. 3-4 dependent on the assigned charge to the carbon atoms is clearly visible. The intensity of the feature at 1432 eV increases with increasing charge attributed to the graphene. While comparing the experimental results with theoretical calculations, this can be used as an indicator of how strongly the graphene is doped. But one still has to be careful as this is not the only parameter influencing the spectrum. To understand the underlying mechanism, leading to such a drastic change in the fine structure, the multiplet structures of the two extrema are presented in Fig. 3-5.

In Fig. 3-5 the 13 lowest-lying multiplets are presented for both example systems. On the left-hand side, where no charge is assigned to the graphene, the lowest-lying multiplet has an expectation value of $M_J = -6$ which corresponds to the highest magnetisation. It is important to note, that this is only true for a quantisation axis along 0° incidence angle, as always used in this example. Considering a different incidence angle, the expectation value would strongly change, as it considers the moments parallel to the quantisation axis only. Having a closer look at the states, an asymmetry between the states is visible. This is caused by the magnetic field, which splits the states energetically. The size of this splitting hereby depends on the individual states. Another variation from the classic atomic picture is the mixing of states. While this is forbidden in a free atom, the mixing of states is allowed under the influence of a crystal field. As considering all possible mixed states would exceed regular computational power, the technical solution is to consider only the two energetically lowest-lying atomic states of the excited and the partially filled shell for the calculation.

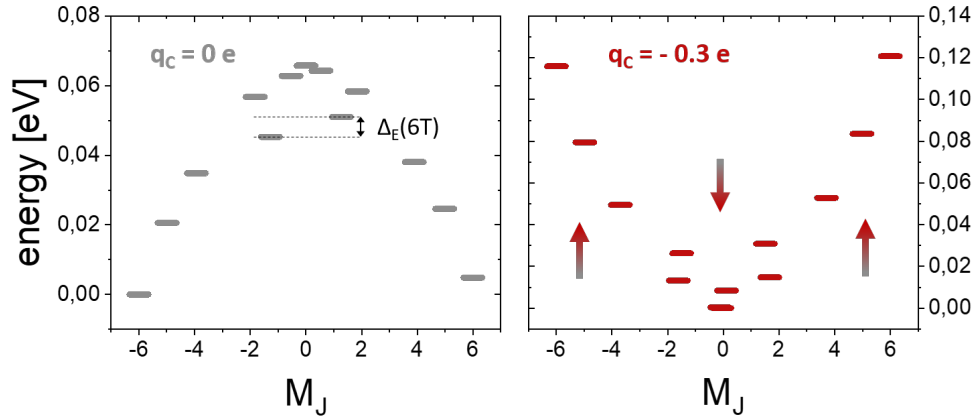


Figure 3-5.: Multiplet level of the example presented in Fig. 3-4 dependent on the expectation value M_J for $q_C = 0 e$ (left) and $q_C = -0.3 e$ (right). The dotted line represent the energy shift of a particular splitted state due to the external magnetic field. The arrows indicate the energetic shift of the states due to the additional charge.

Comparing the multiplet structure with the one of strongly doped graphene on the right-hand side of Fig 3-5, a strong variation between the two structures is visible. The arrows indicate that the states with a higher expectation value are energetically less favourable, whereas the values with low expectation values are favoured. These different states of the Tm are directly represented in the shift in the fine structure presented in Fig. 3-4. Considering the magnetism, we see a drastically reduced magnetic moment perpendicular to the surface in the case of strongly doped graphene, whereas we see a strong magnetic moment for the case without assigned charge to the carbon atoms. In other words, the magnetic anisotropy of this system drastically changes with its changing crystal field. Although we used exaggerated changes of the crystal field within this example, it could nicely show the mechanisms and the opportunities of multiplet calculations and the crystal field approach implemented in the multiX code to simulate our experimental spectra.

3.7. Experimental Setups

Several UHV systems have been used in this work. The investigation of the growth, the structural characterisation, and the XPS measurements of the surface systems have been conducted in the so-called "BESSY" chamber in the workgroup of Prof. Heiko Wende in Duisburg. For the STM experiments, TuMA II of the workgroup of Prof. Thomas Michely in Cologne was used.

A higher variation of UHV systems was present at the different synchrotron facilities, namely X-Treme at the SLS, Deimos at SOLEIL, and VEK MAG at BESSY II. In this section, the BESSY chamber and the X-Treme beamline and endstation are described as representatives for a home lab and a synchrotron setup.

BESSY Chamber

The UHV system BESSY chamber was named after the synchrotron BESSY II, as it was designed as a portable XMCD measurement setup that could be attached to a user beamline. In this thesis, the chamber was only used in the home lab.

The chamber is equipped with a manipulator, that allows liquid helium cooling of the sample down to 20 K and heating via an electron beam up to 900 K. The temperature is controlled by two type K thermocouples and a feedback loop. A flashing stage provides temperatures up to 1600 K, calibrated with a pyrometer. The sample, in our case a single crystal, is mounted on a molybdenum sample holder. Up to three samples can be stored in the garage provided in the transfer chamber. This transfer chamber allows changing the samples without baking the whole system. For the preparation of the sample, an ion sputter gun is mounted. For graphene and nanowire growth, three leak valves are connected to the chamber providing molecules and gases. A quadrupole mass spectrometer with a mass range up to 350 e/u is attached to check the molecules. The chamber has three ports connected with a gate valve, which allows the installation of evaporators with only partial bake-out. Triple and single e-beam evaporators have been used for Tb, Dy, Ho, and Tm and a Knudsen cell was utilized for Eu, Tm, and Yb. The evaporation rate is calibrated by a quartz balance.

In order to analyse the sample, an MCP-LEED, an Auger electron spectrometer and an XPS setup is mounted. The XPS setup consists of a regular X-ray source with Al and Mg anode and a hemispherical electron analyser. The X-ray source and the analyser have a fixed angle of 90°. All measurements conducted in this work used the Al K_{α} source with a constant power of 200 W ($U = 15$ kV, $I_{em} = 13.33$ mA) unless stated otherwise.

X-Treme Beamline and Endstation

The X-Treme beamline and endstation at the Swiss Light Source (SLS) will be described as an example for our synchrotron-based measurements. There are small variations between the different endstations. A detailed description for the DEIMOS beamline and endstation is given in Ref. [144] and for the VEKMAG beamline and endstation in Ref. [145, 146]. The X-ray source of X-Treme is an elliptical undulator, which allows energies from 150 – 8000 eV polarized circularly and vertically [147]. After a collimating mirror, followed by a monochromator the photons pass a focusing mirror as displayed in Fig. 3-6. After passing the exit slit and a refocusing mirror, the photons reach the sample at the endstation. The monochromator defines the energy but limits the range to < 2000 eV due to technical reasons, while the exit slit limits the intensity of the beam. The refocusing mirror can be removed in order to defocus the beam, which is used for delicate samples e.g. organometallic nanowires.

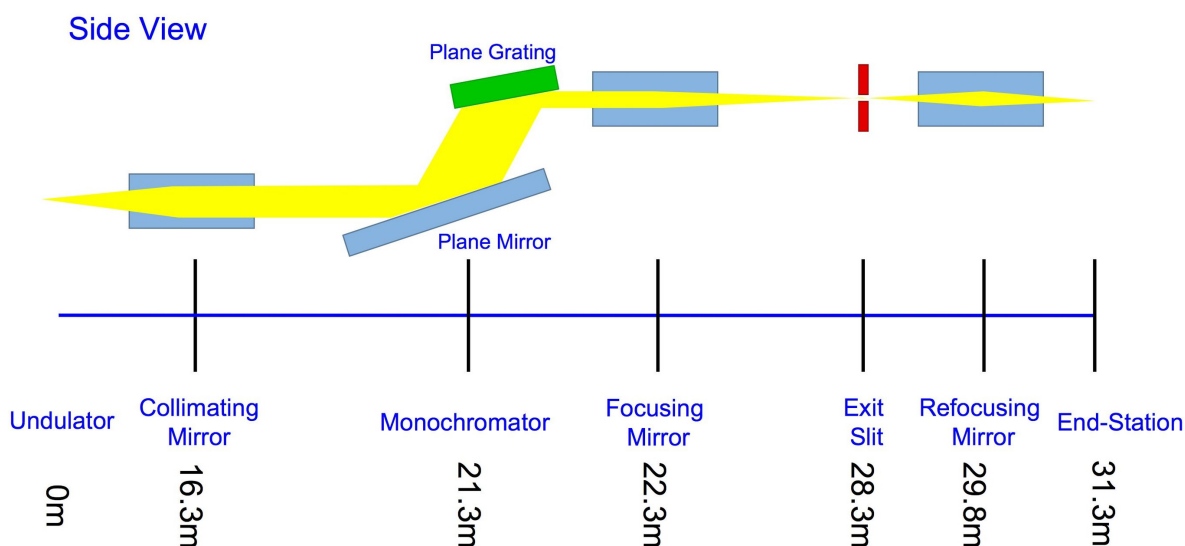


Figure 3-6.: Side view of the X-Treme schematic optical layout. Adapted from [147].

An endstation for such surface science experiments has to combine both, a classical XMCD endstation with a preparation chamber, as the samples have to be grown and measured in-situ. To cover all the needs the X-Treme endstation consists of 4 separate chambers, which are connected to each other. The preparation chamber is equipped similarly to the BESSY chamber described above. A detailed description is provided in Ref. [147]. In addition, an STM chamber with an Omicron STM and a sample garage is attached. The synthesized and pre-characterized samples can be transferred into the cryostat via a transfer chamber, which is connected to a load-lock as depicted in Fig. 3-7.

The He bath-cryostat consists of a pair of superconducting magnets, providing fields up to 7 T along the beam direction and 2 T perpendicular to it. The temperature range for the measurements is 2 K - 350 K and besides the TEY, fluorescence and transmission can be acquired in parallel.

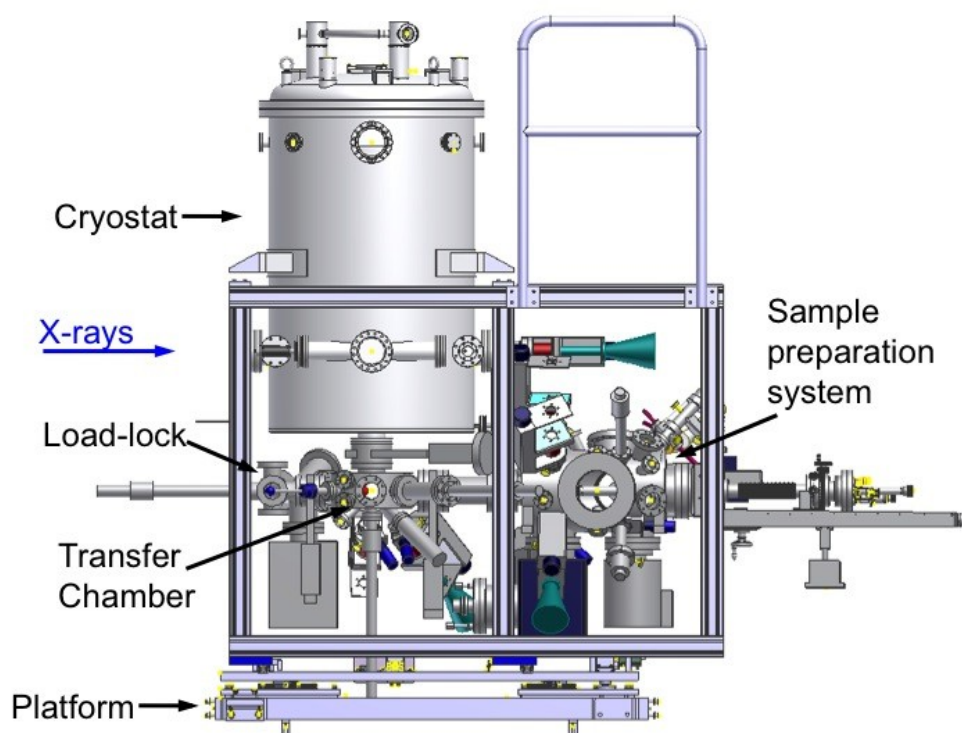


Figure 3-7.: Technical drawing of the X-Treme endstation. Adapted from [147].

4. Graphene-Covered $4f$ Surface Alloys

The work presented in this chapter consists of data and measurements partly published as **A. Herman**, S. Kraus, S. Tsukamoto, L. Spieker, V. Caciuc, T. Lojewski, D. Günzing, J. Dreiser, B. Delley, K. Ollefs, T. Michely, N. Atodiresei, H. Wende. Tailoring magnetic anisotropy by graphene-induced selective skyhook effect on $4f$ -metals [17] and **A. Herman**, S. Kraus, S. Tsukamoto, L. Spieker, V. Caciuc, T. Lojewski, C. Pillich, D. Günzing, J. Dreiser, B. Delley, S. Thakur, C. Luo, K. Chen, F. Radu, K. Ollefs, T. Michely, N. Atodiresei, H. Wende. Tailoring the magnetic anisotropy of $4f$ -surface alloys by graphene adsorption – a systematic study [74]. I contributed the idea, developed the synthesis, and performed all experiments presented in this chapter, besides the structural investigations of the Tm surface alloy (S. Kraus) and the DFT calculations (N. Atodiresei and V. Caciuc). Of course, most experiments can not be accomplished without support. A complete list of all beamtimes and the contributors is given in Appendix B.

In this chapter, we will introduce $4f$ surface alloys on Ir(111), starting with the experimental evaluation of the synthesis and the structure of such surface alloys in section 4.1. *Ab initio* calculations providing the theoretical framework are presented in 4.2. A special focus is set on the magnetic properties and the influence of graphene adsorption on magnetic and electronic anisotropy. Synchrotron-based element-specific measurements are presented in section 4.3, accompanied by ligand-field multiplet theory calculations. Introducing Tb-, Ho-, and Tm- based surface alloys in section 4.4 allows a systematic study of the properties mentioned above. In addition, photo-emission experiments are performed, to reveal the graphene doping level on these surface alloys. A possible application for $4f$ surface alloys as a template for metalloorganic spintronics is presented in chapter 5, section 5.2.

4.1. Synthesis of Graphene-Covered $4f$ Surface Alloys

The idea of evaporating and intercalating Dy on Gr/Ir(111) was based on the interesting results of other $4f$ elements intercalated between Gr/Ir(111). Eu allows the nanopatterning of Gr [44], manipulates the Gr doping level [148], and displays a slightly anisotropic paramagnetic behaviour [45]. Tm and Yb can form an intercalation layer in a similar manner as well [149]. Based on the idea of bringing the magnetically more interesting Dy into play, the

first experiments have been performed. After a few measurements, we realised that there has to be a different mechanism behind this intercalation, as the synthesis parameter to realize a superstructure underneath Gr drastically differs. While Eu forms a full layer underneath graphene [45], Dy forms a surface alloy on Ir(111). The details of this system are presented in the following.

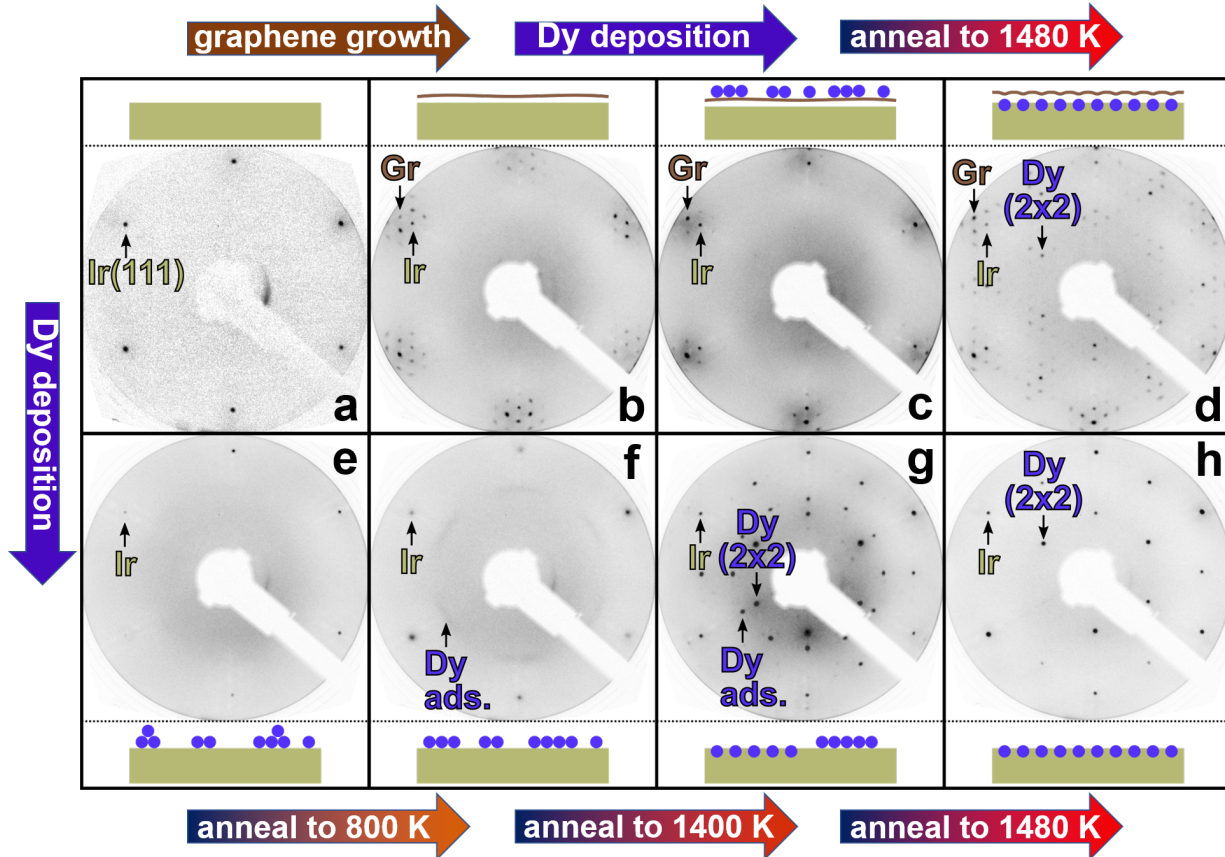


Figure 4-1.: Inverted contrast LEED patterns at 100 eV primary electron energy after the synthesis steps of the (2x2) Dy surface alloy with **a-d** and without Gr **a, e-h**. The arrows indicate the associated LEED spots. Schematic illustrations of the samples are presented next to the LEED patterns. The Ir(111) crystal is depicted in olive, Gr in brown, and Dy atoms in purple. **a** LEED pattern of clean Ir(111); **b** after Gr growth; **c** after the Dy deposition of $0.25 \text{ ML}_{\text{Ir}}$ at 300 K; **d** after sample annealing to 1480 K. **e** LEED pattern after the Dy deposition of $0.25 \text{ ML}_{\text{Ir}}$ at 300 K on the clean Ir(111); **f** after annealing to 800 K, the arrow highlights ring-segment shaped diffraction intensity of Dy adsorption layer; **g** after annealing to 1400 K; **h** after annealing to 1480 K. [17]

Fig. 4-1 presents the synthesis steps for the Dy/Ir(111) 2x2 surface alloy (Fig. 4-1 (a, e-h)) and the graphene-covered surface alloy (Fig. 4-1 (a-d)). Fig. 4-1 a displays the LEED pat-

tern of a clean Ir(111) surface. The olive rectangle in the sketch represents the Ir crystal. As next step, Gr is grown on the Ir(111) surface, according to the TPG+CVD method described in Ref. [150]. The graphene, represented as a brown layer in the sketch in Fig. 4-1 b, introduces additional spots in the LEED pattern, corresponding to the Gr and the moiré. Evaporating 0.25 ML_{Ir} Dy onto Gr/Ir(111) slightly diffuses the pattern indicating no order of the adsorbed atoms, as presented in Fig. 4-1 c. Annealing to 1480 K leads to a formation of a (2x2) superstructure of the Dy atoms, which penetrate through the Gr sheet. It is interesting to mention, that this temperature is far above the intercalation temperatures reported for Eu intercalation, hinting at a different process of the superstructure formation. In order to analyse the superstructure formation, experiments without Gr have been conducted.

The evaporation of 0.25 ML_{Ir} Dy on Ir(111) at room temperature indicated in Fig. 4-1 e leads to a more diffuse LEED pattern, similar to the situation on Gr/Ir(111). The annealing to 800 K presented in 4-1 f initiates the ordering of the adsorbed Dy, indicated by the weak diffraction ring with enhanced intensity along with the directions of the first order Ir spots. Further annealing to 1400 K introduces a well-ordered complex pattern. In Fig. 4-1 g a Dy (2x2) superstructure is coexisting with an intermediate adsorbate phase giving rise to 12 spots with an angular separation of 30° and in a $\sqrt{3}$ distance from the (0,0) spot. This intermediate phase disappears upon further annealing to 1480 K. The LEED pattern in Fig. 4-1 h corresponds to a well-ordered (2x2) Dy superstructure on Ir(111).

In order to understand the process which induces the superstructure formation, STM investigations on Dy/Ir(111) before and after annealing have been conducted. The STM topograph in Fig. 4-2 a, corresponding to the LEED pattern in Fig. 4-1 e, presents the Ir(111) surface after the evaporation of 0.125 ML_{Ir} Dy. Due to the high mobility of the adsorbed atoms, the measurement have been taken at 20 K. A Dy adatom gas is coexisting with Dy islands, visible as bright protrusions on the bare Ir(111) surface. The profile in Fig. 4-2 c reveals an apparent height of about 2 Å for the single atoms and 2.8 Å for the islands. This is in line with the spacing of the dense-packed layers in Dy bulk, which have a spacing of 2.82 Å.

In contrast to the non-annealed sample, the annealed sample presented in Fig. 4-2 b does not exhibit high mobility of the adsorbed atoms indicating a stronger interaction with the substrate. Therefore, the measurements could be conducted at room temperature. The Dy atoms are now mainly ordered in islands and display a (2x2) superstructure. The profile in Fig. 4-2 d reveals an apparent height of just 0.5 Å. In addition, dark spots appear next to the Dy islands, which we assign to defects in the Ir surface, induced by the incorporation of the larger Dy atoms. The low mobility, the lower apparent height, the ordering with respect to the Ir lattice, and the stress-induced defects are all indicators, that the Dy incorporated into the surface and replaces an Ir atom in the surface layer, leading to the (2x2) superstructure.

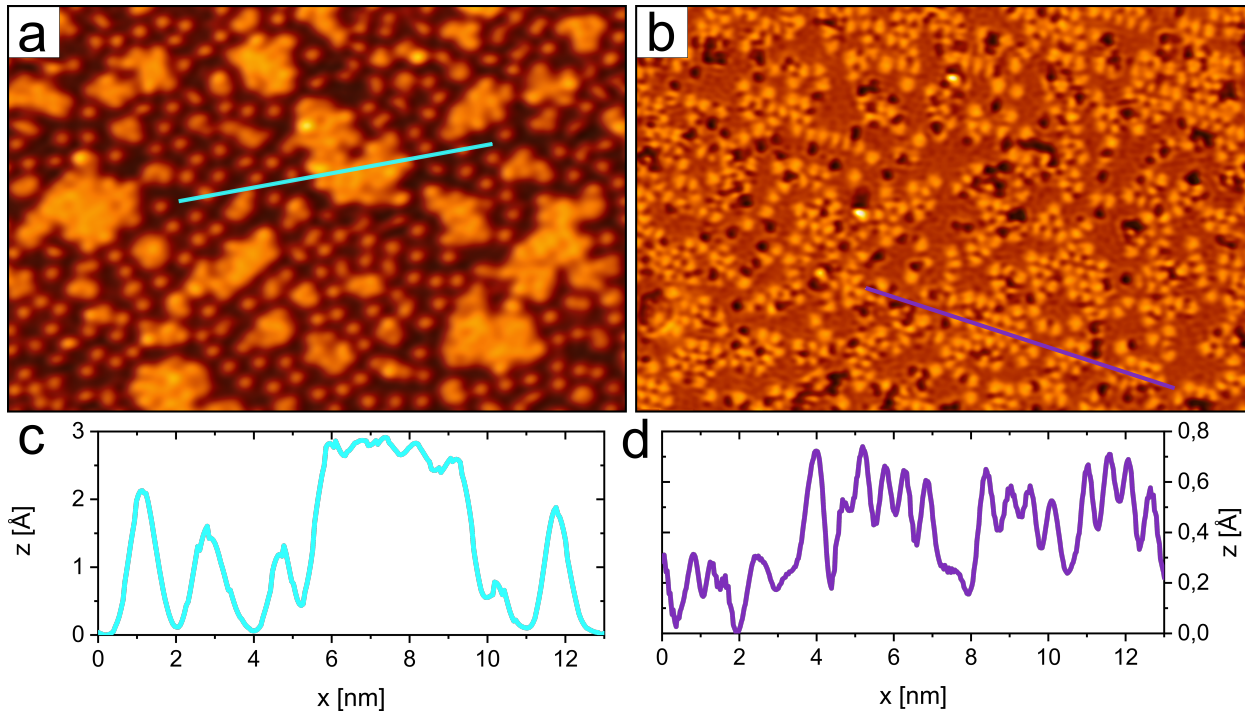


Figure 4-2.: **a** STM topograph after the deposition of $0.125 \text{ ML}_{\text{Ir}}$ Dy on Ir(111) at room temperature ($25.3 \text{ nm} \times 16.6 \text{ nm}$). The turquoise line indicates the profile in **c**. **b** STM topograph after annealing the sample in **a** to 1480 K . ($25.3 \text{ nm} \times 16.6 \text{ nm}$). The purple line shows the profile in **d**. The tunnelling parameters used are **a** $I = 0.15 \text{ nA}$, $U = -2.11 \text{ V}$ and **b** $I = 1.1 \text{ nA}$, $U = -1.05 \text{ V}$. [17]

The STM topograph in Fig. 4-3 **a** allows the direct comparison to the complete (2×2) surface alloy in Fig. 4-3 **b**. For full coverage, the order of the (2×2) Dy surface alloy increases compared to the surface alloy patches. The structure is more regular and surface defects are not present anymore. The (2×2) superstructure is nicely visible when comparing the surface alloy to the atomic resolution STM topograph of a bare Ir(111) surface in the inset. The Ir can not be resolved in presence of the Dy surface alloy.

A similar comparison for the graphene-covered sample is given in Fig. 4-3 **c**, **d**. The patches of the surface alloy underneath Gr in Fig. 4-3 **c**, visible as dark depressions, form mainly islands of the (2×2) surface alloy underneath Gr, similar to Fig. 4-3 **a**. The Gr lattice is visible throughout and is incommensurate with the (2×2) superstructure, which is in line with the results of the LEED pattern in Fig. 4-1 **d**, which showed that the Dy orders with respect to the Ir(111) surface, not the Gr. The areas of larger surface alloy islands appear brighter, which could be attributed to a reduced work function caused by doping of the Gr layer. The high quality of Gr similar to Gr/Ir(111) is still maintained.

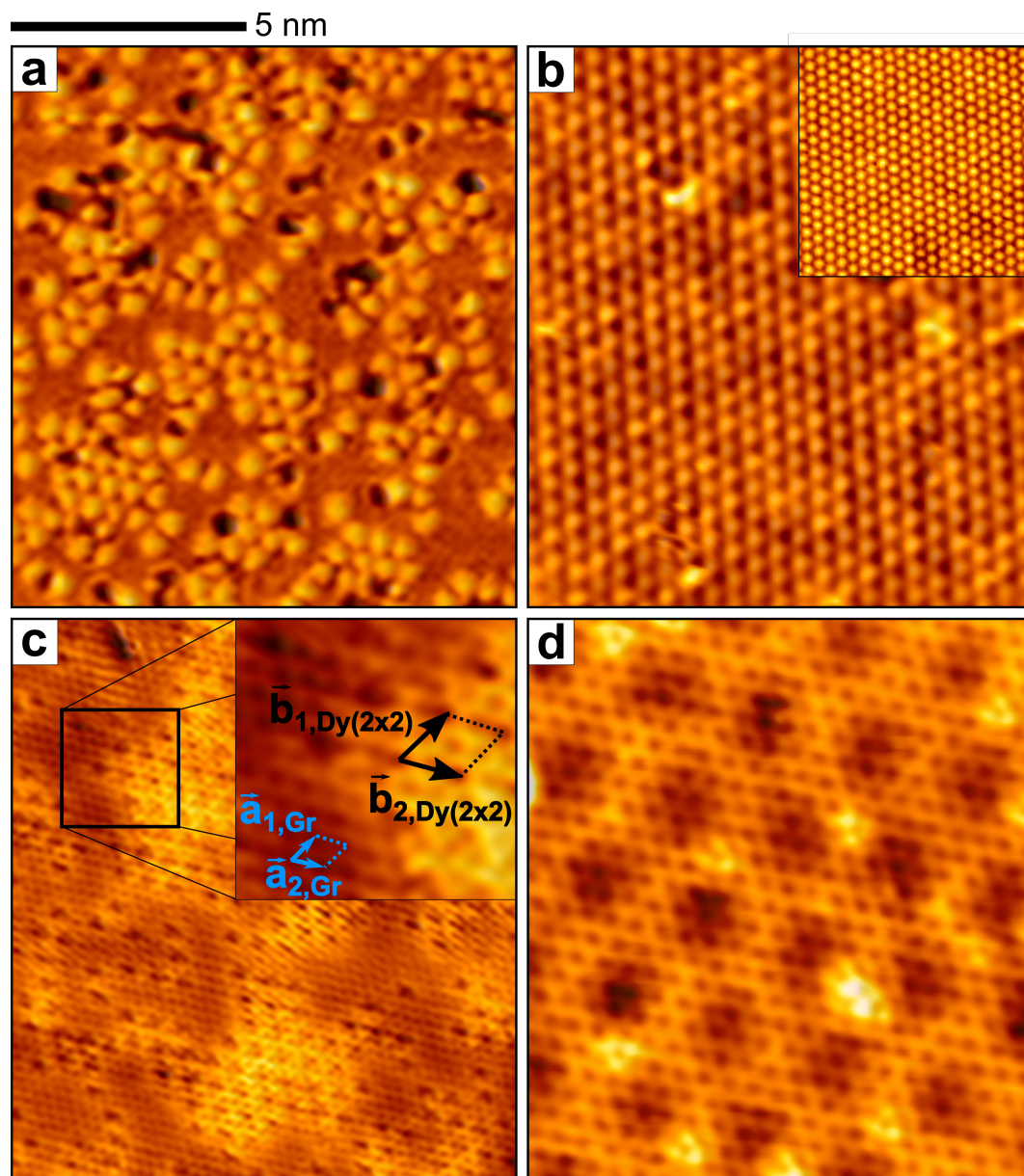


Figure 4-3.: **a** STM topograph of (2x2) Dy surface alloy patches. **b** STM topograph of a complete (2x2) Dy surface alloy. Inset: atomic resolution STM topograph of clean Ir(111). **c** Atomic resolution STM topograph of (2x2) Dy surface alloy patches under Gr. Primitive cells of Gr and the surface alloy are indicated in the zoom-in. **d** STM topograph of a complete (2x2) Dy surface alloy under the Gr cover. (Topograph sizes are $10.8\text{ nm} \times 12\text{ nm}$, inset is $5\text{ nm} \times 5\text{ nm}$, zoom-in is $2.5\text{ nm} \times 2.5\text{ nm}$). The tunnelling parameters used are **a** $I = 1.1\text{ nA}$, $U = -1.05\text{ V}$, **b** $I = 0.5\text{ nA}$, $U = -1.68\text{ V}$, inset $I = 50\text{ nA}$, $U = -0.005\text{ V}$, **c** $I = 30\text{ nA}$, $U = -0.09\text{ V}$, and **d** $I = 5\text{ nA}$, $U = -0.50\text{ V}$. [17]

The complete (2x2) Dy surface alloy presented in Fig. **4-3 d** displays a well-ordered surface with a few bright point defects. In addition to the (2x2) superstructure, the moiré of Gr with its substrate is visible. This moiré pattern, similar to the one of Gr/Ir(111) indicates, that the Gr did not exhibit a significant structural change, which sustains its favourable properties as a substrate for organometallic on-surface synthesis, as presented in section 5.2. In addition, the Gr is expected to act as passivation layer, which prevents the reactive *4f* metal from oxidising. This would allow to utilize the outstanding *4f* properties outside of UHV conditions, which is crucial for future applications and has not been reported for other *4f* surface alloys so far.

4.2. *Ab Initio* Calculations of the Graphene-Covered Dysprosium Surface Alloy

In order to understand the alloy formation and to support our experimental findings, we performed *ab initio* DFT calculations. The first question, which appears after the structural analysis, is if the surface alloy formation is confirmed to be energetically favourable, as proposed in section 4.1. Two different configurations have been analysed, Dy on top of the Ir(111) surface (Fig. 4-4 a, b) and incorporated into the first surface layer (Fig. 4-4 c, d). Analogue, the graphene covered samples have been probed, with an intercalated Dy layer (Fig. 4-4 e, f) and a graphene-covered surface alloy (Fig. 4-4 g, h).

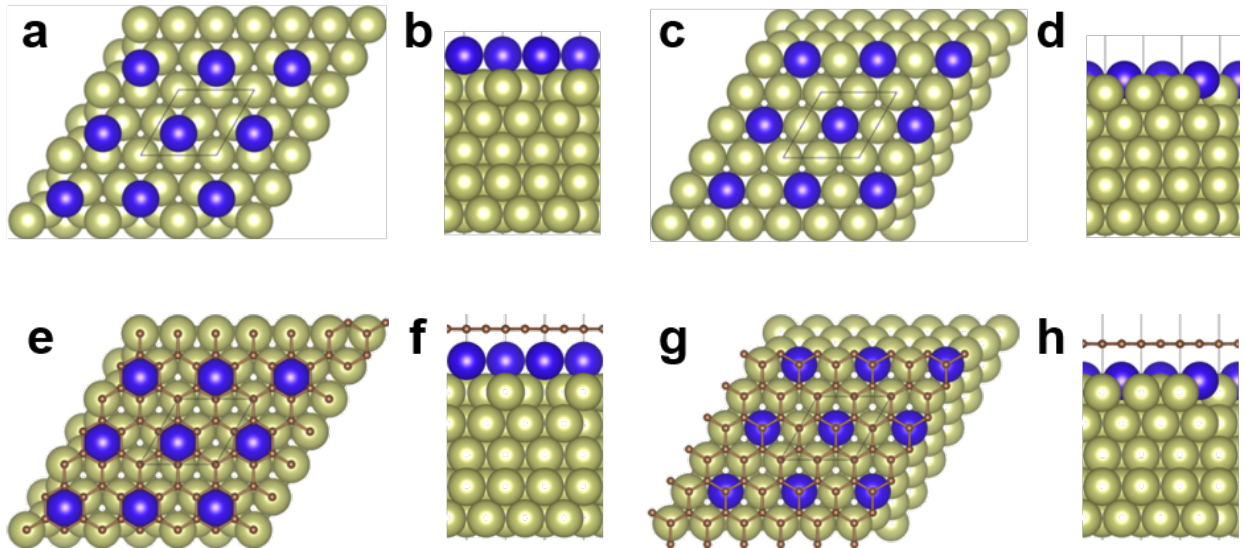


Figure 4-4.: **a** Top and **b** side views of the ground state structures for a Dy atom adsorbed above Ir(111) surface and **c**, **d** embedded within the surface layer of the Ir(111) substrate. The calculated in-plane (2x2) unit cell is indicated by the black lines. With respect to the first Ir layer, when a Dy atom is adsorbed above the surface it is located at 2.055 Å and 0.667 Å when it is embedded within the surface layer. **e** Top and **f** side views of the ground state geometries for a Dy atom intercalated between Gr and Ir(111) surface and **g**, **h** Gr adsorbed onto the surface alloy formed by Dy atoms embedded within a (2x2) in-plane unit cell of the first surface layer of the Ir(111) substrate. With respect to the first Ir layer, when a Dy atom is adsorbed above the surface it is located at 2.251 Å and 0.826 Å when it is embedded within the surface layer. **e**, **f** Gr is 4.508 Å away from Ir substrate and 2.257 Å above the intercalated Dy layer. **g**, **h** Gr is 3.448 Å away from Ir substrate and 2.622 Å above Dy embedded into the Ir(111) surface. [17]

For Dy on Ir(111), embedding Dy into the surface layer in a (2x2) superstructure is energetically preferred by -2.702 eV/atom compared to the adsorption. This is in line with our experimental results. This is also true for the graphene-covered surface alloy, which is favoured by -1.889 eV/atom compared to the intercalation. These rather big energy differences strongly support our interpretation of a surface alloy formation.

A more detailed view of these systems is provided in Fig. 4-5. In the energetically most favourable Dy/Ir(111) surface alloy, the Dy atoms sit 0.667 Å above the Ir atoms. The charge density difference (CDD) plot presented in Fig. 4-5 c cuts through the [1-10] direction which corresponds to the long diagonal of the unit cell indicated in Fig. 4-5 a. The CCD between the sum of the isolated parts and the combined system reveals a charge accumulation above the Dy atom and a depletion below, which is expected due to the Coulomb interaction. Interestingly, the change at the Ir sites is relatively small.

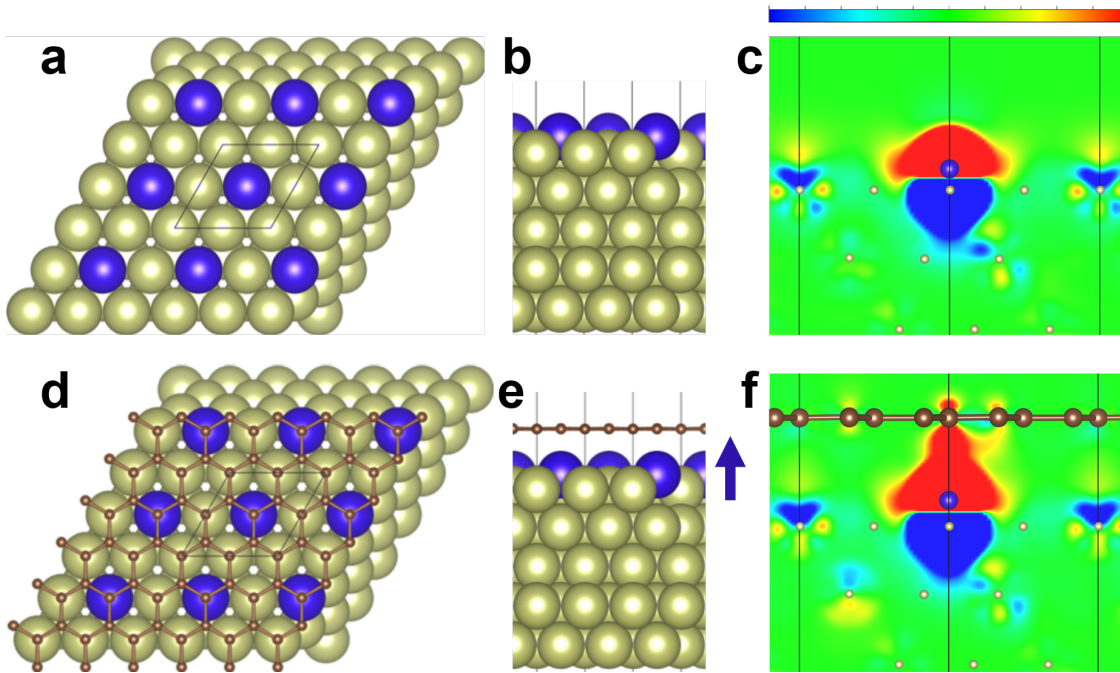


Figure 4-5.: **a, d** Top and **b, e** side views of the ground state geometries for Dy atoms embedded within a (2x2) in-plane unit cell of the first surface layer of the Ir substrate **a, b** and Gr adsorbed onto the surface alloy **d, e**. The calculated in-plane (2x2) unit cell is indicated by the black lines. With respect to the first Ir layer, the Dy atom sits 0.667 Å above the clean surface alloy, by adsorbing Gr onto the substrate the Dy atom is lifted 0.826 Å above the surface. The arrow indicates the lifting. Gr is 3.448 Å away from the Ir substrate and 2.622 Å above Dy embedded into the Ir(111) surface. **c, f** Charge density difference cuts plotted through the [1-10] direction in the absence **c** and presence of Gr **f**. The colour scale bar indicates a charge depletion from -0.008 e/Å³ in blue to a charge accumulation of 0.008 e/Å³ in red. [17]

For the graphene-covered sample, the top position is energetically most favourable, but the other positions show qualitative equal results. The different positions and the handling of the incommensurate graphene lattice will be discussed below at Fig. 4-6. The Dy atoms are lifted 0.826 Å above the Ir. This selective lifting is also represented in the CCD plot. While the charge density shows no significant change around the Ir atoms, the situation at the Dy drastically changes. There is a charge accumulation between the Dy and the Gr, indicating a chemical binding. Around the carbon atoms above the Dy, an increased charge density can be observed, resembling π -like orbitals. The lifting of the Dy is similar to the skyhook effect induced by molecules [151]. Due to the repulsive chemical interaction (Pauli repulsion) between Gr and Ir(111), the physisorbed Gr is located high above the Ir surface [33]. The attractive chemical Gr-Dy interaction leads to a lifting of the Dy by 0.16 Å. Due to this element-specific lifting, we call this effect the "selective skyhook effect".

The additional charge attributed to the C atoms leads to an n-doping of the graphene. It is interesting to notice, that in- and out-of-plane charge gradients can have a drastic impact on the magnetisation direction in systems with large spin-orbit coupling, due to the surface spin-split Rashba states [152].

As graphene and its interaction are crucial in this system, it makes sense to look at the base of the calculations in more detail. Gr/Ir(111) has an incommensurate superstructure of (10.32×10.32) Gr unit cells on (9.32×9.32) Ir unit cells, as described in section 2.1. Due to the limitations of calculation time, a simplified unit cell was used, slightly changing the Gr lattice parameter. While the influence of the changed lattice parameter should be rather small, the relative position of the C atoms to the Dy might be relevant. Due to the incommensurate lattices in the real sample, the Dy could be covered by a C atom atop, at bridge, in center of a carbon ring, or anything between. To take this into account, we performed DFT calculations for all the high symmetry positions.

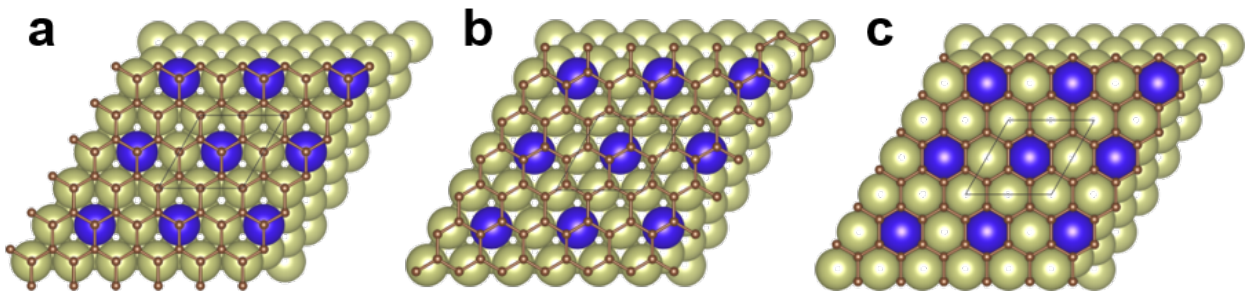


Figure 4-6.: The three different configurations probed in the calculations. The carbon atoms are placed **a** atop, **b** with the bond, and **c** with the hexagon above the Dy atoms. [17]

From the three Gr configurations presented in Fig. 4-6, the atop configuration is the energetically most favoured one. The difference to the hexagon position is negligible (+0.063 eV),

while the bridge position is slightly less favoured (+0.588 eV), which is still far below the energy difference to the intercalated case. Concluding, one can expect, that the real system is well represented by our calculations presented in Fig. 4-5.

A more detailed look at the electronic properties is provided by spin-polarized projected density of states presented in Fig. 4-7. In the embedded system presented in Fig. 4-7 **a** new hybrid electronic states are formed at the Dy site in both spin-channels. These hybrid states have either a large $5d$ and a minor $4f$ contribution, or a significant $4f$ and small $5d$ character. While a hybridisation would be forbidden in the isolated atom, the modification of the chemical environment allows so. The projected total charge density (and effective magnetic moment) on the Dy atoms in the surface alloy account for 0.24 (+0.02 μ_B) in $6s$, 1.01 (+0.06 μ_B) in $5d$, and 9.24 (+5.11 μ_B) in $4f$.

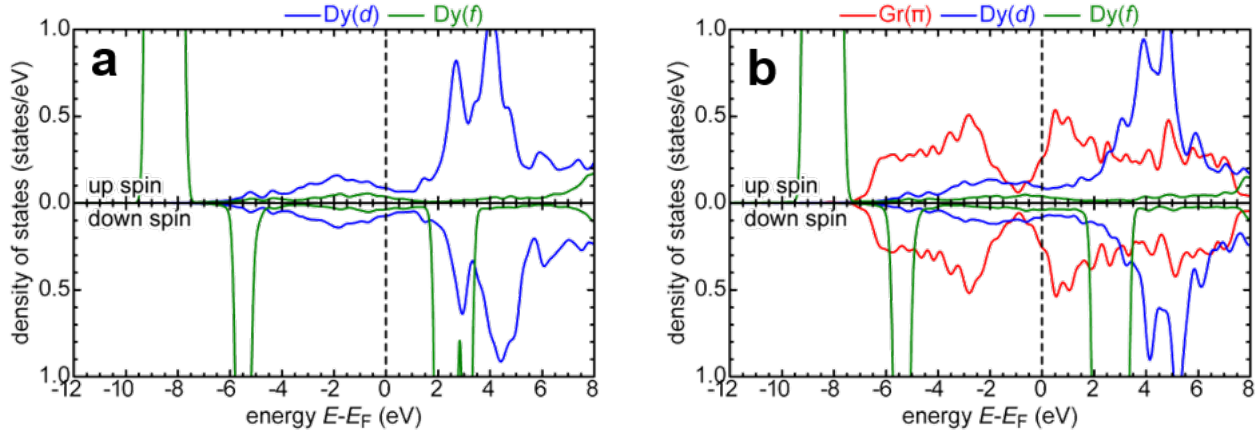


Figure 4-7.: The spin-polarized projected density of states for the **a** clean and **b** graphene-covered embedded Dy/Ir(111) substrate. The Gr π -like orbitals are plotted in red colour and refer to the projection of the electronic states of the hybrid system into the p_z -like atomic orbitals of the C atoms building the Gr layer. The projection of the electronic states of the combined system onto the Dy atomic-like orbitals are plotted with a blue line on $5d$ -states while the $4f$ -states are indicated by the green line. [17]

In the graphene-covered sample presented in Fig. 4-7 **b**, the $5d$ - $4f$ hybrid states hybridise with the carbon π -like orbitals originating from the p_z atomic like orbitals of the Gr, as indicated in the CDD plots in Fig. 4-5 **f**. This complex hybridisation is enabled by the nature of the $5d$ - $4f$ hybrid states, as they have a strong $4f$ atomic like character close to the Dy nucleus, while the extending tails originate mainly from the $5d$ atomic like orbitals. The long reach of these states allows an overlap and hybridisation with the Gr π orbitals as well as the Ir states. These are also responsible for the Gr doping. The minimum of the Gr π states density, which corresponds to the Dirac-like feature, is shifted to negative energies, indicating an n-doping of the Gr by -0.75 eV. The projection of the total charge density

(and effective magnetic moment) onto a sphere around the Dy atom in the graphene-covered surface alloy leads to 0.26 (+0.02 μ_B) in 6s, 1.03 (+0.06 μ_B) in 5d, and 9.26 (+5.03 μ_B) in 4f.

While there is no significant change in the occupation as well as the effective magnetic moments, the graphene-induced selective skyhook effect, i.e. the interaction with the adsorbed Gr layer, strongly changes the magnetic properties of the system. To explore the changes from a theoretical point of view, calculations with an extended (4x4) in-plane surface cell have been performed. The interaction energies can be extracted by the energy differences between the two systems presented in 4-8.

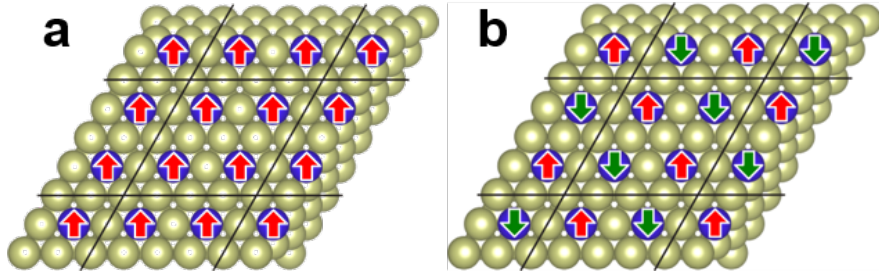


Figure 4-8.: The calculated ferromagnetic **a** and the antiferromagnetic **b** configurations of the Dy atoms in a (4x4) in-plane surface unit cell.

The difference between the two systems, one with ferromagnetic order and one with antiferromagnetic order, varies strongly between the surface alloy and the graphene-covered surface alloy. For the surface alloy, an energy difference of -0.073 eV is given, while the energy difference drastically increases to -1.985 eV for the graphene-covered surface alloy. In order to calculate the exchange coupling constant J of a simple Heisenberg Hamiltonian

$$H_{Heis} = -J \sum_{\langle i,j \rangle} \vec{S}_i \cdot \vec{S}_j,$$

one can derive the energy difference between ferromagnetic and antiferromagnetic configurations as: $E_{FM} - E_{AFM} = (6 \cdot J \cdot M \cdot M) - (-4 \cdot J \cdot M \cdot M + 2 \cdot J \cdot M \cdot M) = 8 \cdot J \cdot M \cdot M$, with M as the spin moment of Dy. This leads to a magnetic exchange constant of 0.36 meV/ μ_B for the clean surface alloy, whereas the graphene-covered surface alloy amounts to 9.93 meV/ μ_B . This drastic increase has, to the best of our knowledge, not been observed for any 4f system. In 3d systems, this effect has only been proposed theoretically, e.g. in Ref. [151, 153, 154].

4.3. Magnetic and Electronic Properties of the Graphene-Covered Dysprosium Surface Alloy

In order to reveal the electronic and magnetic properties of the Dy surface alloy system, we performed synchrotron-based element-specific XAS measurements. By utilizing circularly polarized light combined with applying the sum rules, we investigate the magnetic properties of the Dy $4f$ shell by probing the $M_{4,5}$ edges. Ligand-field multiplet calculations based on the DFT results provide the theoretical background to our experiments. Combining the multiplet results with our linear dichroic measurements allows us to reveal the electronic anisotropy of the $4f$ -shell and provide an experimental fingerprint of the proposed selective skyhook effect.

XANES, XMCD, and multiplet approach

All spectra presented in the following have been recorded at a temperature of 3 K and an external magnetic field of 6.8 T along the beam direction. Fig. 4-9 a shows the experimental XANES and XMCD spectra of the Dy $M_{4,5}$ edge of the surface alloy for normal and grazing incidence. Comparing the XANES to literature and multiplet calculations reveals a $4f^9$ occupation [139]. This is in line with the DFT calculations and indicates a $[\text{Xe}] 5d^1 4f^9$ electron configuration. While the $6s$ electrons are strongly delocalised, one $4f$ electron is promoted to the $5d$ shell due to a metal-metal bond [155]. Similar to the XANES, the XMCD of the surface alloy shows a negligible angular dependence, which is in strong discrepancy to the graphene-covered surface alloy presented in Fig. 4-9 d. While the XMCD signal is drastically reduced for measurements normal to the surface, the grazing incidence measurements display an even higher magnetisation compared to the surface alloy. In addition to the drastic changes in the XMCD, a slight angular dependence of the XANES spectrum is present for the graphene-covered surface alloy. This is on one hand connected to the magnetic anisotropy [156], but on the other hand, it is a strong indicator for a charge anisotropy of the $4f$ shell, which is discussed in more detail below.

Applying the sum-rules introduced in section 3.4, the projected magnetic moments extracted out of the experimental spectra of the surface alloy are given as $\mu_s = -2.15 \pm 0.32 \mu_B$ and $\mu_l = -2.53 \pm 0.38 \mu_B$ for normal incidence and $\mu_s = -2.22 \pm 0.33 \mu_B$ and $\mu_l = -2.51 \pm 0.38 \mu_B$ for grazing incidence. For the graphene covered surface alloy, this changes to $\mu_s = -0.75 \pm 0.11 \mu_B$ and $\mu_l = -0.82 \pm 0.12 \mu_B$ for normal incidence and $\mu_s = -2.84 \pm 0.43 \mu_B$ and $\mu_l = 3.32 \pm 0.50 \mu_B$ for grazing incidence.

An important role, especially for the $4f$ elements, plays the dipolar term T_Z . The contribution of the T_Z term to the spin moment can generally not be derived by the sum rules and therefore must be calculated e.g. by multiplet calculations [129, 157]. Just for the special case of a $4f^9$ configuration, T_Z can be directly derived from the sum rules, utilizing $\mu_s = \mu_l$. This gives us the possibility to validate the T_Z values of our multiplet calculations. In our

case, the deviation between the theoretical and experimental values is smaller than 4% for all measurements, which is below the experimental error. This gives us strong confidence concerning the calculated T_Z values, which can have a massive impact on the spin-moments, as discussed in more detail in section 4.4.

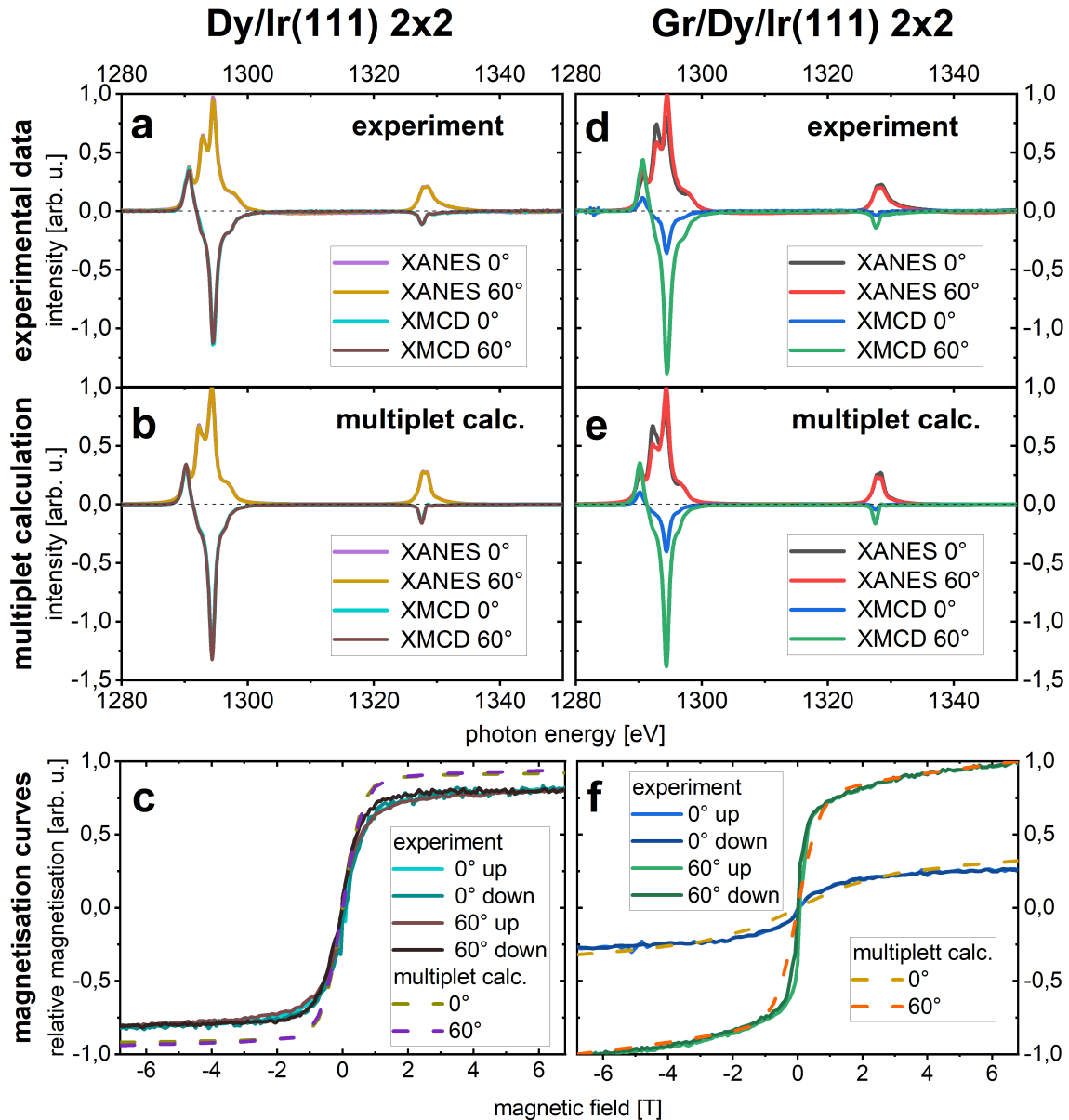


Figure 4-9.: **a, d** Experimental XANES and XMCD of the Dy surface alloy **a** and graphene-covered Dy surface alloy **d** for normal (0°) and grazing (60°) incidence at a temperature of 3 K and a magnetic field of 6.8 T. **b, e** Respective calculated multiplet spectra. **c, f** Experimental and calculated magnetization curves of the two samples normalised to the maximal magnetisation of the graphene-covered Dy surface alloy for grazing incidence. [17]

It is important to note again, that these values correspond to the projected magnetic moment. For example, an in-plane ordered Dy surface alloy would account for an orbital and spin moment of $5 \mu_B$ along the surface plain. Measuring at grazing incidence, this would lead to a projected magnetic moment of $\mu_{proj} = \sin(60^\circ) \cdot 5\mu_B = 2.5\mu_B$.

In order to get a deeper understanding of our system and the magnetic properties, we performed ligand-field multiplet calculations based on the DFT structural results. The simulated XANES and XMCD spectra are presented in Fig. **4-9 b** for the surface alloy and in Fig. **4-9 e** for the graphene-covered surface alloy. By comparing these spectra to the experimental spectra displayed in Fig. **4-9 a, d** a very good fit can be observed, which indicates, that our model represents our real system very well. This also holds for the magnetic properties. The calculated projected magnetic moments of the surface alloy are given as $\mu_s = -2.49 \mu_B$ and $\mu_l = -2.63 \mu_B$ for normal incidence and $\mu_s = -2.37 \mu_B$ and $\mu_l = -2.48 \mu_B$ for grazing incidence and for the graphene-covered surface alloy as $\mu_s = -0.93 \mu_B$ and $\mu_l = 0.94 \mu_B$ for normal incidence and $\mu_s = -2.70 \mu_B$ and $\mu_l = -2.84 \mu_B$ for grazing incidence. These calculated values are all within the experimental error.

Fig. **4-9 c** presents the XMCD magnetisation curves of the surface alloy for normal and grazing incidence. Similar to the experimental finding at 6.8 T, the curves do not vary for the different incidence angles within the experimental error. In addition, they show a typical paramagnetic slope, as a Brillouin function would fit the curves perfectly. The dotted lines represent the multiplet calculation. Besides the slightly higher maxima, an almost perfect fit with the form of the experimental curves is observed. The Dy seems to saturate at an external field of about 2 T.

After the adsorption of Gr, the picture changes drastically. Similar to the XMCD results, a strong anisotropy is present. While the normal incidence measurements displays a saturation at around 2 T at around 1/4 of the maximum value of the grazing incidence measurement, the curve of the grazing incidence measurement displays a very high susceptibility around zero-field and slowly increases at higher fields. This curve deviates from a paramagnetic behaviour. The drift at a higher field, which is nicely reproduced by the multiplet calculations, could be explained by pushing the magnetic moment out of the favoured in-plane orientation by the rising external field, pointing out of the surface plane. Just slightly above and below zero field, the projected value would represent a fully in-plane magnetised sample, as calculated above. Increasing the external magnetic field would force the magnetic moments to align with the magnetic field and therefore the projected magnetic moment increases with increasing field. The magnetisation dependence of the XLD signal supports this interpretation and will be presented and discussed in more detail in Fig. **4-13**.

The second deviation can be found around zero-field. The magnetisation curve exhibits a very steep slope around zero-field. This could hint at a magnetic order, as indicated by the DFT calculations. Due to the negligible in-plane anisotropy of this system, we would expect a coercivity field of just a few mT, as shown for similar systems [62]. This is far below the experimental error of the superconducting magnet at the X-Treme beamline but would

explain the deviation between the calculated and experimental spectra in the low field range. Another hint for the ferromagnetic coupling is presented in Fig. 4-13.

The calculated spectra presented in Fig. 4-9 are based on ligand-field multiplet theory. By utilizing the multiX code [16], we are able to construct a ligand field based on point charges. This provides an advantage over other multiplet codes, as they usually work with crystal-field parameters, which do not represent the situation at a surface properly, due to the broken symmetry. Fig 4-10 **a, b** presents how such a crystal field is realised. The goal is to construct a model system, which is as close as possible to the real structure and represents the electronic and magnetic properties properly.

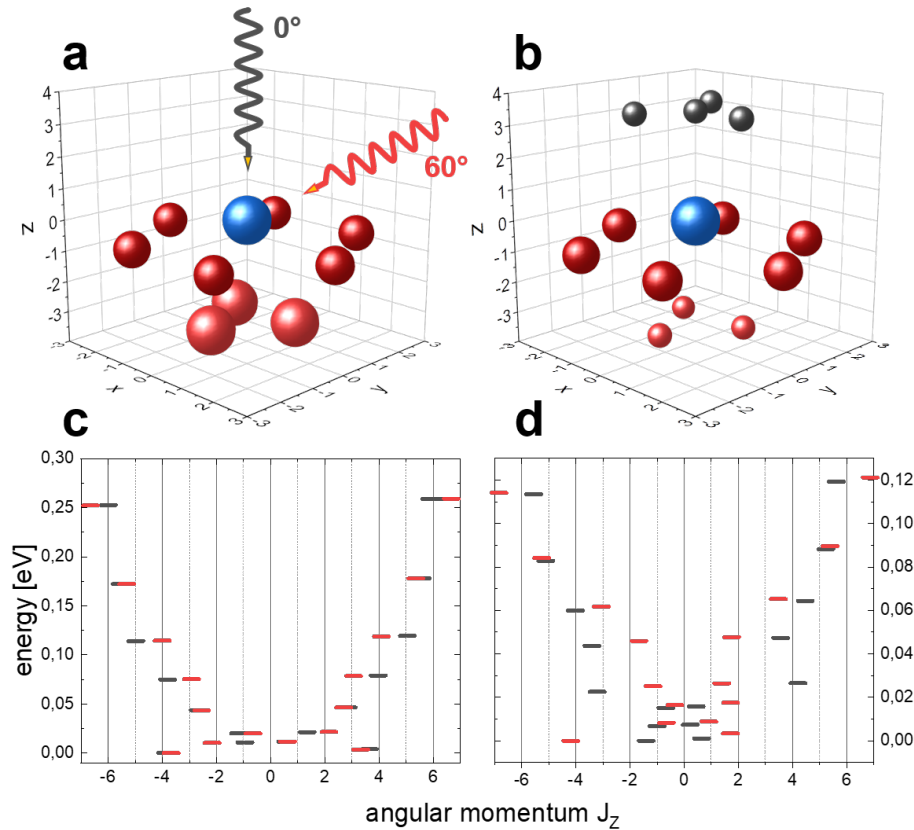


Figure 4-10.: **a** Representation of point charge crystal field scheme employed in multiplet calculation for the Dy/Ir(111) 2x2 surface alloy and **b** the graphene-covered Dy surface alloy. The red spheres represent the Ir atom, the blue sphere the Dy atoms, and the grey spheres the C atoms. The size of the spheres represents the charge assigned to its lattice position. The quantisation axis according to the incoming synchrotron radiation is indicated by the grey (0°) and red (60°) lines. Distances are given in Å. **c** Multiplet level of the surface alloy and **d** graphene-covered surface alloy dependent on the expectation value M_J for normal (grey) and grazing (red) incidence at a magnetic field of 6.8 T.

Fig. **4-10 a** represents the surface alloy. The blue sphere indicates the Dy atom in the centre. The surrounding red spheres represent the Ir atoms. The positions of the Ir atoms are taken from the DFT relaxed structure and the charge is the only "fitting" parameter. The values of the charge are represented in the size of the spheres. All equivalent positions have to have the same charge assigned. As the Dy provides electrons to the surrounding, the charges of the Ir atoms have to be negative. This information is provided by the DFT calculations as well. In addition, the incoming photons are sketched for normal and grazing incidence. The photon direction defines the quantisation axis as well, similar to the experiment.

For the graphene-covered surface alloy, represented in Fig. **4-10 b**, additional carbon atoms represent the adsorbed graphene, indicated in grey. Due to the n-doping, the carbon atoms are also negatively charged. Another change is the elevation of the Dy atom. It is lifted due to the skyhook effect, proposed by the DFT calculations. Multiplet calculations provide multiplet level structures in addition to the spectra, already presented in Fig. **4-9**. For a free atom, one would expect a degenerate ground state with half-integer J_Z values (15/2, 13/2, ..., -15/2). This drastically changes with external influences such as a crystal field or an external magnetic field, e.g. half-integer J_Z values are only conserved for highly symmetric crystal fields. The multiplet level of the surface alloy in an external field of 6.8 T is presented in Fig. **4-10 c** for normal and grazing incidence. It is important to note, that J_Z is the projection of J along the quantisation axis Z , which changes for normal and grazing incidence. The relevant levels are hereby the lowest-lying ones. Excited states could be reached by external stimuli, i.e. phononic or electronic excitations. In our case, the two lowest-lying states are situated at about $J_Z = -4$ for both, normal and grazing incidence. This is in line with our experiments, which also showed a negligible angular dependence of the magnetisation. This changes drastically after the adsorption of graphene. The lowest lying multiplets in Fig. **4-10 d** show a big discrepancy between normal and grazing incidence. In line with our experimental findings, a strong anisotropy appears. Interestingly, the variation of the Gr position has no significant influence on these results, as long as the total charge stays constant. In summary, one could state, that our model system represents our real system very well.

4f charge anisotropy and skyhook effect

As mentioned above, synchrotron-based XANES measurements are not only able to reveal the magnetic properties element-specifically by XMCD, but can also reveal the electronic properties of the probed shell. By evaluating the $M_{4,5}$ edges, we probe the Dy 4f shell. Fig. 4-11 compares the XLD measurements of the surface alloy and the graphene-covered surface alloy. Similar to the magnetic properties presented in Fig. 4-9 a, the XANES does not show any angular dependence in Fig. 4-11 a. This reflects on the XLD signal. For normal incidence, one would not expect any dichroic signal due to geometric reasons. But the out-of-plane component can be addressed by grazing incidence measurements. In the case of the surface alloy, the XLD signal is negligible, which indicates a negligible out-of-plane charge anisotropy. This is in line with the observed magnetic anisotropic behaviour.

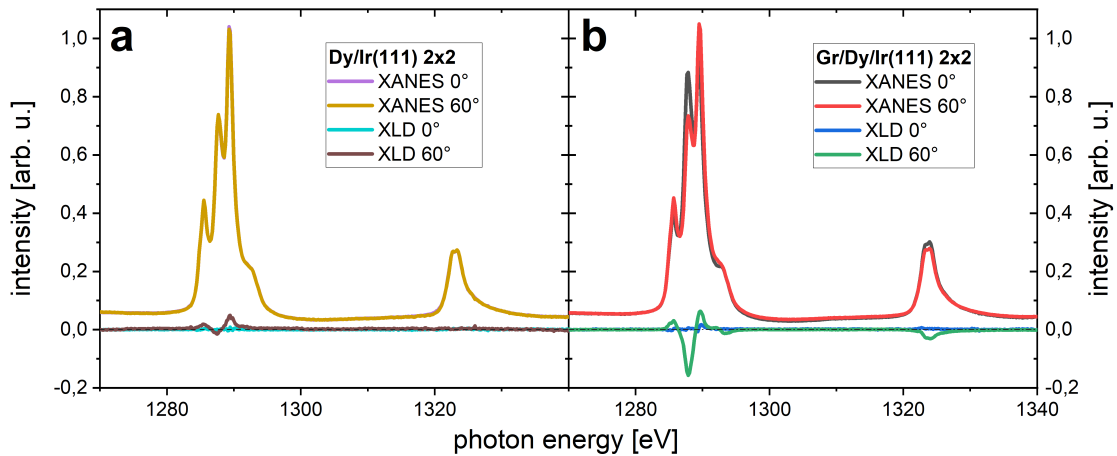


Figure 4-11.: **a** XANES and XLD of the (2x2) Dy surface alloy at 50 mT and 3 K for normal (0°) and grazing (60°) x-ray incidence. **b** XANES and XLD of the graphene-covered(2x2) Dy surface alloy at 50 mT and 3 K for normal (0°) and grazing (60°) x-ray incidence. The XANES spectra are shifted for better visibility. [17]

This changes upon graphene absorption. The difference in the XANES spectra between normal and grazing incidence in Fig. 4-11 b already hints at a strong linear dichroic signal. Again, there is no in-plane XLD signal, whereas a strong XLD signal emerges for grazing incidence. This indicates a strong out-of-plane 4f charge anisotropy. As there is no equivalent to the sum rules for XLD, additional information can only be gained by comparison to theoretical calculations.

One interesting aspect which we want to investigate is the influence of the proposed selective skyhook effect on the spectra. For this purpose, we performed a number of multiplet calculations and compared them with the experimental spectra. In Fig. 4-12 we focus on the M_5 edge of the graphene-covered surface alloy to get a more detailed look.

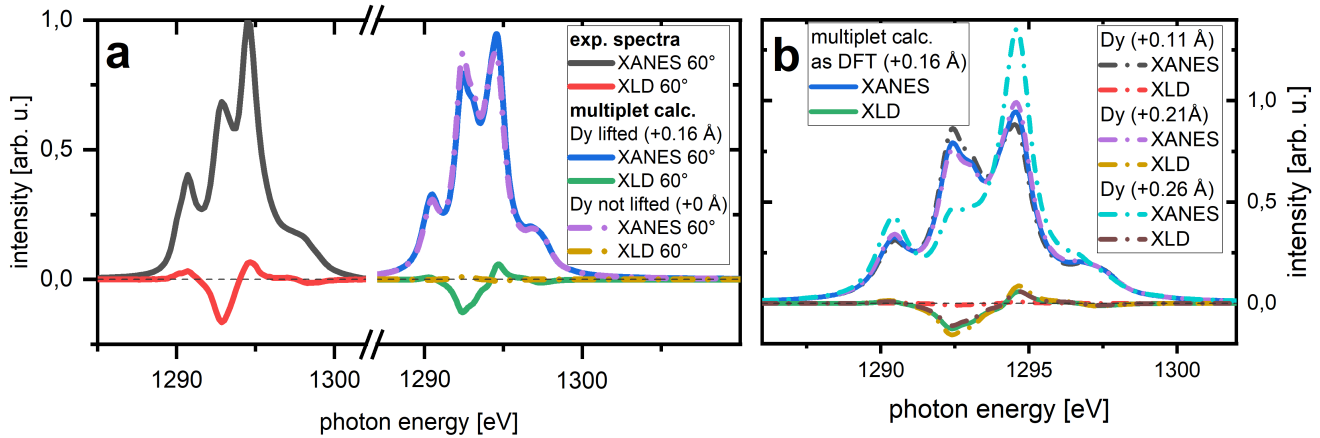


Figure 4-12.: **a** Experimental XANES and XLD spectra of the Dy M_5 -edge of graphene-covered (2x2) Dy surface alloy at 50 mT for grazing x-ray incidence. Multiplet calculations for elevated and non-elevated Dy atoms, in comparison to the (2x2) Dy surface alloy, are displayed next to it. **b** Theoretical XANES and XLD spectra of the structure presented in Fig. 4-10 and for a variation of the Dy z-component by -0.05 \AA , $+0.05 \text{ \AA}$, and $+0.1 \text{ \AA}$. [17]

Fig. 4-12 **a** shows the experimental XANES and XLD spectra of the graphene-covered surface alloy on the left-hand side and two calculated multiplet spectra on the right-hand side. The solid lines represent the multiplet calculation based on the crystal structure presented in Fig. 4-10 **b**. This model, which includes the lifting by the skyhook effect, already displays a very good fit with the XMCD measurements, as shown in Fig. 4-9. For the XLD spectra, we again have a rather good fit. In order to put this into context, calculations based on different crystal fields have been performed. In detail, we varied the elevation of the Dy atom, within the model, which showed a good fit with our experimental results so far. In the case of a non-lifted Dy atom, i.e. at the same elevation above the Ir surface as without Gr, the multiplet calculation shows a negligible XLD signal, as well as a slightly worse fit of the XANES fine structure.

A more detailed analysis of the influence of the Dy lifting on the XANES and XLD spectra is provided in Fig. 4-12 **b**. The spectra present a more precise manipulation of the Dy elevation by 0.05 \AA steps. While a slight reduction of the elevation leads to a negligible XLD signal, similar to the non-lifted spectra in Fig. 4-12 **a**, an elevation by 0.21 \AA displays an even better fit with the experimental data. Increasing the elevation even further leads to a drastic change in the XANES spectrum. Summarizing these results, lifting by the selective skyhook effect by 0.16 \AA up to 0.23 \AA is plausible within our model. This is in line with our DFT results. One has to keep in mind, that the tweezing of the Dy position within this model in the first approximation is only valid for small changes, as the validity is provided by the good fit with the XANES and XMCD experimental spectra and strong theoretical base of the DFT calculations. Major changes in the Dy position would corrupt this model,

but our results proved that they are in line with our interpretation and can therefore be seen as a clear experimental fingerprint of the proposed selective skyhook effect.

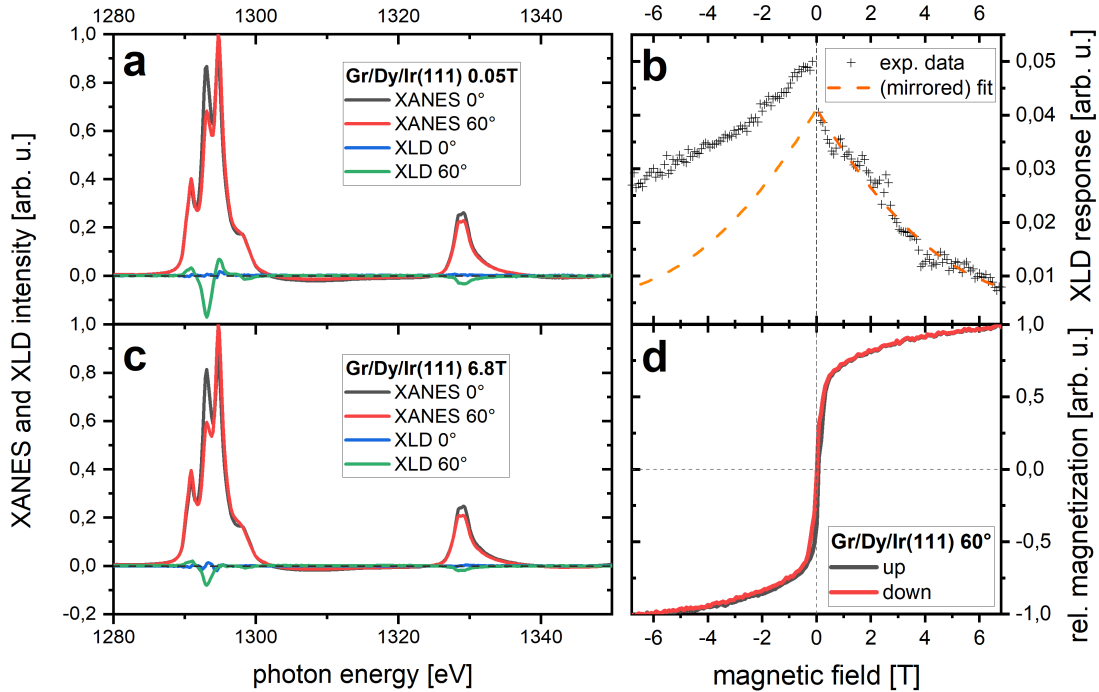


Figure 4-13.: **a** XANES and XLD of the graphene-covered (2x2) Dy surface alloy at zero-field for normal and grazing x-ray incidence. **b** Magnetic field dependence of XLD response of the graphene-covered (2x2) Dy surface alloy for grazing x-ray incidence. **c** XANES and XLD of the graphene-covered (2x2) Dy surface alloy at 6.8 T for normal and grazing x-ray incidence. **d** Magnetic field dependence of XMCD response of the graphene-covered (2x2) Dy surface alloy for grazing x-ray incidence [17]

Fig. 4-13 lays the focus on the magnetic field dependence of the XLD signal of the graphene-covered surface alloy. Fig. 4-13 a displays the XLD spectra already presented in Fig. 4-11 b as a reference. The X-ray magnetic linear dichroic (XMLD) effect can be seen in the comparison of the spectra with the one measured at 6.8 T in Fig. 4-13 c. While there is no significant change in the XANES spectrum, there is a strong decrease of the XLD signal compared to the low-field measurement. A more detailed view of this effect is given in Fig. 4-13 b, which maps the intensity of the feature at 1293 eV for different magnetic fields. Two features appear, that are related to the features of the magnetisation curve, presented in Fig. 4-13 d.

On the one hand, the highest values are present at low fields and the XLD response decays with higher fields. With increasing field, the gradient decreases. This can be correlated with the magnetic field. While at low field, the Dy moments are ordered in-plane and present their

highest out-of-plane electronic anisotropy, increasing external fields force the moments out of the plane and therefore increasing the projected magnetic moment of our measurement, while decreasing the out-of-plane charge anisotropy. One would expect, that such behaviour would not occur if one would measure strictly in-plane, but due to the method used, this is technical impossible. The second and much more puzzling feature is the jump of the XLD signal around zero-field. An explanation for this behaviour could be a ferromagnetic order with a coercive field below our experimental resolution. Switching a ferromagnetic order around zero field would immediately lead to a jump in the XLD signal, while a paramagnetic behaviour would lead to a continuous change. The different absolute values may be explained by the asymmetric measurement of 30° incidence angle, which could lead to an asymmetric XLD response, but to prove this, further investigations would be needed. Nevertheless, a ferromagnetic order with a low coercive field is not only expected by the DFT calculations but could also be detected in several other related systems [62, 64]. Therefore, an investigation of the ferromagnetic properties is very promising. MOKE measurements would be ideal for this system, as they provide in-plane sensitivity, but also synchrotron-based measurements with sensitive electromagnets could provide this information.

Graphene doping

A property of the graphene-covered surface alloy, which only got slightly touched in section 4.2 is the doping of the graphene. The structural investigations and the *ab initio* calculations, which show a Dirac like feature, indicate, that the electronic properties of the graphene are mostly intact and that one could consider the graphene as doped and not as strongly interacting, which would change its properties drastically.

Fig. 4-14 presents XPS measurements of the graphene-covered surface alloy and compares these to Gr/Ir(111). The overview graph in Fig. 4-14 a displays the electron binding energies of the two samples. There are only very few differences between the spectra, mainly the Dy $4d_{3/2,5/2}$ peak, which is only present for the graphene-covered surface alloy. By comparing the Gr/Ir(111) spectrum with literature, we find a very good agreement [158]. The more interesting change is present at the C 1s edge, which is highlighted in Fig. 4-14 b. Here we see a shift of the C 1s peak of the graphene-covered Dy surface alloy to higher energies, compared to Gr/Ir(111). This shift can be related to the Gr doping, as it has been predicted by the DFT calculations. The DFT calculations predict an n-doping of the Gr by -0.75 eV. The XPS measurements allow probing this experimentally. By using the relation by Schröder et al. [47] the shift of the C 1s peak by 0.9 eV relates to a doping level of about -1.1 eV, which is slightly above the expected value. ARPES measurements could provide a more detailed view of the electronic properties of this system. Utilizing spin-polarized ARPES measurements could even add an insight into the magnetic properties of these systems, which would be of great interest.

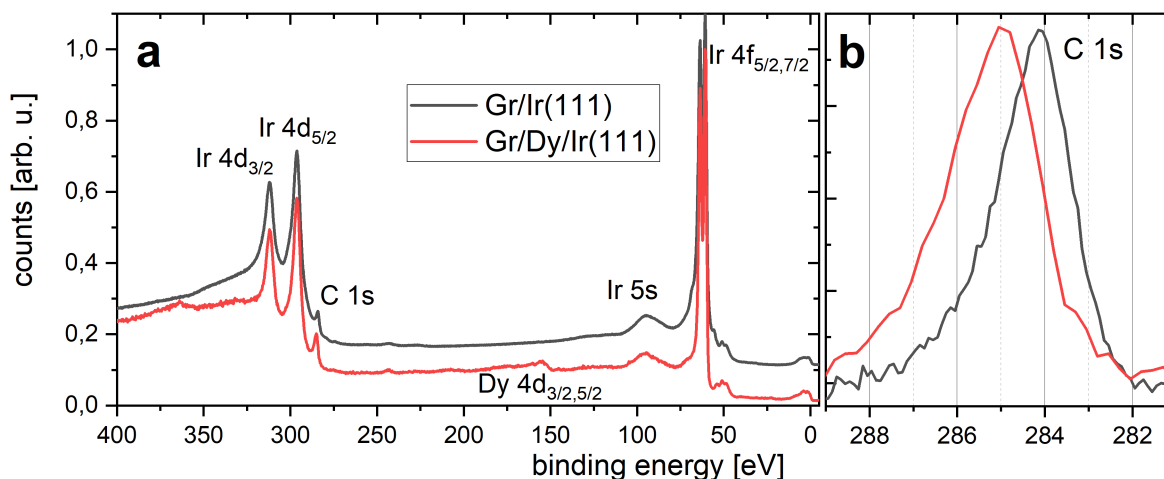


Figure 4-14.: **a** Experimental XPS binding energies for Gr/Ir(111) and the graphene-covered (2x2) Dy surface alloy. The Gr/Ir(111) spectrum is shifted up for better visibility. The peaks are assigned to their respective core levels. **b** Close up on the C 1s XPS spectrum for Gr/Ir(111) and the graphene-covered (2x2) Dy surface alloy. [17]

4.4. Variation of the 4f Metal - a Systematic Study

In this section, we want to extend our investigations on other 4f metals, in order to see if the selective skyhook effect can be treated as a general phenomenon or is limited to the Dy/Ir(111) system. Analogue to the procedure on Dy surface alloys before, we explored the synthesis and the structure of the related systems, compared them to *ab initio* calculations, and probed the electronic and magnetic properties of the 4f surface alloys and the graphene-covered 4f surface alloys.

Synthesis and structure

The synthesis of the 4f surface alloys is similar to the one of Dy/Ir(111) as presented in Fig. 4-1. After the evaporation on a clean substrate, temperatures up to 1480 K are needed for the surface alloy formation. The different results after such synthesis are presented in Fig. 4-15 a-d. For Tb, Dy, and Tm, a clean (2x2) superstructure w.r.t. Ir(111) is visible. The slightly less sharp spots in Fig. 4-15 d are caused by a different measurement setup (regular LEED vs. MCP LEED). For Ho, no (2x2) surface alloy could be realised. A high number of unidentified multi-phase structures are given for lower temperatures, while for higher temperatures, the structure represented in Fig. 4-15 c appears. Spots related to a lattice parameter, which roughly fits the Ho single-crystal parameters, are aligned with the Ir(111) spots. Additional weak slightly misaligned spots are present as well as moiré spots.

The detailed structure of this surface system could not be resolved.

For the graphene-covered surface alloys, the situation changes. The synthesis presented in Fig. 4-1 leads to a graphene-covered (2x2) surface alloy on Ir(111) for all of the probed elements. Fig. 4-15 e-h presents the LEED patterns of the graphene-covered Tb, Dy, Ho, and Tm surface alloy. For Tb, Dy, and Ho lower temperatures lead only to diffuse phases. This is not the case for Tm. Starting from 500 K, Tm intercalates under Gr on Ir(111) and forms a $\sqrt{3} \times \sqrt{3}$ R30° superstructure w.r.t. Gr, as presented in Ref. [73]. Annealing to 1000 K leads to a formation of a (2x2) superstructure w.r.t. Ir(111), which we correlate to the surface alloy formation underneath Gr.

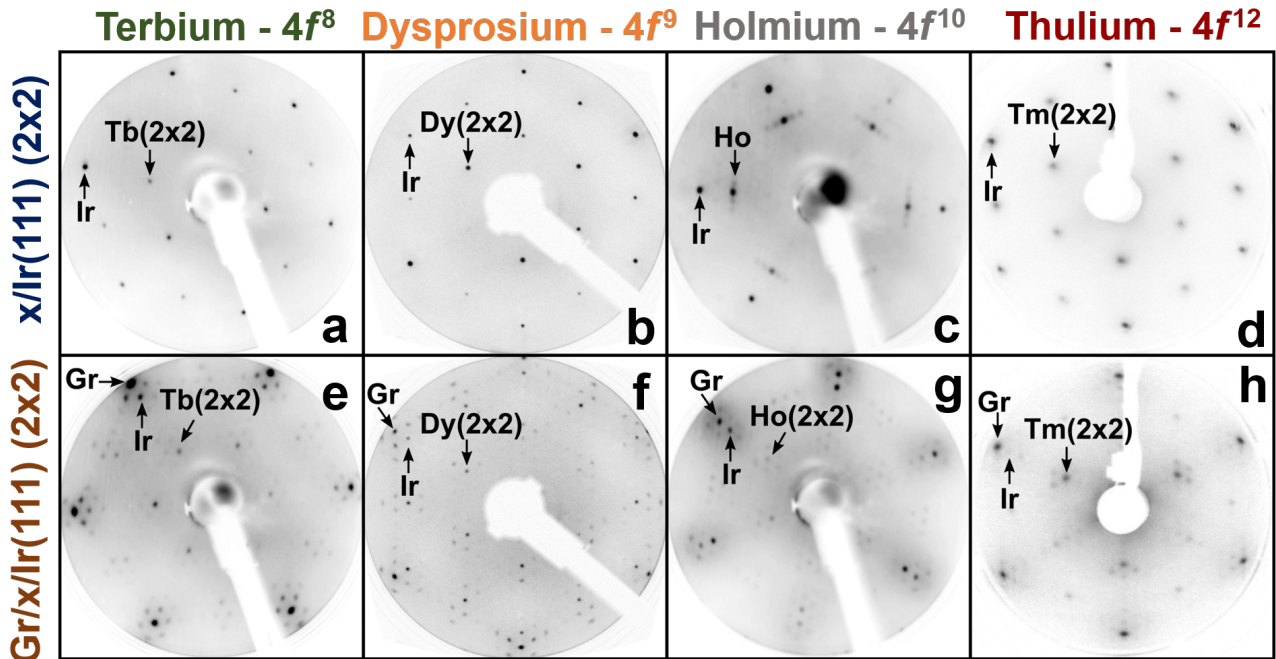


Figure 4-15.: **a-d** Inverted contrast LEED patterns after the deposition and annealing of 0.25 ML_{Ir} Tb **a**, Dy **b**, Ho **c**, and Tm **d** on Ir(111). Tb, Dy, and Tm show a (2x2) superstructure, while Ho orders with respect to the Ir lattice. **e-h** Inverted contrast LEED patterns after the deposition and annealing of 0.25 ML_{Ir} Tb **e**, Dy **f**, Ho **g**, and Tm **h** on Gr/Ir(111). All samples display a (2x2) superstructure and a moiré pattern around every reflex. The primary electron energy is 100 eV for **a-c**, **e**, **f**, 110 eV for **g**, and 70 eV for **d**, **h**. [74]

Opposing to this, our experiments with Eu show that it does not form a surface alloy, but forms intercalation layers as presented in Ref. [45]. We attribute the interstitial behaviour of Tm between the surface alloy formation and the intercalation process to the energy difference between the 2+ and 3+ state, i.e. the energy gain by elevating a 4f electron in the 5d shell. While all the 4f metals in graphene covered surface alloy promote one electron to

the 5d shell, as it provides the metal-metal binding (see section 4.2), Eu does stay in the $4f^7$ state when intercalated, as the half-filled 4f shell is energetically favourable. This is relevant for the integration of 4f metals in organometallic compounds as well, as discussed in section 5.3.

The results of the structural investigation by STM is presented in Fig. 4-16. Fig. 4-16 compares patches of the Dy surface alloy (Fig. 4-16 a) with the ones of the Tm surface alloy in Fig. (4-16 c) and patches of the graphene-covered Dy (Fig. 4-16 b) and Tm (Fig. 4-16 d) surface alloy. The Dy samples have already been discussed in section 4.1.

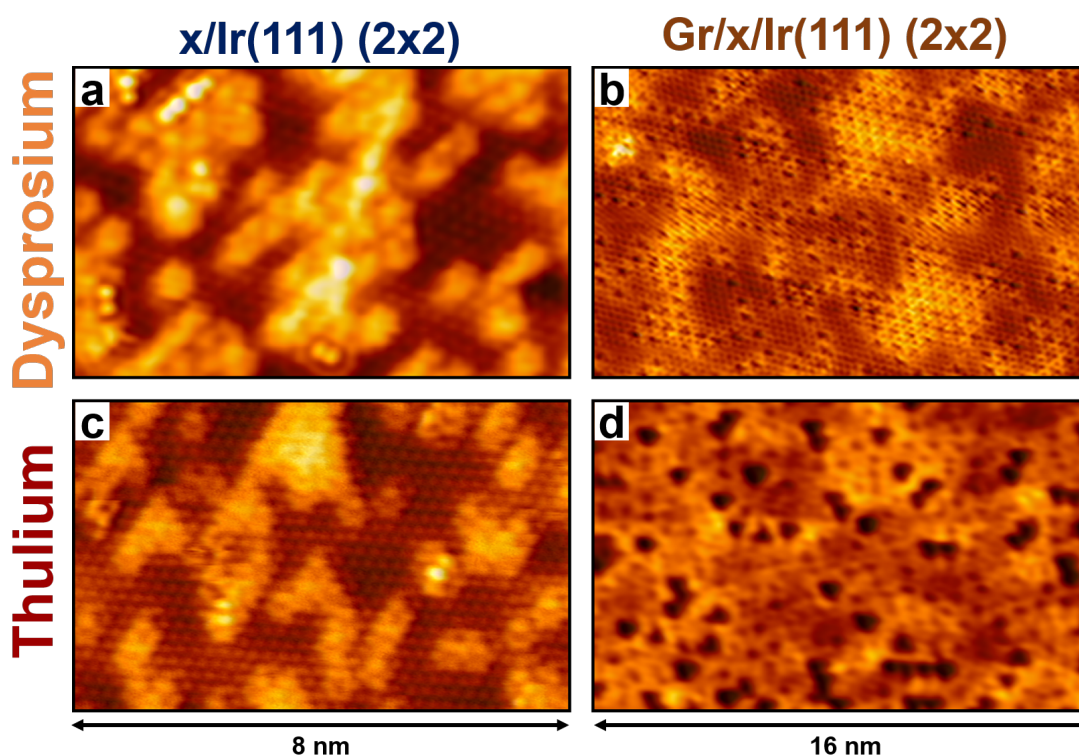


Figure 4-16.: **a, c** Atomic resolution STM topographs of (2x2) Dy **a** / Tm **c** surface alloy patches. **b, d** STM topographs of Dy **a** / Tm **c** surface alloy patches under Gr. Topograph sizes are 8 nm x 5 nm for **a, c** and 16 nm x 10 nm for **b, d**. The tunnelling parameters used are **a** $I = 4.7$ nA, $U = -0.001$ V, **b** $I = 30$ nA, $U = -0.09$ V, **c** $I = 6.2$ nA, $U = -0.001$ V, and **d** $I = 0.4$ nA, $U = -1.58$ V. [74]

Comparing the STM topograph of the Tm surface alloy with the Dy surface alloy, the Tm surface alloy appears sharper, which is correlated to a better tip during the measurement. Concerning the structure, both show the atomic resolution of the Ir(111) with patches of the surface alloy. In both cases, the (2x2) structure can only be hardly recognised on the islands, but the apparent height of the islands indicates a surface alloy formation in both cases. In general, they show a very similar structure. On the first look, the differences are larger for

the graphene-covered surface alloys. The graphene-covered Tm surface alloy in Fig. 4-16 d exhibits a number of dark holes, which we correlate to surface defects, similar to the one presented in Fig. 4-2 b. This could be explained by the reduced annealing temperature compared to the graphene-covered Dy surface alloy. Besides these defects, the structure is very similar. Small black holes correspond to the (2x2) superstructure and larger islands of the superstructure lead to a smaller work function, visible as bright areas. Again, it can be assumed, that the structures of both systems are very similar.

DFT calculations

Similar to the investigation of the Dy surface alloy, we accompanied our structural analysis with *ab initio* calculations. The DFT calculations support our experimental findings. Again, the surface alloy formation and the surface alloy formation underneath Gr are the energetically most favourable states. A small deviation from the Dy surface alloy is the most favoured Gr position in our model. For Tb, Ho, and Tm, the bridge position is the most favourable one. But the energy difference for all systems between bridge and atop is in the meV range, as for the Dy. Also, the occupation numbers are in-line, i.e. in all systems, one *4f* electron is elevated to the *5d* shell. Therefore, no significant structural differences are expected.

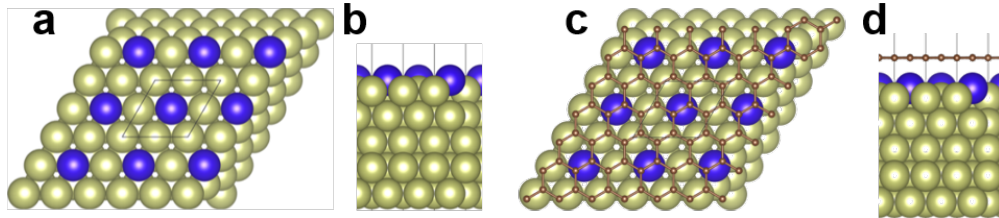


Figure 4-17.: Exemplary top **a**, **c** and side **b**, **d** view of the relaxed DFT structure of a *4f*-surface alloy **a**, **b** and a graphene-covered surface alloy **c**, **d**. [74]

A question arising is the influence of the *4f* species on the selective skyhook effect. As the general structure seems to be similar, one could expect to see the selective lifting also for the other *4f* systems. In fact, our DFT calculations reveal a selective lifting for all of the *4f* elements. The expected elevation above the surface alloy position is given in table 4-1.

4f-element	Tb	Dy	Ho*	Tm
expected lifting	+ 0.23 Å	+ 0.16 Å	+ 0.14 Å	+ 0.13 Å

Table 4-1.: Expected lifting of the *4f* metals out of the surface alloy due to the selective skyhook effect, extracted out of the DFT calculations. The Ho surface alloy could not be realised experimentally.

A general trend is visible. Increasing 4*f* occupancy leads to a decreased lifting due to the selective skyhook effect. This could be closely connected to the single-ion anisotropy of the 4*f* elements, as introduced in section 2.2 and could also have strong indications on the magnetic properties, which will be discussed in the following.

Electronic and magnetic properties

The electronic and magnetic properties of these systems have been probed by XANES and XMCD measurements. Fig. 4-18 presents the experimental XANES and XMCD spectra of 4*f* surface alloys and graphene-covered surface alloys, overlaid with the theoretical multiplet spectra based on the DFT structure. To avoid getting lost with this information, we will go through the different 4*f* metals step by step.

The XANES spectra of the Tb based samples in Fig. 4-18 a, b display a 4*f*⁸ occupation, which indicates that one 4*f* electron is promoted to the 5*d* shell. This will be true for all of the following systems. Concerning the charge anisotropy, a slight difference at around 1240 eV is visible for the different orientations, indicating a slight charge anisotropy. As this measurement has been performed at VEKMAG, which has a bending magnet as photon source, linear dichroic measurements could not be performed. The difference at the peak position is slightly increased for the graphene-covered sample, indicating an increase in the charge anisotropy of the 4*f* shell. The multiplet calculations indicated as dotted lines, reproduce this change in the fine structure qualitatively. Also, the overall fit is rather well, but slightly worse compared to the Dy based samples. Concerning the magnetic properties, the Tb surface alloy displays a magnetic anisotropy favouring in-plane magnetisation. Graphene adsorption increases the difference drastically. As for the Dy based samples, adsorbing graphene favours in-plane magnetisation. The multiplet calculations are in line with the experimental data. They qualitatively show the same trend, but slightly overestimate the magnetic moment.

The Dy spectra, presented in Fig. 4-18 c, d have been discussed in section 4.3.

For Ho, data is only available for the graphene-covered surface alloy, as we were not able to synthesize a (2x2) surface alloy. The XANES spectra in Fig. 4-18 e reveal a 4*f*¹⁰ electron configuration and display some changes between normal and grazing incidence. The slight changes are well represented by the multiplet calculations. The magnetic properties reveal a strong magnetic anisotropy, as we have seen for Tb and Dy. The XMCD reveals a strong magnetic moment in-plane, while the out-of-plane moments are smaller. The ratio between in-plane and out-of-plane projected magnetic moments is reduced compared to Tb and Dy. A comparison to the surface alloy is not possible in this case. The multiplet calculations, which are based on the calculated DFT structure, represent the experimental spectra very well, which indicates, that our approach gives us a proper model also in this case.

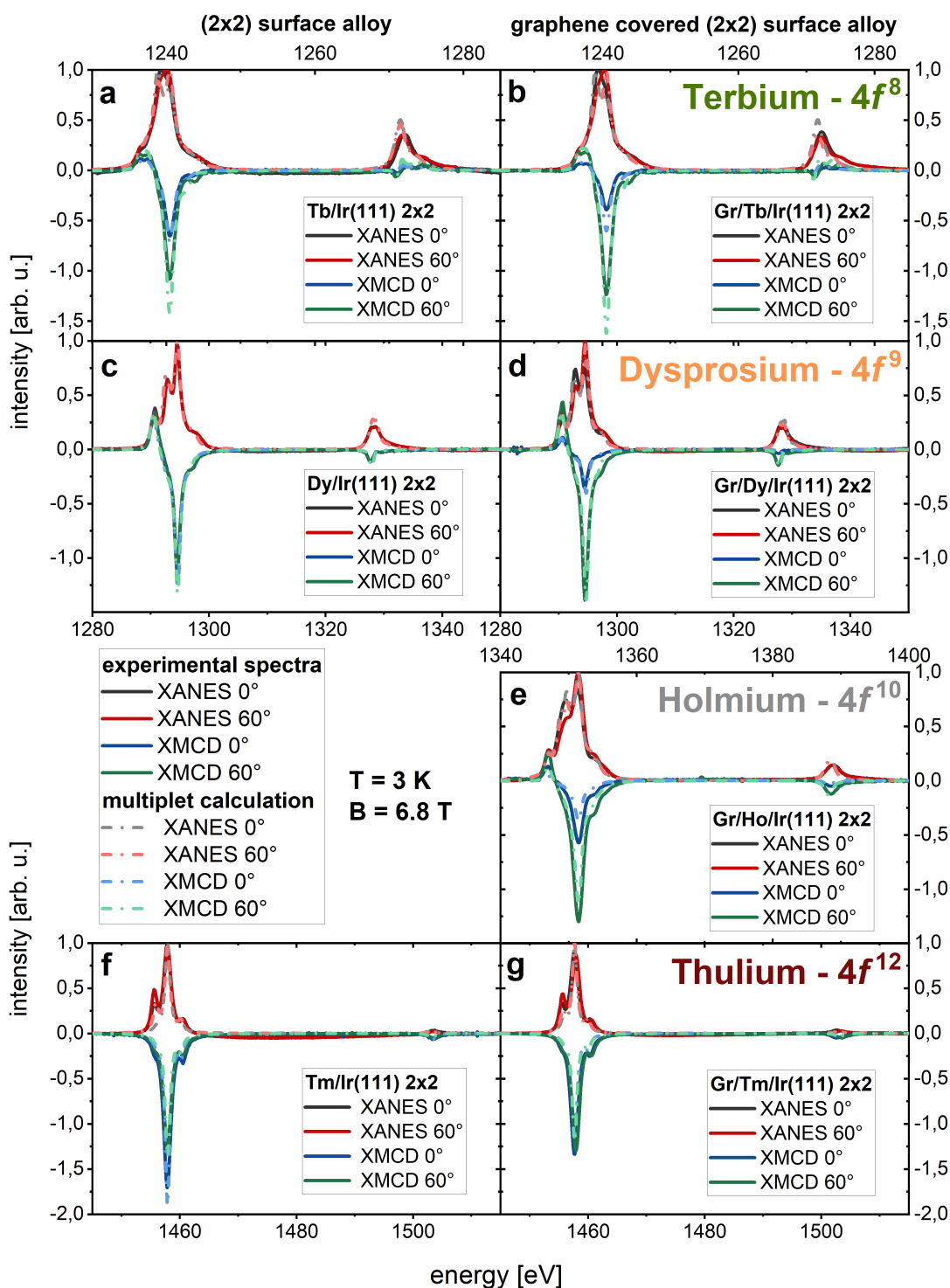


Figure 4-18.: **a-g** Experimental (solid lines) and theoretical (dotted lines) XANES and XMCD of the (2×2) Ir surface alloy with **a** Tb, **b** Dy, and **f** Tm and the graphene-covered (2×2) surface alloy with **b** Tb, **d** Dy, **e** Ho, and **g** Tm for normal (0°) and grazing (60°) x-ray incidence at a temperature of 3 K and a magnetic field of 6.8 T along the beam direction. [74]

The situation changes for Tm, presented in Fig. 4-18 f, g. While the XANES indicates a $4f^{12}$ electron configuration for both systems, the change of the XANES, i.e. the XLD decreases upon Gr adsorption. This is in contrast to the Tb and Dy systems. A similar change can be seen in the XMCD signal. For the surface alloy, an out-of-plane magnetisation is clearly favoured, also in opposition to Tb and Dy. After Gr adsorption, the XMCD signal drastically decreases for the normal incidence measurement, while the grazing incidence XMCD signal slightly increases. This is in line with the findings of the other systems. The multiplet calculations represent the experiment well again, proving our approach.

The different behaviour and easy axis of Tm compared to Tb and Dy could be explained by the single-ion anisotropy [55]. While Tb and Dy surface alloys display an in-plane easy axis with increased anisotropy upon graphene adsorption, the Tm surface alloy shows an out-of-plane easy axis, with a reduced projected out-of-plane moment upon graphene adsorption. This general trend is presented in table 4-2, which displays the experimental sum rule results for the projected reduced spin moment and the projected orbital moment.



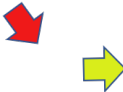
	surface alloy		trend	graphene-covered surface alloy	
	$\mu_S + 6 T_Z$	μ_L		$\mu_S + 6 T_Z$	μ_L
Tb 0°	-1.67 μ_B	-1.01 μ_B		-0.79 μ_B	-0.68 μ_B
Tb 60°	-2.01 μ_B	-1.93 μ_B		-2.67 μ_B	-2.55 μ_B
Dy 0°	-1.82 μ_B	-2.53 μ_B		-0.71 μ_B	-0.82 μ_B
Dy 60°	-1.87 μ_B	-2.51 μ_B		-2.43 μ_B	-3.32 μ_B
Ho 0°	--	--		-0.86 μ_B	-1.09 μ_B
Ho 60°	--	--		-2.17 μ_B	-2.86 μ_B
Tm 0°	-3.19 μ_B	-3.60 μ_B		-2.54 μ_B	-2.86 μ_B
Tm 60°	-2.41 μ_B	-2.66 μ_B		-2.45 μ_B	-2.77 μ_B

Table 4-2.: The projected reduced spin moments $\mu_S + 6T_Z$ and the orbital moments μ_L extracted out of the sum rules of the experimental spectra presented in Fig. 4-18. The change of the projected moment after graphene absorption is indicated by the coloured arrows. [74]

As mentioned before, the measurement method allows only to measure the projected moment of the sample along the beam direction, which is in this case also the direction of the applied magnetic field. In general, an experimental error of 10-15 % can be assumed. The sum rules

can not extract the spin moment directly, as the dipolar term T_Z is not accessible by the measurement method. This will be discussed in more detail below.

The influence of the Gr adsorption is clearly visible if one compares the values of the surface alloys and the graphene covered surface alloys. The general trend is also highlighted by the coloured arrows, red for decreasing values, which includes all normal incidence measurements and green for increasing values, which includes all grazing incidence measurements. One can generally state, Gr adsorption and the selective skyhook effect favours in-plane magnetisation. But this is not the only trend, presented with these values. Also along with the $4f$ occupation number, a change from favoured in-plane magnetisation (Tb) to an out-of-plane magnetisation (Tm) in the surface alloys can be seen. This is in line with recent measurements performed on molecules [61] and to the best of our knowledge has not been reported for surface systems so far.

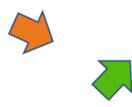
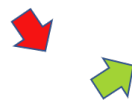

	surface alloy			trend	graphene-covered surface alloy		
	$\langle \mu_s \rangle$	$\langle \mu_l \rangle$	$\langle T_Z \rangle$		$\langle \mu_s \rangle$	$\langle \mu_l \rangle$	$\langle T_Z \rangle$
Tb 0°	-2.04 μ_B	-1.06 μ_B	0.112		-1.80 μ_B	-0.93 μ_B	0.097
Tb 60°	-3.97 μ_B	-2.06 μ_B	0.206		-4.86 μ_B	-2.55 μ_B	0.239
Dy 0°	-2.49 μ_B	-2.63 μ_B	0.076		-0.93 μ_B	-0.94 μ_B	0.038
Dy 60°	-2.37 μ_B	-2.48 μ_B	0.069		-2.70 μ_B	-2.84 μ_B	0.064
Ho 0°	--	--	--		-0.48 μ_B	-0.75 μ_B	-0.015
Ho 60°	--	--	--		-1.57 μ_B	-2.47 μ_B	-0.051
Tm 0°	-1.59 μ_B	-4.01 μ_B	-0.353		-1.00 μ_B	-2.52 μ_B	-0.194
Tm 60°	-0.88 μ_B	-2.22 μ_B	-0.221		-0.89 μ_B	-2.20 μ_B	-0.195

Table 4-3.: The expectation values of the projected spin moment μ_S , the orbital moment μ_L , and the quadrupolar term T_Z extracted out of the multiplet calculations presented in Fig. 4-18. The change of the projected moment after graphene absorption is indicated by the coloured arrows. [74]

Additional insight into the magnetic properties and the changes within the $4f$ series is provided by our multiplet calculations. As presented in Fig. 4-18, the multiplet spectra show a very good overall fit with our experimental spectra, which indicates that the models based on DFT calculations represent the real systems rather good and therefore it is justified to use their values for our interpretation.

In difference to the experimental sum rules, the multiplet calculations allow a separation of the spin moment, orbital moment, and the dipolar term T_Z , as presented in table 4-3. To be precise, the given values are the respective expectation values. The general trend of graphene adsorption is also valid within our multiplet approach. More interesting is the change based on the different 4f occupations, especially concerning the T_Z term. The T_Z term changes from positive values for Tb and Dy to negative values for Ho and Tm. Although such a trend is expected from early multiplet calculations [129], one could learn something about the effect of the single-ion anisotropy, as is it closely correlated [55]. The oblate shape of Tb and Dy leads to a positive T_Z value, while the prolate shape of the Tm leads to a highly negative T_Z value, which contributes strongly to the spin moment. This has to be taken into account when discussing Tm XMCD spectra.

Another question arising is the influence of the different 4f metals on the electronic properties of the Gr. The DFT calculations suggest different lifting heights for the different 4f elements due to the selective skyhook effect. The reduced interaction could affect the doping level for example. Also, could a variation of the doping level limit the possibilities of specifically manipulating the magnetic properties of an adsorbed system by making use of the different favoured magnetisation directions of the graphene-covered 4f surface alloys.

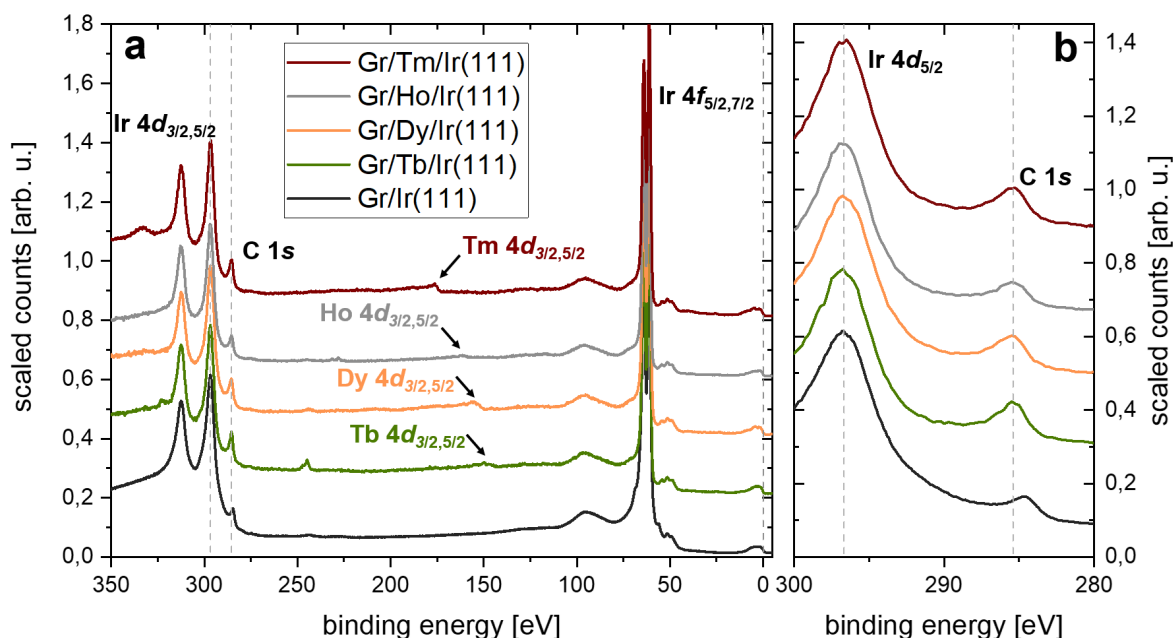


Figure 4-19.: **a** Low energy XPS spectra of the graphene covered surface alloys and Gr/Ir(111). Several peaks are indicated and dotted lines are given as a guide to the eye. **b** Zoom-in on the C 1s and Ir $4d_{5/2}$ peak. The dotted lines indicate the constant position of the Ir $4d_{5/2}$ peak and the shift of the C 1s peaks of the graphene-covered surface alloys with respect to Gr/Ir(111). [74]

The answer to these questions is provided in Fig. 4-19. It presents XPS spectra of all the graphene-covered surface alloys presented above and compares them to clean Gr/Ir(111). One difference between all the spectra are the highlighted $4d$ peaks of the $4f$ elements. They shift slightly for the different graphene-covered surface alloys and are absent in the clean Gr/Ir(111) sample. Although the $3d$ peaks would be far more dominant and would provide clearer information about e.g. the oxidation state, we are limited due to our setup with an Al K_α source. Eu and Tb $3d$ edges can be nicely resolved, but starting from Dy, the peaks are in the rise of the elastic peak, while Ho and Tm cannot be measured anymore. But concerning the Gr doping, the C $1s$ peak is the relevant one, which is highlighted in Fig. 4-19 b. Indicated by the dotted lines, we see a shift at the C $1s$ peak, while the Ir $4d_{5/2}$ sits at the same position. Similar to the results in section 4.3, the Gr is n-doped for all the graphene-covered surface alloys. A shift of about 0.9 eV of the C $1s$ peak is present for all the samples, which can be translated to a doping level of -1.1 eV by using the relation by Schröder et al. [159]. The similar doping level indicates, that the interaction and therefore the charge transfer of the $4f$ atoms with the C atoms of the Gr is similar for all the different species. Therefore one could expect, that the graphene-covered surface alloys display similar electronic properties as a substrate, while only the magnetic properties are dependent on the $4f$ element used.

4.5. Conclusion and Outlook

In this chapter, we introduced the synthesis of new surface systems, namely the $4f$ surface alloys and the graphene-covered $4f$ surface alloys, and investigated their growth and their structure by LEED and STM. Complimentary *ab initio* calculations provided the theoretical background and supported our experimental findings. The effect of the proposed selective skyhook effect on the electronic and magnetic properties could be revealed by element-specific synchrotron-based measurements and could be reproduced by our combined theoretical multiplet approach. The variation of the $4f$ elements allowed us to generalize this effect and revealed systematic changes within the $4f$ series as well as upon graphene adsorption, which finally provided us with a set of electronically and structural similar substrates with tuneable magnetic properties based on the choice of the $4f$ species.

Our investigations showed, that $4f$ metals form surface alloys on Ir(111) after annealing to 1480 K. These (2×2) surface alloys differ from the $(\sqrt{3} \times \sqrt{3})$ R30° rare-earth surface alloys on transition metal surfaces reported so far [66, 62, 68, 71]. Analogue to this synthesis, such surface alloy forms underneath Gr as well, leading to so-called graphene-covered surface alloys. These differ from $4f$ intercalation layers underneath Gr [44, 45, 160] by their incorporation of the $4f$ atoms into the Ir surface. The Gr structure and even the moiré structure stay intact, indicating that the Gr properties are still intact and that the Gr layer could act as a passivation layer that allows to utilize the $4f$ magnetic properties outside of the UHV.

DFT calculations supported our findings and proved, that the incorporation of the $4f$ atoms into the surface is energetically more favourable than adsorption. It also suggests $5d4f$ hybrid states at the $4f$ elements, enabled by the interaction with the surrounding Ir atoms and the resulting crystal field. This statement also holds for the graphene-covered surface alloys. The calculations propose, that the $4f$ atoms are particularly lifted, while the Ir atoms are not affected by the Gr adsorption. This selective skyhook effect is mediated by the $5d4f$ hybrid states, which hybridise with the p_z like orbitals of the Gr and therefore lift e.g. Dy 0.16 Å out of the surface alloy. This lifting is accompanied by a massive increase in the ferromagnetic coupling constant, which has so far only been proposed theoretically for $3d$ metal surfaces [151, 153, 154, 161].

The large proposed changes in the structure, as well as the electronic and magnetic properties, have been probed by XANES, XMCD, and XLD. A massive increase of electronic and magnetic anisotropy could be detected upon Gr adsorption. While the Dy surface alloy displays a rather isotropic behaviour, the graphene-covered surface alloy strongly favours in-plane magnetisation, which is accompanied by a charge anisotropy of the $4f$ shell. Our ligand field multiplet approach based on the atomic positions of the DFT calculation could reproduce these results nicely, providing us with a proper model system. Based on this model system, we were able to extract the lifting of the $4f$ metal out of our XLD measurements. The experimental value was slightly above the theoretical one, but fits the DFT results within the experimental error, proving the selective lifting of the $4f$ metal. The proposed ferromagnetic coupling could not be measured directly. Due to the negligible in-plane anisotropy, coercive fields of a few mT are expected, as reported for similar systems [62, 64]. This was far below our experimental error. Besides a few features in our data, which hint at the ferromagnetic coupling for the graphene-covered sample further measurements need to be done, to reveal this property. MOKE measurement would fit this system perfectly, especially as they are sensitive to in-plane magnetisation, but also XMCD measurements with precise electromagnets would allow revealing this property. The ferromagnetic order could be of special interest, if one uses this system as a substrate, e.g. for spintronic application.

By introducing further $4f$ elements into this system, a systematic study could be performed. By comparing the synthesis, structure, electronic, and magnetic properties of surface alloys and graphene-covered surface alloys based on Tb, Dy, Ho, and Tm, general trends could be revealed. The synthesis and structural analysis indicated, that the different $4f$ species behave quite similar, and similar structures form, which allows a direct comparison. The DFT calculations proposed a reduction of the lifting due to the selective skyhook effect for increased $4f$ occupation, which does not influence the general trend of a decreased out-of-plane projected moment and increased in-plane projected moment upon Gr adsorption. Another trend based on the $4f$ occupation showed up during the magnetisation measurements. While Tb favours in-plane magnetisation in the surface alloy, Tm shows an out-of-plane easy axis. This change is also represented in the electronic anisotropy. While Gr adsorption increases the anisotropy of the $4f$ shell for Dy, it decreases the XLD signal for Tm. This is closely

related to the single-ion anisotropy [55, 61] but has not been reported for surface systems so far. Our combined theoretical multiplet approach could represent all of the experimental spectra fairly well, verifying our approach. They also highlight the importance and the influence of the dipolar term T_Z , that we provided for the whole sample set.

XPS measurements of graphene-covered surface alloys revealed an n-doping of the Gr, which does not depend on the $4f$ species used. Combined with the finding, that the structural properties of Gr are still intact, these systems could be an ideal substrate for any kind of nano-sized spintronic applications, as the magnetic properties of the substrate are tunable by the choice of the $4f$ species. Interactions with a magnetic substrate have shown to be a versatile tool to manipulate the properties of adsorbed systems [13, 14, 162]. This lays the ground for future experiments, in which one can make use of the tunable magnetic anisotropy of the substrate and the interaction with adsorbed nanosized devices. The first preliminary experiments are presented in section 5.2.

5. Nanowires and Organometallic Compounds

The work presented in this chapter consists of data and measurements partly published as S. Kraus, **A. Herman**, F. Huttmann, M. Bianchi, R. Stan, A. Holt, S. Tsukamoto, J. Dreiser, K. Bischof, H. Wende, P. Hofmann, N. Atodiresei, and T. Michely. Uniaxially aligned 1D sandwich-molecular wires: electronic structure and magnetism [163] and S. Kraus, **A. Herman**, F. Huttmann, C. Krämer, S. Tsukamoto, H. Wende, N. Atodiresei, and T. Michely. Selecting the Reaction Path in On-Surface Synthesis Through the Electron Chemical Potential in Graphene [164]. For clarity, figures taken out of these papers are tagged as "adapted from" or "provided for" in the following. A complete list of all beamtimes and the contributors is given in Appendix B.

In this chapter, we will focus on the element-specific investigation of the electronic and magnetic properties of $4f$ -elements in organometallic compounds. In order to put these measurements into context, a brief introduction to the synthesis and the structure is given. In section 5.1 we will describe EuCot nanowires on Gr/Ir(110), in 5.2 the influence of the substrate and the ligands will be investigated, and in 5.3 we will focus on thulium-based compounds.

5.1. EuCot Nanowires on Gr/Ir(110)

As introduced in section 2.4, EuCot nanowires are of great interest and order ferromagnetically at low temperatures. A limitation of EuCot nanowires on Gr/Ir(111) is the random orientation of the wires on the substrate. In order to orient the nanowires on a compatible substrate, the synthesis of Gr/Ir(110) was developed [37]. A more detailed description of this substrate, as well as the synthesis, is provided in Appendix A.1.

Fig. 5-1 presents a structural investigation of EuCot nanowires on Gr/Ir(110). The STM topograph in Fig. 5-1 a displays an overview image of globally-ordered nanowires along [001]. The Gr/Ir(110) appears dark as the contrast is focused on the nanowire islands. The vast majority of the wires are well oriented, only a few differently oriented domains are observed, preferably at step edges. The LEED pattern in Fig. 5-1 b also supports the global orientation. The relevant reflections and the unit cell are highlighted.

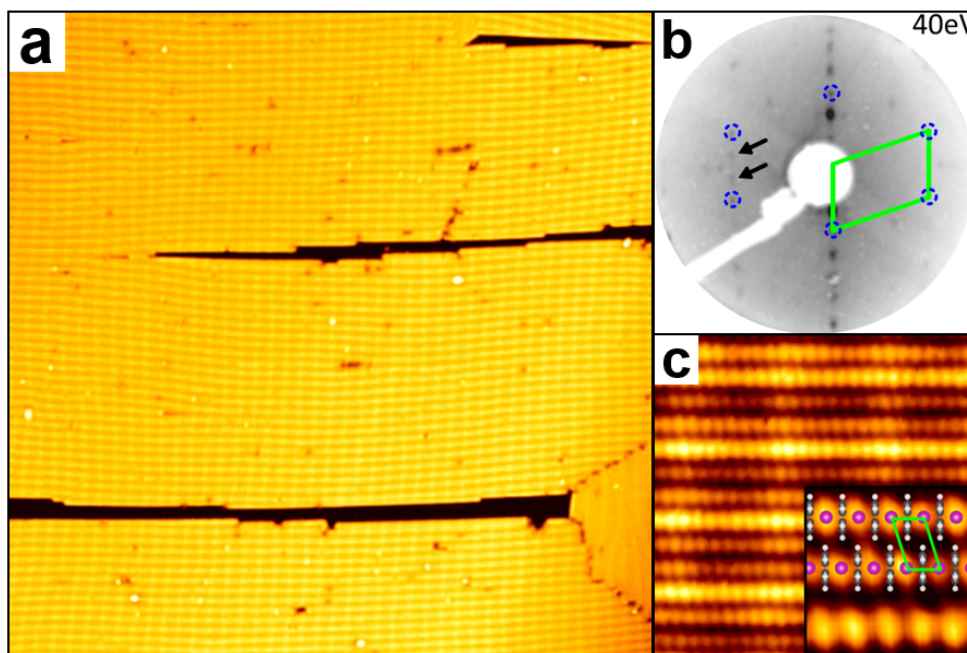


Figure 5-1.: **a** STM topograph of a full layer of EuCot nanowires on Gr/Ir(110) ($150 \text{ nm} \times 150 \text{ nm}$). **b** Contrast-inverted LEED pattern of the sample presented in **a** at 40 eV primary electron energy. The unit cell of the EuCot nanowires is indicated by the green lines, with the first order reflexes encircled. The arrows indicate the (3×1) superstructure. **c** STM topograph of EuCot/Gr/Ir(110) showing the (3×1) intensity variation represented in **b**. The inset displays a molecular resolution STM topograph with a ball model and the unit cell of the nanowires indicated ($2.5 \text{ nm} \times 2.5 \text{ nm}$). Adapted from [163].

The unit cell is also indicated in the real space STM topograph presented in Fig. 5-1 **c**. In this close-up, the molecular resolution points out the interlocking of the nanowire carpet, as also visible in the inset. By synthesizing these well-oriented wires, one can hope to increase T_C as well as the coercivity field of the system, compared to the random oriented nanowire islands on Gr/Ir(111), as one expect the magnetic order along the wire. It also enables directional dependent measurements like ARPES, which allows one to reveal the band structure of these sandwich-molecular nanowires.

In order to probe the magnetic properties of this new system, XANES and XMCD measurements have been conducted at the X-Treme beamline at the SLS. Fig. 5-2 **a** displays the XANES spectra of the $M_{4,5}$ edge of Eu for normal and grazing incidence. The XANES shows a clear $4f^7$ electron configuration [138]. By directly comparing the two spectra we see only neglectable variations, indicating negligible linear dichroism. This is expected for a $4f^7$ electron configuration as it represents a half-filled $4f$ -shell. The red line represents the integral over the XANES spectrum, which will be used in the evaluation of the sum rules.

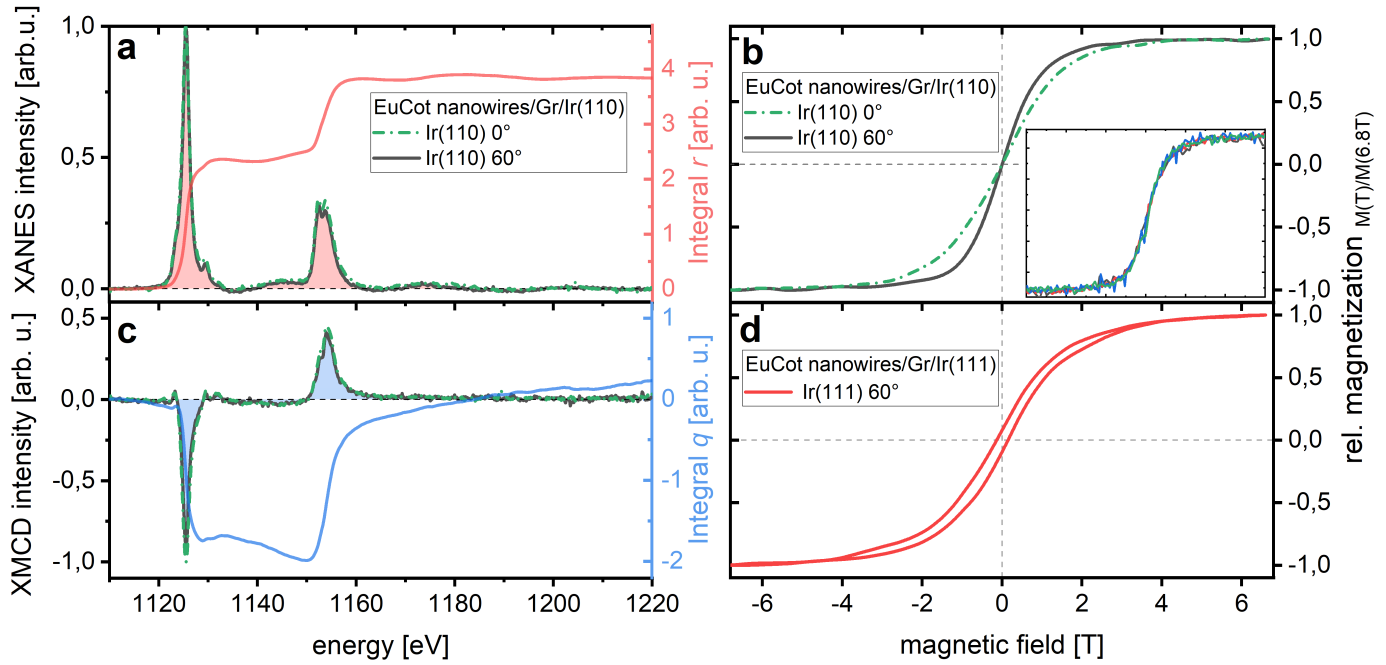


Figure 5-2.: **a** XANES of EuCot nanowires on Gr/Ir(110) for normal (0°) and grazing incidence (60°) at a temperature of 3 K and a magnetic field of 6.8 T. The red line represents the integral r for grazing incidence utilized for the sum rules. **b** Respective magnetisation curves at 3 K for normal (0°) and grazing (60°) incidence normalised to the magnetisation at 6.8 T. The inset displays the raw data for grazing incidence consisting of up and down measurements, clearly showing no opening of a hysteresis loop. **c** Respective XMCD spectra with the sum-rule integral q . **d** Magnetisation curve of EuCot/Gr/Ir(111) at 3 K for grazing (60°) incidence normalised to the magnetisation at 6.8 T. Provided for [163].

Fig. 5-2 c shows the XMCD spectra for grazing and normal incidence. Similar to the XANES spectra, no anisotropy is present at a magnetic field of 6.8 T, which can be explained by the fact, that the Eu is saturated at this field. The evaluation of the sum rules, which lead to a spin moment $\mu_S = (7.2 \pm 0.6)\mu_B$ and an orbital moment $\mu_L = (0.0 \pm 0.4)\mu_B$ for grazing incidence, supports the idea of full saturation. For normal incidence, the evaluation lead to $\mu_S = (7.0 \pm 0.8)\mu_B$ and $\mu_L = (0.1 \pm 0.4)\mu_B$. The dipolar term $\langle T_Z \rangle$ is hereby approximated by zero, as the dipolar term of a half-filled $4f$ -shell is negligible [165]. The magnetisation curves presented in Fig. 5-2 b correspond to the maximum of the XMCD signal. The curves for the field sweeping up and down are averaged for better visibility. The raw data for grazing incidence is given in the inset. In the range of the error, there is no opening of a hysteresis loop at a temperature of 3 K, differing from the magnetisation curve of EuCot nanowires on Gr/Ir(111) shown in Fig. 5-2 d. There is also a difference in susceptibility between normal and grazing incidence. The susceptibility of 60° is hereby larger by a factor of 1.6

compared to 0° , stating that the easy axis of the magnetisation lays along the wire direction, i.e. [001]. We will have a closer look at this topic below. It is important to mention, that the magnetisation curve shown in Fig. 5-2 d confirmed the finding in Ref. [18]. We contribute the slightly higher coercive field and the opening of the hysteresis at higher fields to the lower measurement temperature.

A closer look at the magnetic properties of the wires and the different susceptibilities is provided in Fig. 5-3. Two questions arise from the missing hysteresis of EuCot nanowires on Gr/Ir(110), which we want to answer by investigating two different samples. Is the direct interaction with the substrate quenching the magnetism? And may it be possible that the magnetic order lies in-plane perpendicular to the wire axis? We synthesised a multilayer EuCot/Gr/Ir(110) sample, for which is known, that the wires are still well oriented [149] and we measured a EuCot/Gr/Ir(110) monolayer sample along the [010] direction.

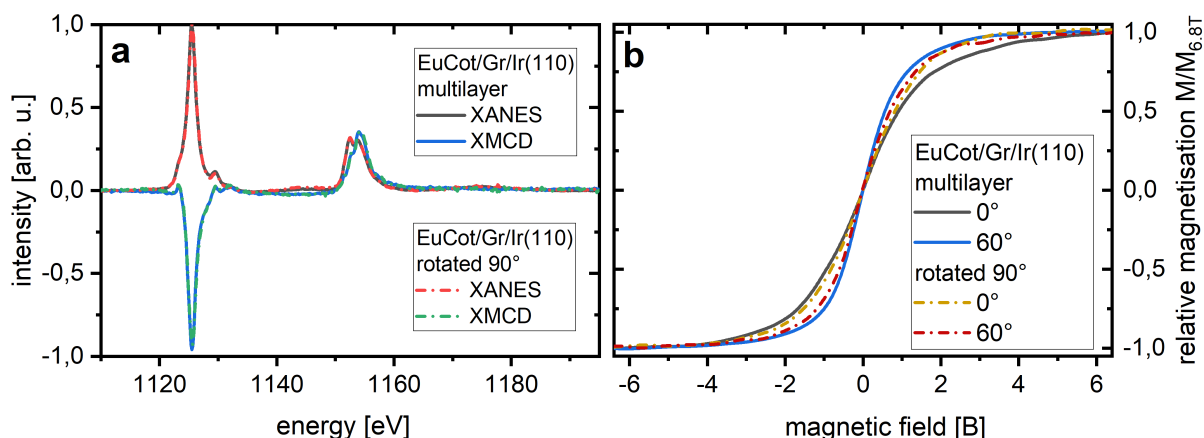


Figure 5-3.: **a** XANES and XMCD of EuCot nanowire multilayer on Gr/Ir(110) and EuCot nanowires measured perpendicular to the dominant wire axis (rotated 90°) for grazing incidence at a temperature of 3 K and a magnetic field of 6.8 T. **b** Respective magnetisation curves at 3 K for normal (0°) and grazing (60°) incidence normalised to the magnetisation at 6.8 T.

The XANES and XMCD spectra presented in Fig. 5-3 a are similar to the ones presented in Fig. 5-2, indicating that there are neither changes in the electronic properties, nor in the saturation magnetisation. More interesting are the magnetisation curves displayed in Fig. 5-3 b. Again there is no opening of a hysteresis loop for both samples. In the case of the multilayer, this means, that the nanowires still do not show a ferromagnetic behaviour in the upper layers, leading to the question, if the intra-wire interaction is the reason for this suppression of the ferromagnetism, or if the interaction with the Gr/Ir(111) itself leads to the ferromagnetic ordering. Another possible explanation could be the increased quantum magnetic tunneling due to the changed electronic properties, which would lead to a fast decay time of the magnetic order [166]. While Gr/Ir(111) has proved to strongly decouple adsorbed

systems from electronic and phononic interactions with the substrate (comp. section 2.4), Gr/Ir(110) may not provide such strong decoupling. This could lead to a decay of the global ferromagnetic order within a time scale which is below the one of our measurement. For the rotated sample, we can state, that the wires also do not show a magnetic ordering perpendicular to the wires. Focussing on the susceptibility, the multilayer sample displays similar behaviour to the monolayer, indicating that this magnetic anisotropy arises only due to the orientation of the nanowires, rather than the interaction with the surface. For the rotated monolayer, the susceptibility is only slightly higher for grazing incidence. For an ideal sample, one would expect to have no variation for rotation around the wire axis, but due to defects at step edges, which leads to wire orientations along $[010]$, the slight increase for grazing incidence measurements can be explained.

Electronic properties

In order to reveal further electronic properties, ARPES and XPS measurements have been performed. Of special interest are the $4f$ bands of the EuCot nanowires. Theoretical DFT calculations presented in Fig. 5-4 **a** predict dispersion along the wire direction ($\Gamma - N$). If experiments could approve this prediction, it would be the first confirmation of dispersion of bands in 1D organometallic compounds. In Fig. 5-4 **b**, the experimental ARPES spectra of EuCot nanowires on Gr/Ir(110) are presented. One broad dominant flat band is visible at -1.85 eV with a full width at half-maximum of (1.0 ± 0.2) eV. No dispersion could be detected. One big problem of these measurements is radiation damage. The STM topograph in Fig. 5-4 **c** displays the partly destroyed nanowires after scanning the sample for the measurement shown in Fig. 5-4 **b**, which already significantly reduced the amount of photons per area. X-ray induced oxidation of $4f$ metals is also discussed in detail in Appendix A.2.

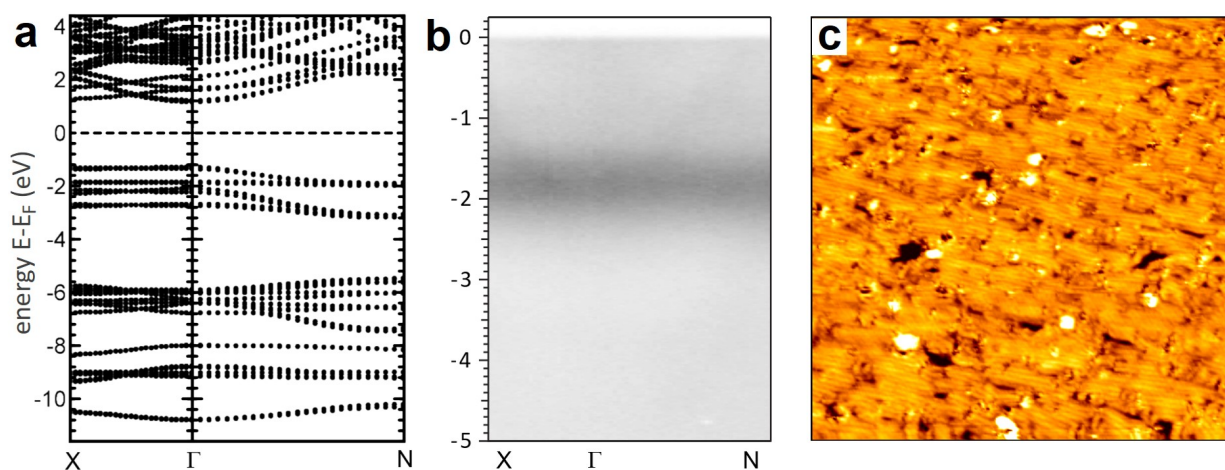


Figure 5-4.: **a** DFT band structure of 1 ML of EuCot nanowires along $X - \Gamma - N$ using an effective Hubbard U of 3.5 eV. **b** Angle-resolved photo emission spectrum along $X - \Gamma - N$ for 1 ML of EuCot nanowires on Gr/Ir(110) at a photon energy of 110 eV while scanning the sample. **c** Respective STM topograph after scanning the sample to limit the photon dose to $\approx 6 \cdot 10^3 \frac{ph}{nm^2}$ ($150 \text{ nm} \times 150 \text{ nm}$). Adapted from [163].

Although radiation damage is detected, a vast majority of the wires is still intact, just with reduced lengths. The flat band can be attributed to the $4f$ atoms of the Eu. The angle-integrated ARPES spectrum in Fig. 5-5 **a** shows a maximum at the flat band position. By comparing this to the spin-polarized projected density of states of the EuCot nanowires presented in Fig. 5-5 **b** we see a good agreement. The comparison of the experimental data with the DFT calculations also allows extracting the effective Hubbard U that should be used for DFT calculations of organometallic europium compounds. The best fit is given for an effective Hubbard U of 3.5 eV.

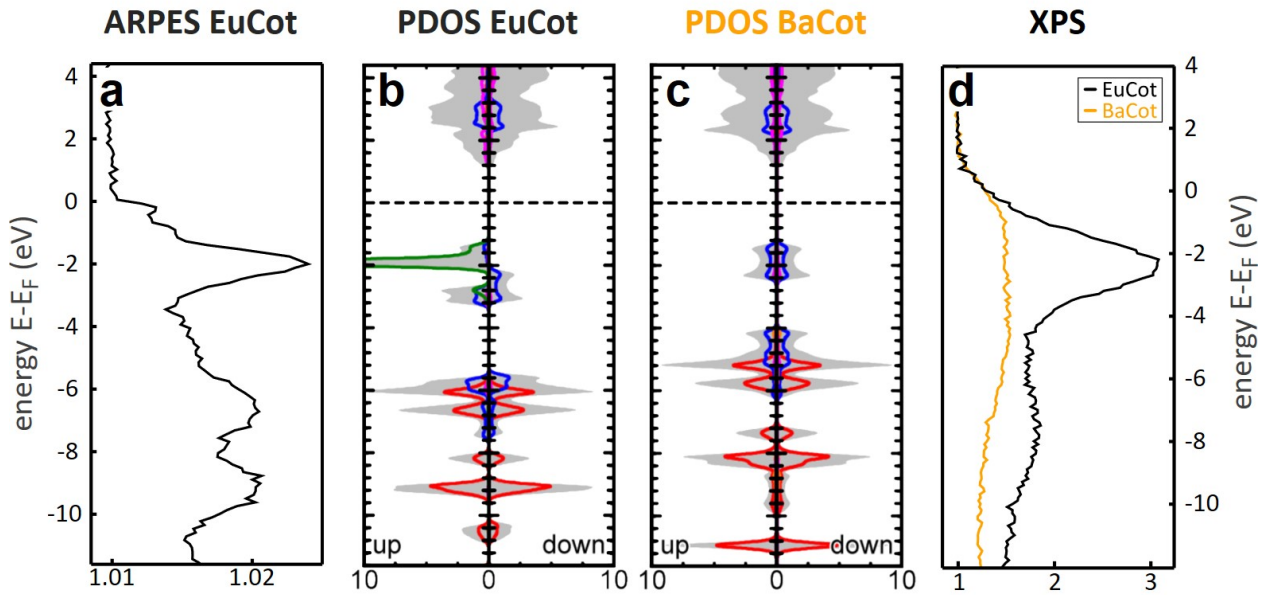


Figure 5-5.: **a** Angle-integrated ARPES spectrum of 4 ML EuCot nanowires on Gr/Ir(110). **b**, **c** Calculated spin-polarized PDOS for 1 ML of **b** EuCot and **c** BaCot nanowires using an effective Hubbard U of 3.5 eV. **d** XPS spectra of ≈ 10 ML of EuCot and BaCot nanowires on Gr/Ir(110). **a-c** adapted, **d** provided for [163].

To prove experimentally that the origin of the flat band are the $4f$ electrons of the Eu, we compared them to BaCot nanowires on Gr/Ir(110). BaCot nanowires have a similar structure to the EuCot nanowires, but in variation to Eu, Ba has no $4f$ electrons. The projected density of states of BaCot nanowires presented in Fig. 5-5 **c** implies, that no peak would be expected at around -2 eV. The XPS measurements we performed on EuCot and BaCot nanowires on Gr/Ir(110) demonstrate that this contribution correlates to the $4f$ electrons. The difference is clearly visible in the low energy XPS spectra in Fig. 5-5 **d**. While there is a distinct peak in the XPS spectra of the EuCot nanowires on Gr/Ir(110) at -2 eV, similar to angle-integrated ARPES data, BaCot nanowires have a rather flat curve at low energies.

5.2. Variation of Substrate and Ligand for EuCot Nanowires

As described in section 5.1, changing the substrate and templating a global orientation can have significant influence on the magnetic properties of EuCot nanowires. In this section, we will present different approaches to manipulate the magnetic properties of the EuCot nanowires, from chemical doping and global orientation to magnetically anisotropic substrates and the variation of the organic ligands.

Variation of the substrate

As mentioned above, the variation of the substrate is one opportunity to manipulate the magnetic properties of EuCot nanowires. By doping Gr, the electronic potential can be shifted, which directly influences the nanowire properties. For Gr/Ir(111) Eu doping has been intensively studied and leads to an n -doping of -1.4 eV [45]. But due to our element-specific approach, additional Eu in the system would distort our measurement. Therefore a different approach is used, namely Yb-intercalation. The synthesis of Yb-doped Gr/Ir(111) works similar to Eu intercalation [149].

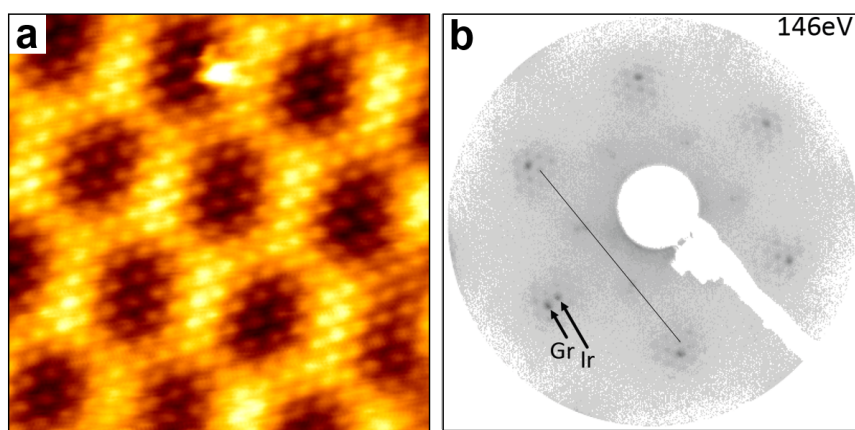


Figure 5-6.: **a** STM topograph of the moiré of Gr with Ir(111) and the $(\sqrt{3} \times \sqrt{3})R30^\circ$ intercalated Yb lattice ($15 \text{ nm} \times 15 \text{ nm}$). **b** Contrast-inverted LEED pattern corresponding to **a** at 146 eV primary electron energy. Indicated are Gr, Ir, and the $(\sqrt{3} \times \sqrt{3})R30^\circ$ superstructure by the guide to the eye. Both adapted from [149].

Fig. 5-6 **a** shows an STM topograph of Yb-intercalated Gr/Ir(111). In combination with the LEED representation provided in Fig. 5-6 **b**, one can state, that Yb-intercalated Gr/Ir(111) is a well-ordered template for nanowire growth. The doping level of the graphene has not been measured but could be roughly estimated by the comparison to Eu-intercalation, which has a similar intercalation process, differing from the graphene-covered surface alloys presented in chapter 4. Negative doping of the Gr in the same order can be expected.

Another intriguing template that allows global orientation of EuCot nanowires with smaller impact on the electronic structure is Gr/Ir(332) [167]. While a bare Ir(332) surface consist of small regular terraces along the $[\bar{1}10]$ direction, the situation changes upon Gr adsorption. Due to the energetically favoured adsorption of Gr on Ir(111), large terraces Gr/Ir(111) form along the $[\bar{1}10]$ direction, accompanied with (331) facets. In Fig. 5-7 this transition can be observed. While Fig. 5-7 a-c display the experimental STM data, Fig. 5-7 d visualizes the transition with a ball model.

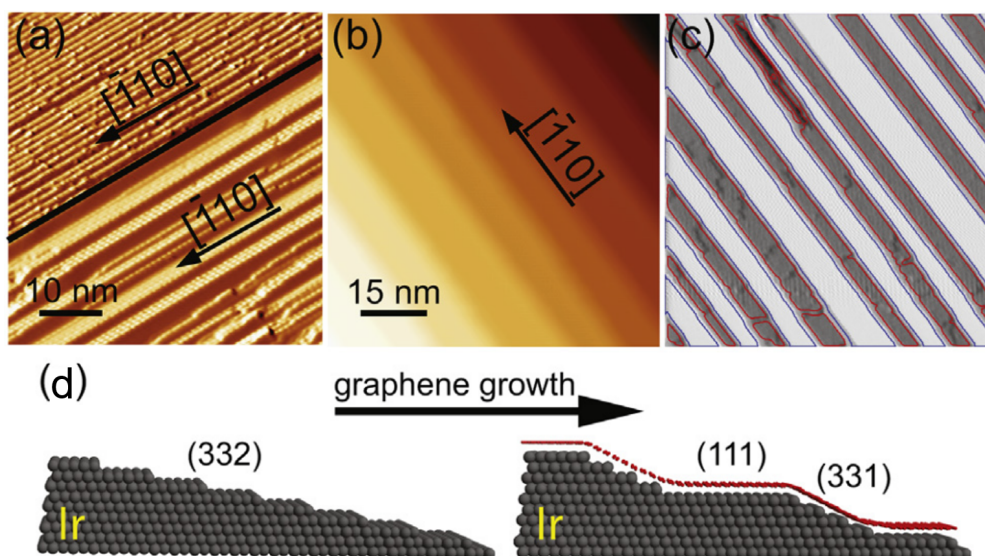


Figure 5-7.: Two differentiated STM images of the Ir(332) surface partially covered with Gr. The top part shows the bare Ir(332) surface, whereas the bottom part displays graphene-covered part. **b** STM topograph of a graphene-covered region. **c** Respective differentiated image. The lines indicate the dominant (111) and (331) facets. **d** Ball model indicating the restructuring of the surface after Gr growth. Adapted from [167].

It has been observed that EuCot nanowires on Gr/Ir(110) preferably orient along step edge bundles. Making use of this, growing EuCot nanowires on Gr/Ir(332) could combine the properties of large Gr/Ir(111) terraces with the globally-oriented wires of the growth on Gr/Ir(110). Of course, large areas of the sample are also covered with the Ir(331) facets, on which the growth behaviour of the EuCot nanowires is not known.

To reveal the influence on the magnetic properties of these substrates on EuCot nanowires, XANES and XMCD measurements have been performed. The sample on Gr/Ir(332) was mounted in that way, that grazing incidence measurements would be conducted along the expected wire direction.

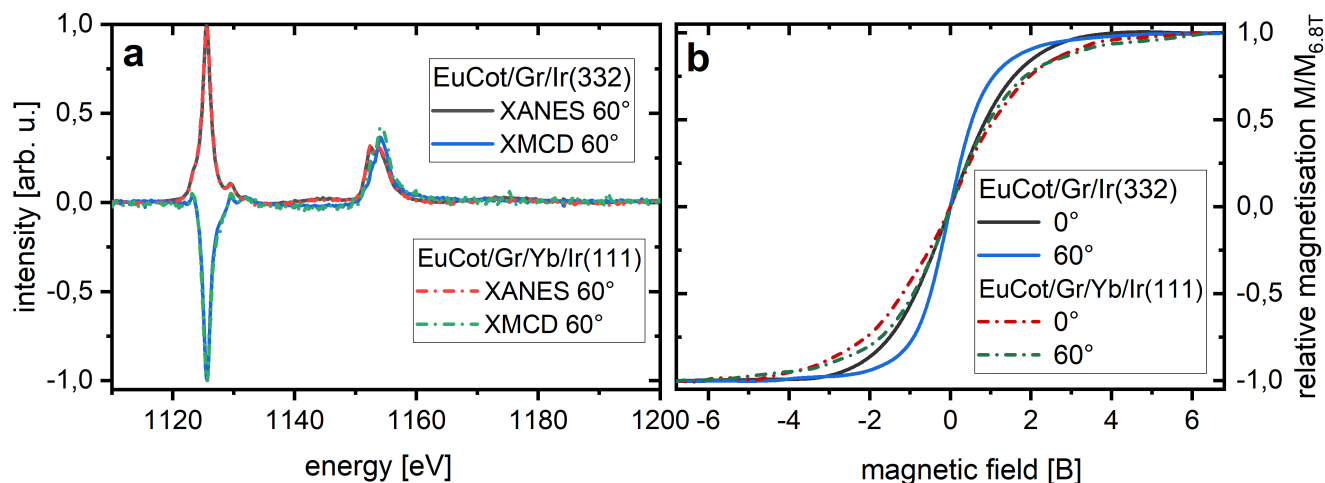


Figure 5-8.: **a** XANES and XMCD of EuCot nanowires on Gr/Ir(332) and Yb-intercalated Gr/Ir(111) for grazing incidence at a temperature of 3 K and a magnetic field of 6.8 T. **b** Respective magnetisation curves at 3 K for normal (0°) and grazing (60°) incidence normalised to the magnetisation at 6.8 T.

Fig. 5-8 **a** presents the XANES and XMCD spectra of the Eu $M_{4,5}$ edges of EuCot nanowires on Gr/Ir(332) and Yb-intercalated Gr/Ir(111). Similar to the spectra shown above, there is neither a significant difference in the XANES, nor in the XMCD. Both samples display no significant change in their electronic structure and are fully saturated. More interesting are the magnetisation curves displayed in Fig. 5-8 **b**. Again, both samples do not show an opening of the hysteresis curve at 3 K. The Yb-intercalated sample shows no significant difference between normal and grazing incidence. The susceptibility is equal to the one of EuCot nanowires on Gr/Ir(111). One can state, that doping the Gr substrate suppresses the ferromagnetic order while having no influence on the susceptibility.

In the case of EuCot on Gr/Ir(332), we see a difference between normal and grazing incidence similar to the ordered nanowires on Gr/Ir(110). Therefore we can assign this behaviour to the global orientation of the nanowires. But again, no opening of the hysteresis curve could be detected. One may think, that the ordered nanowires on the large terraces should behave similar to the ones on Gr/Ir(111), but the exact behaviour of the nanowires on Gr/Ir(332) has not been investigated yet. In addition, it could be plausible, that additional charge is present at these (111) terraces, due to the interaction with the neighbouring (331) facets. In order to get a deeper understanding of this system, further investigations are needed.

We have also studied different graphene-covered $4f$ -surface alloys as substrate for nanowire growth. The graphene-covered Dy surface alloy has been studied intensively and provides a magnetic strongly anisotropic substrate. An open question is if we see an interaction between this magnetically anisotropic substrate with the magnetic properties of the EuCot nanowires, as it has been shown for comparable systems, in which a magnetic substrate could induce magnetic order and drive a transition in single-molecule magnets [14]. In our case the easy axis of the substrate lays in-plane, which is similar to the ferromagnetic ordering of EuCot nanowires on Gr/Ir(111).

Fig. 5-9 **a** displays the LEED pattern of the graphene-covered Dy surface-alloy. This system has been described in detail in section 4.3. EuCot nanowires are grown on top of this substrate, represented by the EuCot specific ring pattern highlighted in Fig. 5-9 **b**. These LEED measurements have been taken directly prior to the XMCD measurements.

The STM topograph in Fig. 5-9 **c** displays the random orientation of EuCot nanowire islands on Gr/Dy/Ir(111). Also on this substrate, the well ordered wire-carpets form preferably monolayer islands with a small fraction of double layers, as visible in this overview image.

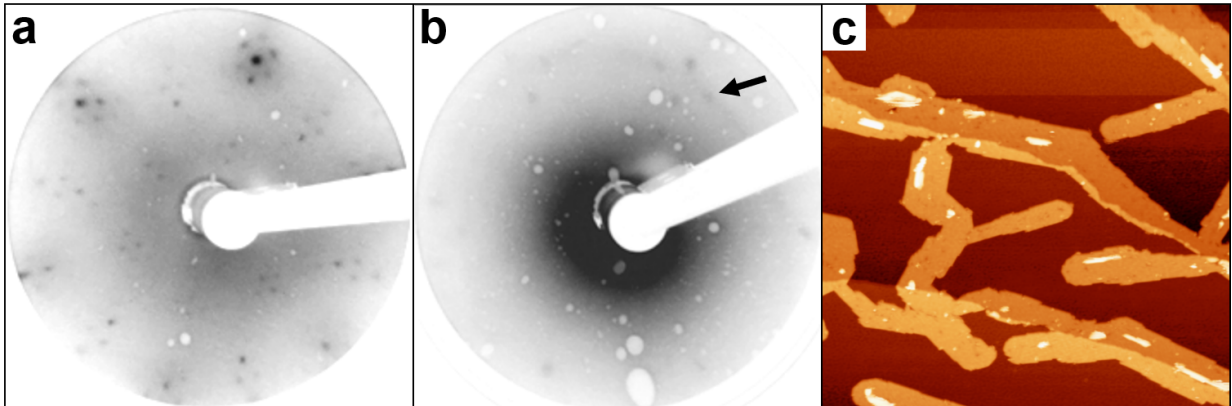


Figure 5-9.: **a** Contrast inverted LEED pattern of a graphene-covered Dy surface alloy on Ir(111) at 100 eV primary electron energy taken at the VEKMAG endstation. **b** Contrast inverted LEED pattern at 35 eV primary electron energy after the growth of EuCot nanowires on the sample represented in **a**. The arrow points at the ring representing the EuCot nanowires on Gr/Dy/Ir(111). **c** STM topograph of EuCot nanowire islands on Gr/Dy/Ir(111) (200 nm \times 200 nm). The tunneling parameters are $U_B = -2.60$ V, $I_T = 2.6 \cdot 10^{-11}$ A.

The results of the synchrotron-based measurements are presented in Fig. 5-10. It is important to mention, that these measurements have been performed at the VEKMAG endstation at BESSY II. A lower energetic resolution compared to the measurements at the X-Treme Beamline at the SLS is given by the experimental setup. In addition, a reduced degree of polarisation is caused by the bending magnet, which is the source of the X-rays at that beamline [146]. This is relevant for the XMCD signal, which reduces the overall XMCD

intensity. And at last, measurements of magnetisation curves of Eu show major problems at the VEKMAG endstation. The origin of this behaviour is not clear. Interestingly, this complication is also present at the DEIMOS endstation at SOLEIL.

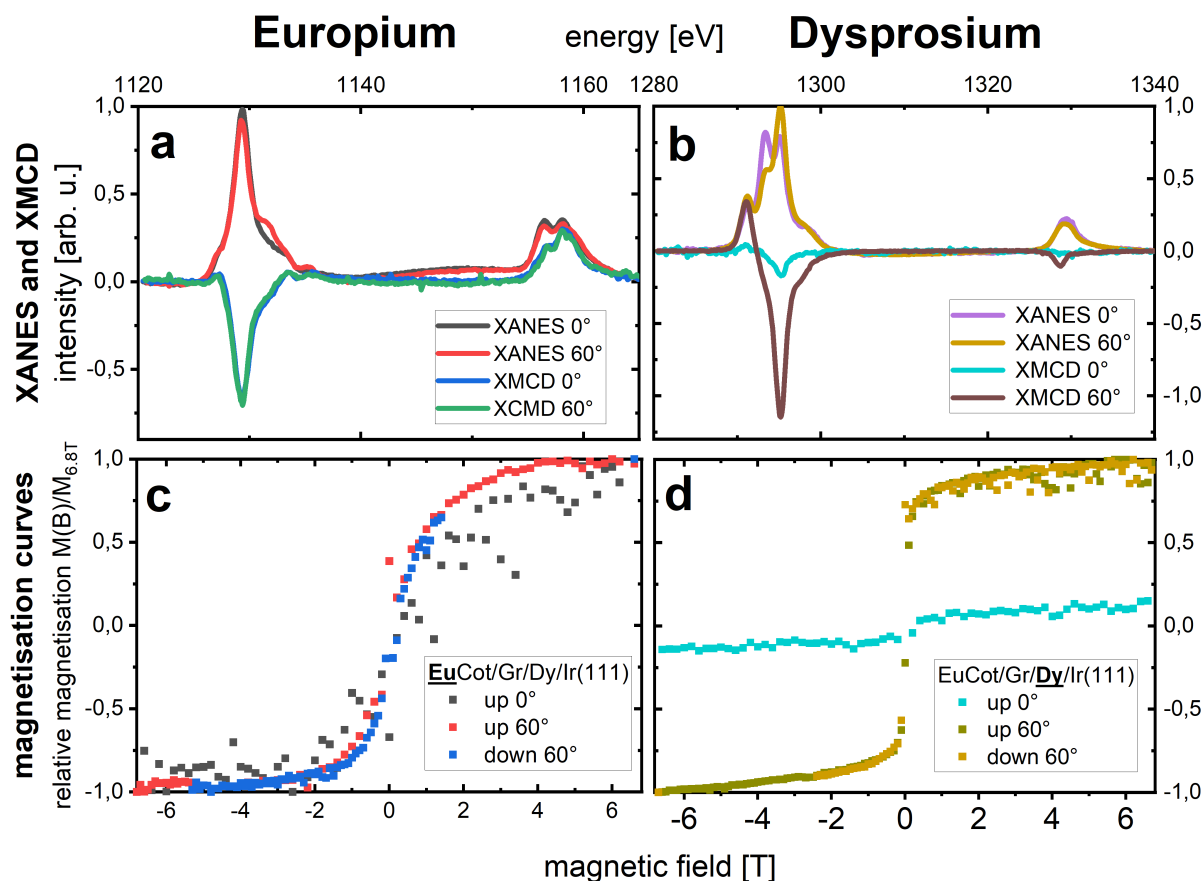


Figure 5-10.: XANES and XMCD of the $M_{4,5}$ edges of Eu **a** and Dy **b** of EuCot nanowires on a graphene-covered Dy surface alloy for normal (0°) and grazing (60°) incidence at a temperature of 3 K and a magnetic field of 6.8 T. (c,d) Respective magnetisation curves at 3 K for normal (0°) and grazing (60°) incidence normalised to the magnetisation of the respective sample at 6.8 T.

Fig. 5-10 presents the XANES and XMCD (**a**, **b**), as well as the magnetisation curves (**c**, **d**) of EuCot nanowires on graphene-covered Dy surface alloy. The XANES of the Eu M_5 edge for grazing incidence in Fig. 5-10 **a** displays a small shoulder at higher binding energies. This is an indication for slight oxidation of the EuCot nanowires, as this shoulder belongs to the Eu $4f^6$ configuration [168]. One should mention, that the base pressure of the measurement chamber was in the order of 10^{-9} mbar, which is much worse compared to our other experimental setups. Nevertheless, the influence is neglectable and due to the non-magnetic $4f^6$ state, there is no relevant influence on the magnetic properties. In contrast

to this, the Dy presented in Fig. **5-10 b** shows a strongly anisotropic behaviour. Although explained in detail in section 4.3, the Dy seems to exhibit an even stronger anisotropic behaviour, compared to Gr/Dy/Ir(111). That could be explained by the additional layer of EuCot nanowires on top of the Gr. A deeper understanding of this question could be provided by the magnetisation curves of Eu and Dy.

The issues of Eu measurements at this beamline have been mentioned above. Nevertheless, reliable data for grazing incidence measurements could be presented in Fig. **5-10 c**. There is no opening of a hysteresis loop visible. By comparing the susceptibility $\chi_{60} = \alpha(1.15 \pm 0.13)$ with the situation on Gr/Ir(111), we see a drastic increase. The EuCot nanowires on the graphene-covered surface alloy have even a higher susceptibility than the ordered wires on Gr/Ir(110) (there is an overlap of the errors), although the wires are not globally oriented on this substrate. The change in susceptibility can not be explained by the doping level, as shown by the Yb-intercalation, which induces no change in the magnetic susceptibility and therefore this is a strong indication of a magnetic interaction of the EuCot nanowires with the graphene-covered Dy surface alloy. For normal incidence, an interpretation is not possible due to the data quality.

Having a look at the Dy magnetisation curves in Fig. **5-10 d** we see similar behaviour to the graphene-covered Dy surface alloy. While there is a large magnetisation in the surface plane, the magnetisation normal to the surface is even smaller than for the case without EuCot nanowires on top. This increase in anisotropy could also be attributed to the magnetic interaction between the Dy atoms and the EuCot nanowires.

Variation of the molecule

Another approach to manipulate the magnetic properties of the Eu-based nanowires is the variation of the ligand. By adding methyl groups to Cot molecules, one can not only change the separation between the different wires. It also changes the charge distribution within the molecule, due to carbon bonds of the methyl group, that replaces a hydrogen atom. It is also important to check the aromaticity, as it is crucial for nanowire growth. But of course, one can think of stronger changes, e.g. by adding chlorine atoms, but the limits of chemistry have to be taken into account.

One available molecule is, as described above, 1,3,5,7-tetramethyl cyclooctatetraene, short TM-Cot. It consists of four evenly distributed methyl groups at the corners of the Cot molecule. How these changes influence the wire growth is depicted in Fig. 5-11.

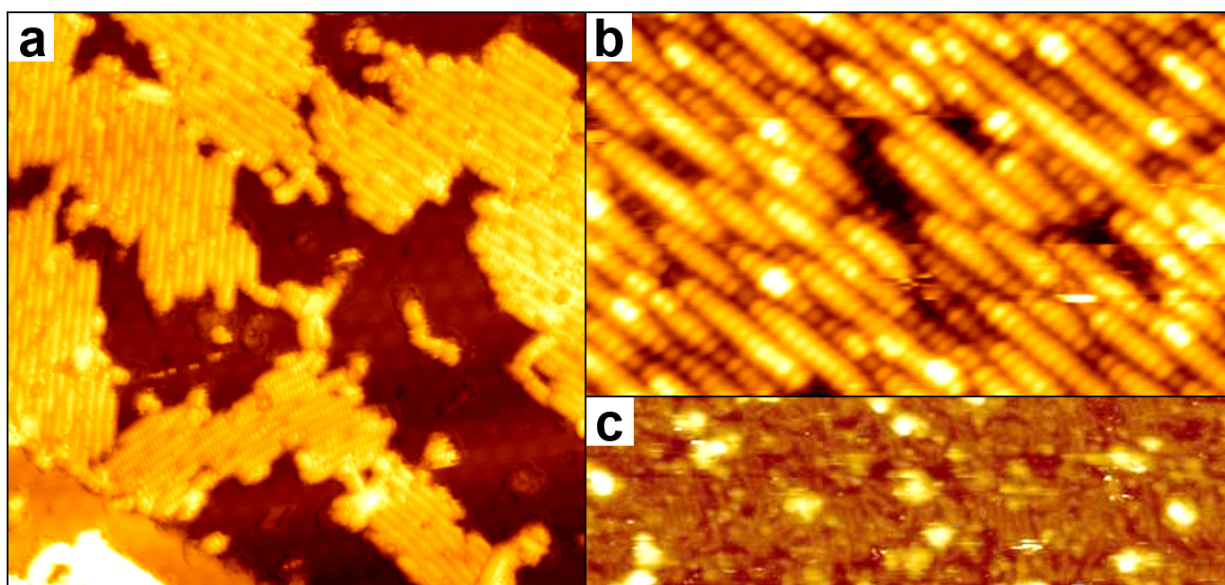


Figure 5-11.: **a** STM topograph of Eu-TM-Cot wire islands on Gr/Ir(111) ($65 \text{ nm} \times 65 \text{ nm}$). **b** Molecular-resolution STM topograph of a Eu-TM-Cot wire island on Gr/Ir(111) ($12 \text{ nm} \times 20 \text{ nm}$). **c** STM topograph of Eu-TM-Cot wires on Gr/Ir(110) with oxidised Eu piles, taken at the X-Treme endstation (SLS) ($82 \text{ nm} \times 24 \text{ nm}$). **a** and **b** adapted from [149].

Fig. 5-11 **a** displays an overview STM topograph of Eu-TM-Cot nanowire islands on Gr/Ir(111). Similar to EuCot nanowires on Gr/Ir(111), they form randomly oriented monolayer wire islands. The molecular resolution STM topograph in Fig. 5-11 **b** reveals differences, caused by the different ligands. The apparent height of the wires exhibits an intensity variation along the wire, which could be caused by different orientations of the methyl groups of the ligand. The inter-wire distance is significantly increased to $(10 \pm 1) \text{ \AA}$, compared to Eu-Cot nanowires on Gr/Ir(111). The apparent island height is also increased, which indicates

a larger separation of the Eu atoms from the substrate. In order to understand the change induced by the new ligands, XANES and XMCD measurements have been performed. The STM topograph in Fig. 5-11 c displays the sample, grown at the X-Treme endstation. Two structures are visible. On the one hand, mostly well-oriented wires that cover a large fraction of the surface, and on the other hand piles of oxidised Eu. The reason for the oxidation is not clear, but we will explain below, how we are still able to extract the magnetic properties of the nanowires.

To understand how we analysed the spectra presented in Fig. 5-12, it is important to mention, that oxidised Eu (Eu_2O_3) has an electron configuration of $4f^6$, which is a completely non-magnetic state, as spin and orbital moment cancel each other. We measured the $M_{4,5}$ -edge of Eu oxide on Ir(111) before, which enabled us to separate the $4f^6$ and $4f^7$ contributions in our spectra.

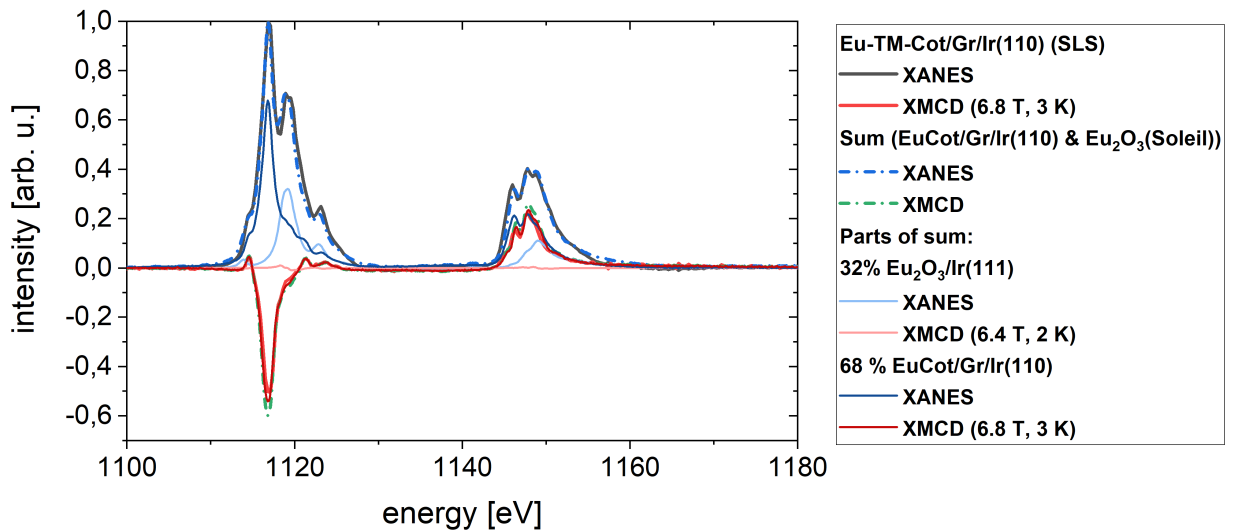


Figure 5-12.: XANES and XMCD of the Eu-TM-Cot on Gr/Ir(110) sample measured at the SLS compared to a sum of $\text{Eu}_2\text{O}_3/\text{Ir}(111)$ and an $\text{EuCot}/\text{Gr}/\text{Ir}(110)$ in order to disentangle their contributions. The summands are indicated with thin lines.

To do so, a fit consisting of the spectra of EuCot nanowires on $\text{Gr}/\text{Ir}(110)$ and the Eu oxide on $\text{Gr}/\text{Ir}(111)$ is applied, in which the weight of the components is chosen that way, that the difference between the experimental spectra of the Eu-TM-Cot nanowires on $\text{Gr}/\text{Ir}(111)$ and the fit is minimal. On the one side, this allows us to separate the oxide contribution and allows us to analyse the XANES and XMCD of the nanowires. The fit indicated as dotted lines fits very well for XANES and XMCD. That leads to the conclusion, that there are no significant differences in the XANES of EuCot and Eu-TM-Cot nanowires. In addition, we can state that the Eu-TM-Cot nanowires are also fully saturated at 6.8 T and 3 K.

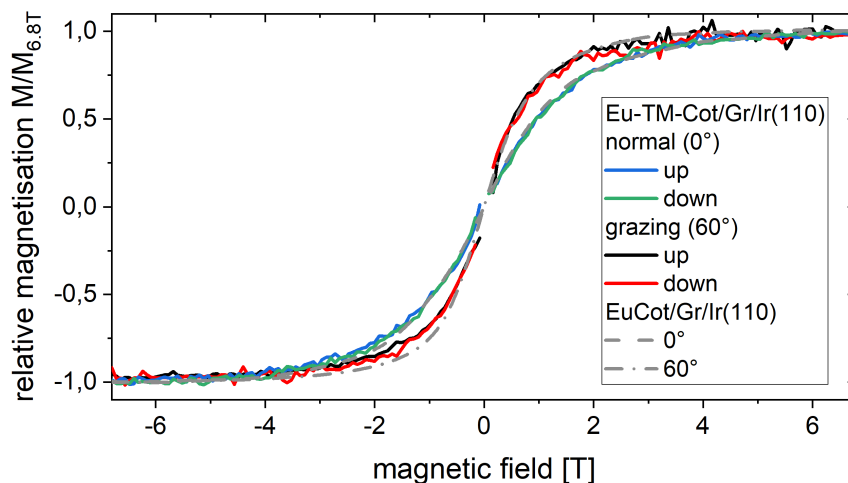


Figure 5-13.: Magnetisation curves of the Eu-TM-Cot sample on Gr/Ir(110) for normal (0°) and grazing (60°) at a temperature of 3 K. The dotted grey lines indicate the magnetisation curves of EuCot on Gr/Ir(110) as a comparison.

The magnetisation curves presented in Fig. 5-13 describe the magnetic properties of the Eu-TM-Cot nanowires only, as $\text{Eu } 4f^6$ has no contribution to the XMCD signal. In comparison, the curves of EuCot nanowires on Gr/Ir(110) are added. The comparison shows immediately that there is no significant difference between both curves. This states, that the separation of the wires, as well as the different charge distribution in the ligand, do not have a significant influence on the magnetic properties. Also, they do not lead to an opening of a hysteresis loop.

Changing the ligand from Cot to TM-Cot may lead to a structural change, but to significantly improve the magnetic properties, nanowires with different molecules have to be evaluated. One interesting molecule would be Borata-Cot, which is theoretically proposed to introduce half-metallicity and a stronger ferromagnetic coupling into the EuCot system [105].

5.3. Thulium-Cyclooctatetraene Compounds

After the discussion of Eu-based nanowires in the previous sections, a new $4f$ -metal is introduced in these organometallic compounds. Tm forms a number of different structures with Cot. In this chapter, we will describe TmCot dots, TmCot double deckers, TmCot coffee beans, and TmCot nanowires. The synthesis and the structure of these systems are described in detail in Ref. [164]. As a relevant background to the element-specific measurements presented in this section, these systems are introduced briefly in the following.

Fig. 5-14 displays two of these systems, TmCot dots and TmCot double deckers. A schematic sketch of them is presented in Fig. 5-14 a. On the left-hand side, TmCot double deckers are presented. The name is given by the two Cot molecules, which bind to the Tm atom in between, leading to a formula unit of Tm_1Cot_2 . As indicated these molecules do not bind to the substrate chemically. This statement will be discussed in more detail below. On the right-hand side, TmCot dots are sketched. In this case, the Tm sits between the Gr and the Cot atom sits on top of this Tm atom. The adsorption energy of this structure is much larger compared to the double deckers. Nevertheless, the imaging of the dot phase is only possible at very low temperatures.

Such an STM topograph is presented in Fig. 5-14 b. The dots appear as bright protrusions. The separation is rather regular and matches the Gr/Ir(111) moiré lattice. The separation indicates, that the dots are charged and repel each other. In the close-up scan presented in the inset, a ring-like feature can be obtained, which is attributed to the Cot ring. The line profile in Fig. 5-14 f shows the dip central above the dot.

In contrast to the dots, the double decker molecules can not be prepared and studied at room temperature, as they desorb at these temperatures. Therefore double deckers can only be prepared by evaporating Tm in a thick layer of adsorbed Cot molecules on a substrate cooled below the desorption temperature. Such preparation is shown schematically in Fig. 5-14 c. The random oriented Tm double deckers are embedded in the thick layer of Cot adsorbed on Gr/Ir(111).

The desorption mentioned above has been studied by thermal desorption spectroscopy (TDS). The TDS spectra for two different amounts of Tm evaporated into a thick layer of adsorbed Cot molecules in Gr/Ir(111) is presented in Fig. 5-14 d. Independent of the amount, a desorption peak arises for the mass of the TmCot double deckers (377 amu) at a temperature of (157 ± 2) K, which represents the desorption of TmCot double deckers. In contrast to this, a similar TDS measurement of TmCot dots on Gr/Ir(111) for the masses of the TmCot dots and the TmCot double deckers (273 amu and 377 amu) do not exhibit any desorption peak, as presented in Fig. 5-14 e. With this, we can conclude that TmCot dots do not desorb at temperatures up to 1000 K. This supports the idea of the van-der-Waals type of binding for the TmCot double deckers, whereas the dots are chemically bound to the substrate.

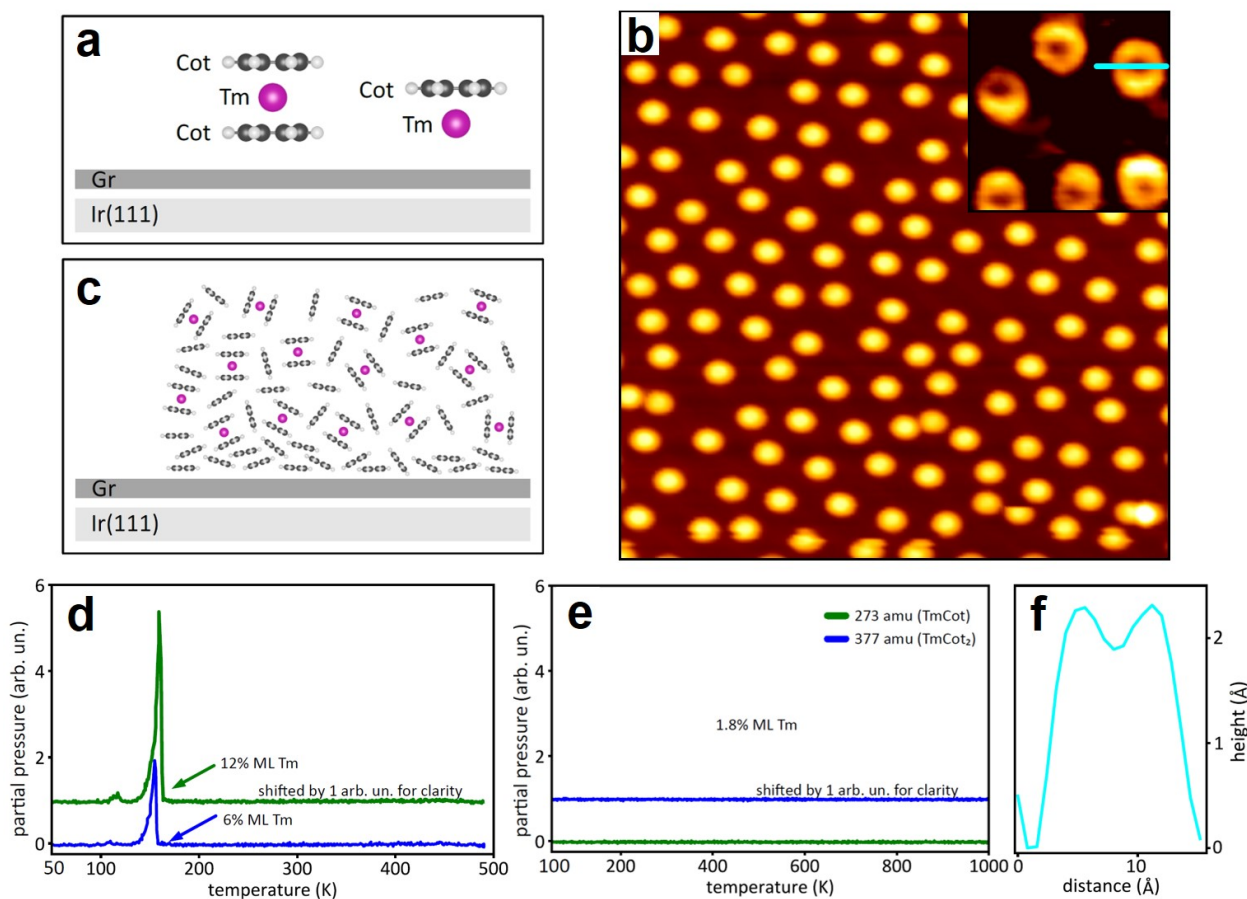


Figure 5-14.: **a** Schematic side view sketch of TmCot double decker (left) and TmCot dot (right) on a Gr/Ir(111) substrate. **b** STM topograph of TmCot dots after deposition of 0.08 ML Tm in Cot vapor on a Gr/Ir(111) substrate at 20 K (25nm × 25nm). The inset shows a magnified view of the dots (3.6nm × 3.6nm). The blue line indicates the height profile displayed in **f**. **c** Schematic side view sketch of TmCot double decker formation after deposition of Tm into a thick layer of adsorbed Cot molecules on Gr/Ir(111) at 20 K. **d** Temperature-programmed desorption of sample created in **c**. A mass of 377 amu characteristic for TmCot double deckers is detected with a heating rate of 10 K/s for two different amounts of Tm. **e** Temperature-programmed desorption of a TmCot dot sample after the deposition of 0.18 ML Tm with a rate of 10 K/s for the masses 273 amu and 377 amu corresponding to dots and double decker. **f** STM height profile over TmCot dot indicated in the inset in **b**. All adapted from [164].

Fig. 5-15 **a** presents XANES and XMCD spectra of TmCot dots on Gr/Ir(111). The $M_{4,5}$ -edges of Tm, measured at low temperatures and a magnetic field of 6.8 T, indicate a $4f^{12}$ electron configuration and show an anisotropic behaviour. The XANES for normal incidence reflects a narrow peak, whereas the grazing incidence measurement has a strong shoulder at lower energies, indicating strong linear dichroism. The M_4 -edge is very small and cannot be distinguished from the noise. The noise level can be explained by the wide separation of the dots, leading to a Tm coverage of the surface of around 1% of a ML_{Ir} .

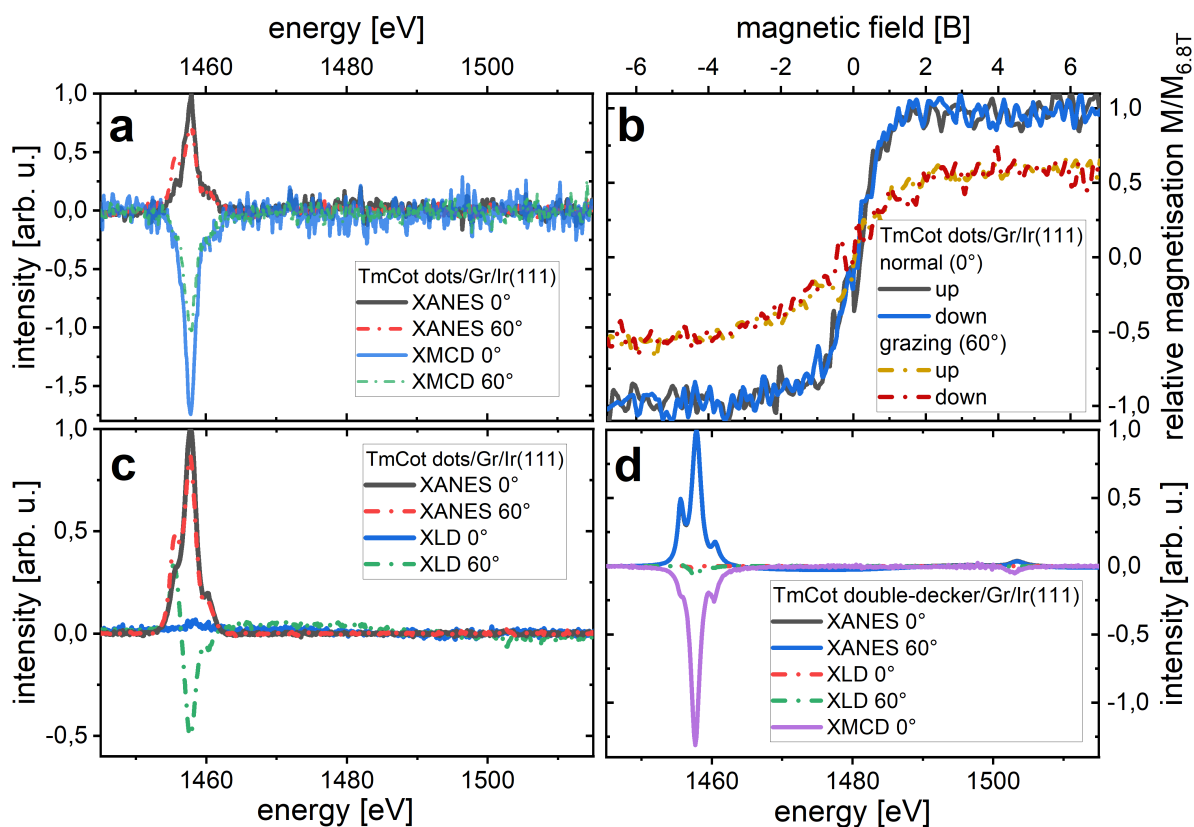


Figure 5-15.: **a** XANES and XMCD spectra of the $M_{4,5}$ -edges of Tm of TmCot dots on Gr/Ir(111) for normal (0°) and grazing (60°) incidence at a temperature of 3 K and a magnetic field of 6.8 T. **b** Respective magnetisation curves at 3 K for normal (0°) and grazing (60°) incidence, normalised to the normal magnetisation at 6.8 T. **c** Respective XANES and XLD spectra of the TmCot dots on Gr/Ir(111) for normal (0°) and grazing (60°) incidence at a temperature of 3 K and a magnetic field of 6.8 T. **d** XANES, XLD, and XMCD spectra of TmCot double-decker on Gr/Ir(111) for normal (0°) and grazing (60°) incidence at a temperature of 3 K and a magnetic field of 6.8 T (0.05 T for the XLD).

The XMCD signal displays also a strong magnetic anisotropy. The easy axis sits out-of-plane along the Tm-Cot binding axis, similar to the anisotropy in the EuCot wires, which

has their easy axis along the Eu-Cot binding as well. Evaluating the sum-rules results in $\mu_S - 6\langle T_Z \rangle = -3.82 \mu_B$ and $\mu_L = -3.82 \mu_B$ for normal incidence and $\mu_S - 6\langle T_Z \rangle = -2.52 \mu_B$ and $\mu_L = -2.52 \mu_B$ for grazing incidence. The similar values are caused by the indistinguishable M_4 -edge. Nevertheless, the dipolar term $\langle T_Z \rangle$ is very relevant for Tm, as also discussed in chapter 4.4. Including $\langle T_Z \rangle$, which have been calculated by multiplet calculations to be $\langle T_Z \rangle = -0.303$ for normal incidence and $\langle T_Z \rangle = -0.199$ for grazing incidence, the moments change to $\mu_S = -2.01 \mu_B$ and $\mu_L = -3.82 \mu_B$ for normal incidence and $\mu_S = -1.32 \mu_B$ and $\mu_L = -2.52 \mu_B$ for grazing incidence.

This large anisotropy is also represented in the magnetisation curves in Fig. 5-15 b. Both curves display a paramagnetic behaviour and no opening of a hysteresis loop can be identified outside the noise level. The curve saturates between 2 T and 3 T. An insight on the electronic properties is given by the XLD measurements, presented in Fig. 5-15 c. A higher photon flux allowed a much better signal to noise ratio. By comparing the XANES for normal and grazing incidence, a similar behaviour to the XANES depicted in Fig. 5-15 a is present. The extremely large XLD signal for grazing incidence implies a really strong out-of-plane charge anisotropy, while the signal is neglectable in-plane. The strong charge anisotropy of the $4f$ -shell is in line with the binding of the Tm atoms to the surface and the molecule. This is a clear indication, that there is a relatively strong interaction between the binding and the $4f$ -electrons. This contributes to the discussion if the $4f$ -electrons are so localised, that there is no significant interaction with the surrounding of the atoms. In line with the results presented in chapter 4, we can state, that there is a significant influence of the surrounding on the $4f$ -electrons, e.g. by hybridising with the $5d$ -states [164].

Fig. 5-15 d presents the experimental spectra of TmCot double deckers. The preparation at the beamline was tricky, as the sample needed to be below 150 K for the whole transfer process between the preparation chamber and the cryostat. The XANES indicates a clear $4f^{12}$ state and is isotropic, also represented in the neglectable XLD signal. It is important to mention, that this is not clear information about the single molecule itself but rather attributed to the random orientation of the TmCot double decker within the thick Cot layer (compare Fig. 5-14 c). The averaged magnetisation determined by the sum-rules is $\mu_S - 6\langle T_Z \rangle = -2.10 \mu_B$ and $\mu_L = -2.33 \mu_B$ and including $\langle T_Z \rangle = -0.184$ from the multiplet calculation, the moments are given as $\mu_S = -1.00 \mu_B$ and $\mu_L = -2.33 \mu_B$.

Besides the TmCot dots and TmCot double deckers described above, there are additional TmCot compounds. Further increasing the TmCot density by evaporating larger amounts of Tm in Cot background pressure on Gr/Ir(111) leads to the nucleation of so-called coffee-bean island, which are named after their apparent structure. The STM topograph in Fig. 5-16 a depicts the two coexisting phases. The inset presents the molecular resolution. Such a coffee bean consist of 12 Tm atoms, but the exact structure could not be determined.

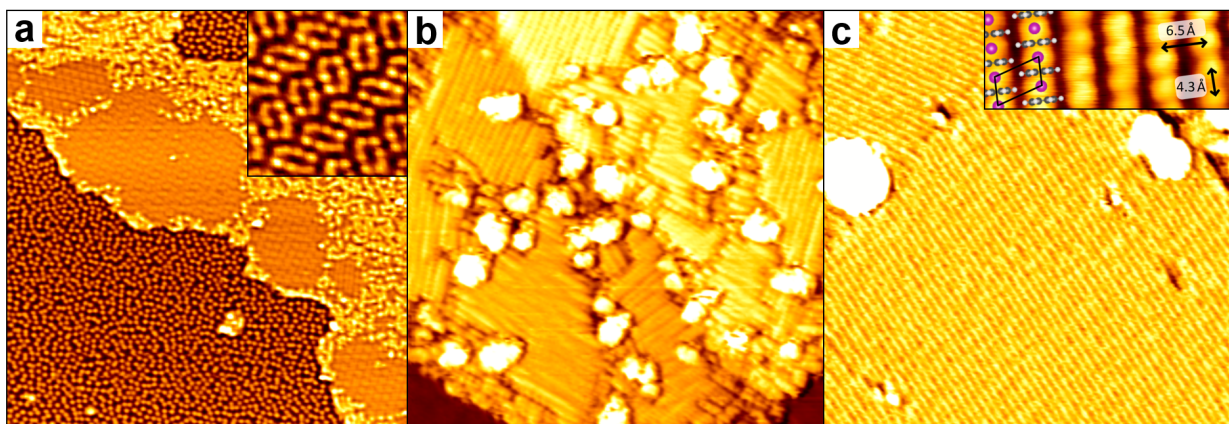


Figure 5-16.: **a** STM topograph of TmCot dots in coexistence with coffee-bean phase islands after deposition of 0.14 ML Tm in Cot vapor ($80 \text{ nm} \times 80 \text{ nm}$). The inset displays the molecular resolution of the coffee-beans ($7.5 \text{ nm} \times 7.5 \text{ nm}$). **b** STM topograph of TmCot nanowires after deposition of 0.12 ML Tm in Cot vapour on Gr/Eu/Ir(111) at a temperature of 300 K ($35 \text{ nm} \times 35 \text{ nm}$). **c** STM topograph of a sample similar to **b**, but synthesized at 350 K ($35 \text{ nm} \times 35 \text{ nm}$). The inset presents the molecular resolution of the sandwich-molecular nanowires ($4.2 \text{ nm} \times 1.5 \text{ nm}$). The intra- and interwire repeat distances are indicated and a ball model is overlaid indicating the unit cell. All adapted from [164].

More interesting are the structures presented in Fig. 5-16 **b** and **c**: TmCot nanowires. As mentioned in section 5.1, Cot molecules need to accept two electrons to be aromatic and therefore allow wire growth. In the structures presented above, Tm exhibits a 3+ oxidation state, which is the favoured configuration of Tm [107]. In order to allow wire growth, Tm has to be in a 2+ oxidation state. By n-doping the substrate, the reaction path of Tm can be changed. While there are coffee beans forming on Gr/Ir(111), exclusively nanowires are formed on Eu-intercalated Gr/Ir(111), because the initial formation of TmCot dots is prevented. This intriguing change of the reaction path is also backed by DFT calculations, which imply that the adsorption energy of the dots is increased from -2.16 eV to -1.51 eV by the additional charge of the Gr provided by Eu intercalation [164]. With a wire formation energy gain of -2.11 eV per formula unit, this change in adsorption energy allows the wire growth [164].

The STM topograph in Fig. 5-16 **b** presents a wire island after the growth of nanowire islands on Gr/Eu/Ir(111) at room temperature. Wires with random orientation and partial double-layer island are present. Increasing the growth temperature to 350 K and optimising Tm/Cot flux ration leads to islands with larger domains, as depicted in Fig. 5-16 **b**. The inset shows the molecular resolution of the nanowires.

It would be of special interest, to experimental proof the transition from the 3+ to the 2+ oxidation state of Tm. One option would be XPS measurements, but Tm $3d_{5/2,3/2}$ edges are

just above the excitation energy of a standard Al K_α cathodes. Obviously, XANES would be a perfect method to analyse changes in the electronic structure. The limitation is hereby the very sensitive nature of the TmCot nanowires. As the doping of the graphene forces the Tm into the 2+ oxidation state, any interaction with oxygen immediately oxidises the wires into their favoured 3+ state. Such a transition can be caused by non-perfect UHV conditions.

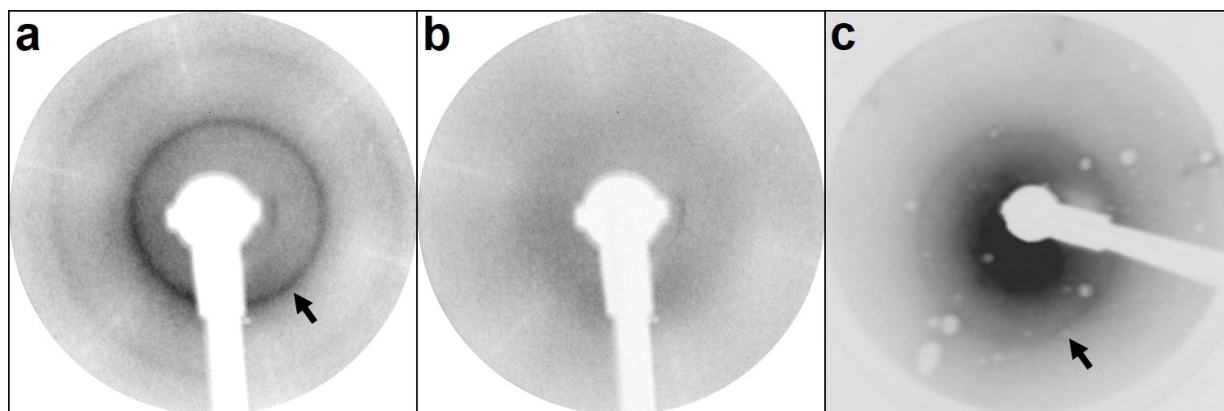


Figure 5-17.: **a** Contrast inverted LEED pattern of TmCot nanowires on Gr/Ir(111) at 40 eV primary electron energy and a temperature of 30 K. **b** Contrast inverted LEED pattern of the sample shown in **a** after exposure to $1 \cdot 10^{-7}$ mbar air for 15 min at 40 eV primary electron energy and a temperature of 30 K. **c** Contrast inverted LEED pattern of TmCot nanowires on Gr/Ir(111) at 30 eV primary electron energy at a temperature of 100 K taken at the preparation chamber of the VEKMAG beamline. The black arrows indicate the ring-like features of the TmCot nanowires. **a** and **b** taken from [169].

The experiments presented in Fig. 5-17 **a** and **b** visualizes the effect of non-perfect UHV conditions on the TmCot nanowires. The LEED pattern in Fig. 5-17 **a** displays a ring structure, which indicates well ordered TmCot nanowires. After the exposure to $1 \cdot 10^{-7}$ mbar air for 15 min, the rings vanished and therefore the wires oxidised and measurement would result in a 3+ oxidation state of Tm.

Fig. 5-17 **c** represents a sample that was grown at the preparation chamber of the VEKMAG beamline at BESSY II. The clear ring indicates a successful wire growth. The measurement showed an $4f^{12}$ electronic state, but there were no indications for intact nanowires after the measurement. Transfers in the order of 20 min are necessary at all beamlines with separate preparation chambers. But there is one exclusion. The preparation chamber at VEKMAG has the option, to measure XANES spectra right in the preparation chamber without needing a transfer. But sadly, this option was broken and therefore not available at our beamtime, so we were not able to measure intact TmCot nanowires.

5.4. Conclusion and Outlook

In this chapter, we investigated and manipulated the element-specific magnetic and electronic properties of EuCot nanowires by inducing global order, shifting the chemical potential, interaction with a magnetic anisotropic substrate, and by varying the organic ligand.

By ordering EuCot nanowires globally by utilising the anisotropic substrate Gr/Ir(110), the magnetic easy axis of the wires could be revealed, which lies along the wires. Although the wires display a similar electronic structure and are also magnetically saturated at high fields and low temperatures, an opening of the hysteresis curve as presented in Ref. [18] for EuCot nanowires on Gr/Ir(111), could not be detected, whereas the opening of the hysteresis on Gr/Ir(111) could be confirmed. Even for ordered multilayers of EuCot nanowires on Gr/Ir(110) no ferromagnetic order could be observed.

The globally ordered sample allowed first APRES measurements on EuCot nanowires and therefore 1D organometallic compounds in general, which revealed a broad flat band at -1.85 eV, but no dispersion of this band. XPS measurements of EuCot nanowires and BaCot nanowires proved experimentally, that this flat band can be assigned to the $4f$ -electrons.

The influence of the Gr doping level on the ferromagnetic order of EuCot nanowires is addressed by the measurement of EuCot nanowires on Yb-intercalated Gr/Ir(111). While there is no change in the electronic properties or the magnetic susceptibility compared to EuCot nanowires on Gr/Ir(111), there is no ferromagnetic order at 3 K. This indicates, that the ferromagnetic order is suppressed by the additional charge available. This could be either caused by the doping level of the graphene, for which DFT calculations suggest an increased ferromagnetic coupling for p-doping [170]. Or the increased interaction with the substrate due to the additional charge carriers would lead to a fast decay of the ferromagnetic state [5], which could also explain the missing ferromagnetic order on Gr/Ir(110). A simple experiment to answer this question would be XMCD measurements of EuCot nanowires on p-doped Gr/Ir(111), e.g. by chlorine doping [171].

The investigation of EuCot nanowires on Gr/Ir(332) tried to combine the order of Gr/Ir(110) with small terraces of Gr/Ir(111). The measured susceptibility indicates, that aligning along the step edges is possible. But again, no ferromagnetic order has been detected. In order to get a better understanding of this system, structural investigations should be performed.

By combining the magnetically strongly anisotropic substrate of a graphene-covered Dy surface alloy with EuCot nanowires grown on top, the magnetic interactions of the nanowires with a magnetic substrate could be studied. The interaction leads to the highest measured susceptibility along the wires of all samples measured, indicating a coupling constant $J > 0$ between the Eu and the Dy, which also has its easy axis in-plane. This shows the potential of such surface alloys, to manipulate the magnetic properties of any structure grown on top, which may be useful for spintronic applications.

The variation of the ligand, namely replacing Cot by TM-Cot has some influence on the structure, e.g. an increased inter-wire distance, but the influence on the electronic and

magnetic properties of the Eu is negligible. This proves that the inter-wire interaction in EuCot nanowire carpets does not play a significant role, at least for the probed molecules. Nevertheless, the influence on the Eu could significantly change, if stronger changes are applied to the molecule, e.g. by adding chlorine instead of hydrogen. But of course, the availability of such molecules, as well as the ability to form nanowires, limit possible future experiments.

From the Tm compound discussed in this chapter, TmCot dots are of special interest. First of all, they exhibit a very strong out-of-plane anisotropy. When looking for high-density storage devices, such out-of-plane anisotropy is favoured. Next, the $4f$ shell of Tm displays a very strong anisotropy in the binding axis, expressed by the large XLD signal. This indicates a strong interaction between the $4f$ states and the local surrounding of the atom. While textbooks describe $4f$ states as strongly localised and therefore shielded by the outer electrons, the discussion about interaction and hybridisation has gathered more attention lately [172]. DFT calculations already indicate $4f - 5d$ hybridisation for the TmCot dots on Gr/Ir(111) [164], but these XLD results are a strong experimental indicator for such interaction. At last, such systems are just in the gap between single-molecular magnets [59] and single-atom magnets on Gr/Ir(111) [155], which could lead to very interesting properties. Therefore investigating other lanthanide-Cot dots on Gr/Ir(111) could introduce a new window for high-density data storage applications, but also introducing Cot molecules on more stable structures like the $4f$ surface alloys could lead to extremely interesting magnetic properties, that are worth exploring.

The change of the reaction path of TmCot on Gr/Ir(111) by doping, leading to TmCot nanowires on n-doped Gr is interesting. It would be desirable, to explore the magnetic properties and experimentally prove the change of the oxidation state. This could be realised by using a Cu K_α anode at an in-situ XPS set-up or having access to a properly working VEK MAG endstation.

6. Summary

In this work, we explored a variety of different low-dimensional $4f$ systems, reaching from the $4f$ surface alloys in chapter 4 to the metalloorganic systems in chapter 5. We investigated the synthesis and the structure of these systems and focused on the element-specific investigation of the electronic and magnetic properties of the relevant $4f$ elements. By combining this experimental approach with *ab initio* and ligand field multiplet theory, we gained a comprehensive understanding of these systems.

In chapter 4, we established the synthesis of $4f$ Ir surface alloys and graphene-covered $4f$ surface alloys. Our LEED and STM measurements revealed the structure of these systems, including the surface alloy formation at high temperatures. *Ab initio* calculations supported the experimental finding and proposed a graphene-induced selective skyhook effect, i.e. a selective lifting of the $4f$ metals out of the surface alloy. It also proposes a massive increase of the coupling constant upon Gr adsorption, which has so far only been reported theoretically for $3d$ metals. Using synchrotron-based XANES and XMCD measurements, we revealed a massive increase of electronic and magnetic anisotropy in the $4f$ shell, due to the selective skyhook effect. A ferromagnetic order could not be shown, but due to the negligible in-plane anisotropy, a coercive field far below our experimental error is expected. Future MOKE measurements are planned and will show if a ferromagnetic order arises upon Gr adsorption. Based on our DFT based crystal field model employed for our multiplet calculation, we provided experimental proof of the proposed skyhook effect, by utilizing XLD measurements. Extending the variety of systems by including other $4f$ elements allowed us to generalize the selective skyhook effect, as all the probed systems showed a lifting of the $4f$ metals. We also see a general trend of Gr adsorption favouring in-plane magnetisation of the $4f$ elements, while increasing $4f$ occupancy changes the easy-axis systematically from in-plane for Tb ($4f^8$) to out-of-plane for Tm ($4f^{12}$). Our multiplet approach also allowed us to determine the dipolar term T_Z systematically. XPS measurements of these systems displayed an n-doping of the adsorbed graphene, which is independent of the $4f$ species used. In combination with the structural intact graphene, this system provides a platform with tunable magnetic anisotropy for possible spintronic applications.

Such possible building blocks for spintronic application have been investigated in chapter 5. EuCot nanowires, which have been proved to be ferromagnetic insulators on Gr/Ir(111), may be used as spin filters. In our work, we studied the influence of different substrates on these systems. While inducing global orientation by utilizing the newly introduced substrate Gr/Ir(110) (comp. A.1) increases the susceptibility due to the alignment and therefore proves,

that the easy axis lies along the wires, no ferromagnetic order could be measured. By doping the Gr/Ir(111) substrate, we could show, that the ferromagnetic order is lost upon changes in the electronic structure of Gr. We attribute this change to the loss of the close to free-standing Gr properties on Ir(111) and therefore the loss of its insulating properties. Similar behaviour could be seen for Gr/Ir(332) and Gr/Dy/Ir(110). The interaction with the anisotropic graphene-covered Dy surface alloy revealed a strong increase of the susceptibility, providing the first proof of our concept of magnetically manipulating adsorbed systems, relevant for future spintronic applications. It also proved that the on-surface synthesis is not hindered by the underlying surface alloy. However, a change of the reaction path by Eu intercalation could be shown for TmCot compounds. On the one hand, TmCot dots which form on pristine Gr/Ir(111) display a massive electronic and magnetic anisotropy which is of special interest for the understanding of $4f$ magnetism and in combination with its out-of-plane easy axis, provides a very promising system, to be investigated in further studies. On the other hand, TmCot nanowires form on Eu doped Gr/Ir(111), similar to the EuCot nanowires. Sadly, we were not able to study TmCot nanowires by the means of XANES and XMCD.

Concerning future projects, the main focus lies on the $4f$ surface alloys. Besides the use as a substrate with tunable magnetic properties, adsorption of different systems onto the bare surface alloy could lead to promising systems, e.g. Cot adsorption could introduce a regular array of slightly coupled moments with similar properties as the dot phase. But the dot-phase itself could show intriguing properties upon the variation of the $4f$ element. One could think of single-molecular magnets, ordered with respect to the Gr moiré. In general, the understanding of $4f$ magnetism combined with the establishment of new nanosized organometallic systems paves the road for future energy-efficient spintronic devices.

A. Scientific Appendix

A.1. Graphene on Ir(110)

The work presented in this section is based on S. Kraus, F. Huttmann, J. Fischer, T. Knispel, K. Bischof, **A. Herman**, M. Bianchi, R. Stan, A. Holt, V. Caciuc, S. Tsukamoto, H. Wende, P. Hofmann, N. Atodiresei, and T. Michely. Single-crystal graphene on Ir(110) [37]. Although my contribution to this publication was limited to beam time support, Gr/Ir(110) has been intensively used in this work (compare section 5.1 and 5.2). Therefore, the growth process will be described briefly and additional XPS measurements are presented.

The Ir(110) surface is energetically less stable than e.g. the Ir(111) surface, which leads to a surface reconstruction. Surface reconstructions have already been introduced in section 5.2. The clean Ir(110) surface is faceted, consisting of (331) and $(3\bar{3}\bar{1})$ facets. Due to the faceting, besides the reactivity of the bare metal, this surface is not favourable for on-surface synthesis. The faceting can be suppressed by oxygen adsorption during the cool-down process. Another option to prevent faceting is the growth of Gr.

Fig. **A-1 a** presents an overview STM topograph of Gr/Ir(110). It displays large terraces of Gr/Ir(110) with step-edges bundles between them, as indicated in the height profile. Fig. **A-1 b** shows an atomic scale STM topograph. The Gr is well ordered and has no other domains. To obtain single-domain Gr, growth temperatures as high as $T = 1500$ K are necessary. The lower growth temperature $T = 1300$ K leads to the formation of two-domain Gr. The high order of Gr/Ir(110) is also represented in the LEED pattern in Fig. **A-1 c**. The reflections of Gr and Ir(110) are indicated by circles, as well as the primitive moiré translations. There are no rotated domains visible in this pattern.

The well-ordered substrate in combination with its two-fold symmetry makes Gr/Ir(110) an ideal template for globally ordered structures, as thoroughly discussed in section 5.1. A question which arises is, how the strong interaction of the substrate with Gr, in contrast to Gr/Ir(111), influences the properties of the Gr and adsorbed species. This can be answered by theoretical DFT calculations, as well as experimental photoelectron spectroscopy.

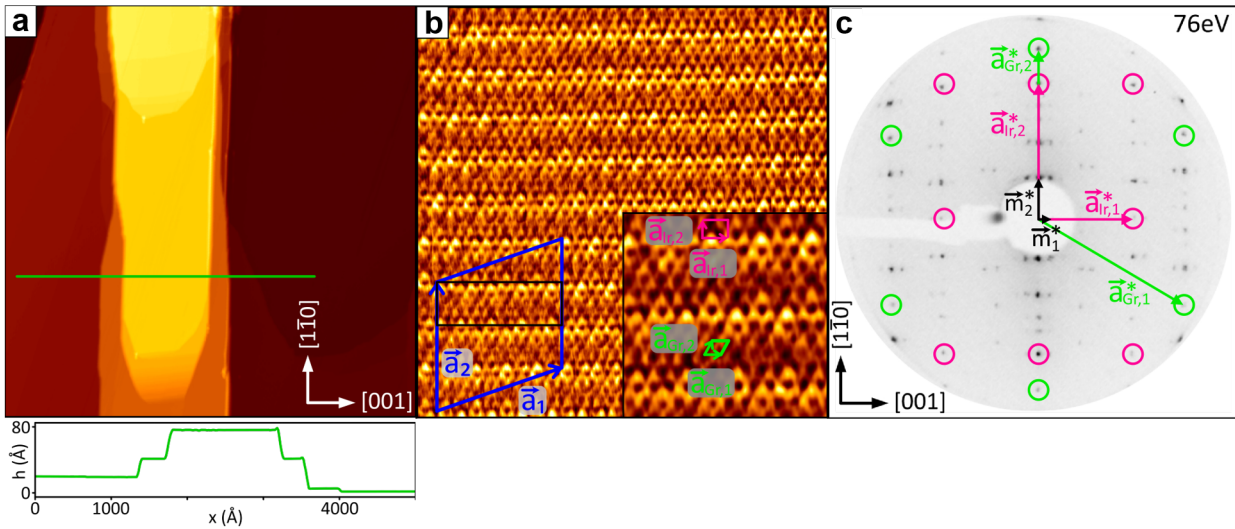


Figure **A-1**: **a** Large scale STM topograph on Gr/Ir(110) (700 nm \times 700 nm). The $[1\bar{1}0]$ and $[001]$ directions are indicated in the corner. The green line indicates the height profile displayed below. **b** Atomic resolution STM topograph (10 nm \times 10 nm). The commensurate superstructure cell is presented in blue, the moiré unit cell in black. The inset shows the Gr and Ir(110) unit cell (3 nm \times 3 nm). These indications are also represented in **c** LEED pattern of Gr/Ir(110) at 76 eV primary electron energy. Adapted from [37].

Fig. **A-2** represents the results of the DFT calculations. The charge-density difference (CDD) plots indicate the changes throughout the unit cell. Without going into detail, a strong interaction of the Gr with the Ir(110) is visible, at least for trough t_1 and the average.

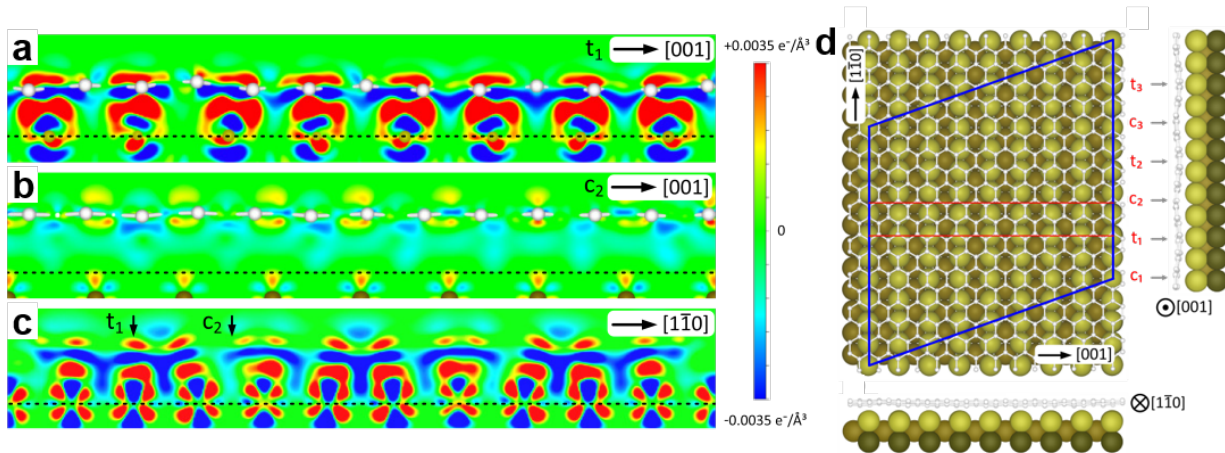


Figure **A-2**: **a**, **b** CDD plots in the **a** trough and **b** crest locations. **c** CCD average over the entire superstructure unit cell projected onto a plane along the $[1\bar{1}0]$ direction. **d** Ball model representation of the DFT supercell of Gr/Ir(110). The red lines indicate the charge density difference cuts. Adapted from [37].

t and c belongs to the troughs and crest of the wave pattern of Gr/Ir(110). This is in strong contrast to Gr/Ir(111). Having a detailed look at the average in Fig. **A-2 c**, additional charge is present just above the C atoms, which indicates a non-negligible sp^3 character of the bonding. The influence of this significant change in the carbon properties can be further analysed by electron photoemission experiments.

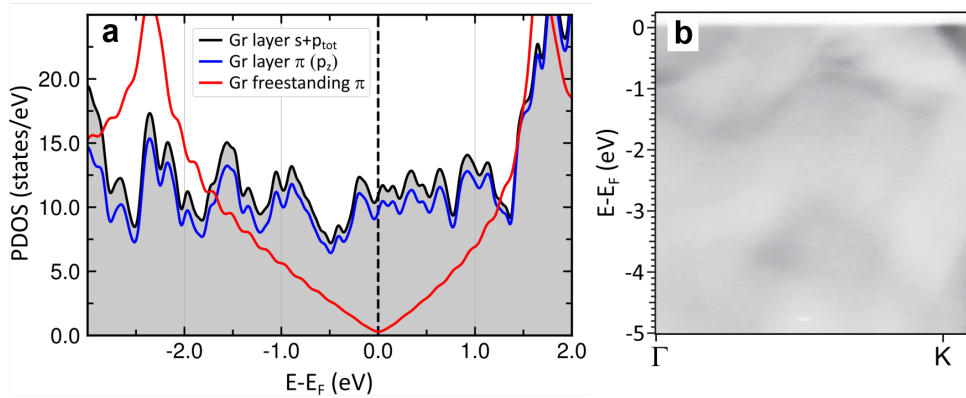


Figure **A-3**: **a** DFT partial Gr density of states (DOS) on Ir(110) (black line and grey shade). The blue line indicates the Gr partial DOS projected on the Gr π system and as a comparison the DOS of freestanding Gr. **b** Angle-resolved photoemission spectrum along $\Gamma - K$ of Gr/Ir(110). Adapted from [37].

The DFT-calculated DOS presented in **A-3 a** highlights the significant difference of the Gr partial DOS on Ir(110) to freestanding Gr, which can be explained by the strong interaction with the substrate. The ARPES measurement presented in Fig. **A-3 b** supports this interpretation, as there is no Dirac cone at the K point and no feature, that could be related to Gr π bands expected from the DFT calculation. Such a big change in the electronic properties may explain the changes, which have been observed in section 5.1.

Although the doping level of the Gr may not be well defined due to the strong changes in the electronic structure and the absence of a Dirac cone, XPS measurements could indicate additional charge on the C atoms due to a shift of the C K-edge.

The experimental overview XPS spectra presented in Fig. **A-4 a** display no significant difference between Gr/Ir(110) and Gr/Ir(111). The spectra of Gr/Ir(111) exhibits slightly sharper peaks, which is attributed to the increased measurement time, leading to a lower noise level. Only the detailed analysis of the C 1s peak, presented in Fig. **A-4 b** reveals differences between the two spectra. While the C 1s peak of Gr/Ir(111) lays at 284.1 eV, which is in line with the literature [159], the C 1s peak of Gr/Ir(110) is shifted by about 0.4 eV to 284.5 eV indicating a negative doping of the Gr. This is in line with the additional charge present in Fig. **A-2 c**, but is much smaller than the shift for Eu doping [45] and the graphene-covered surface alloys presented in chapter 4.

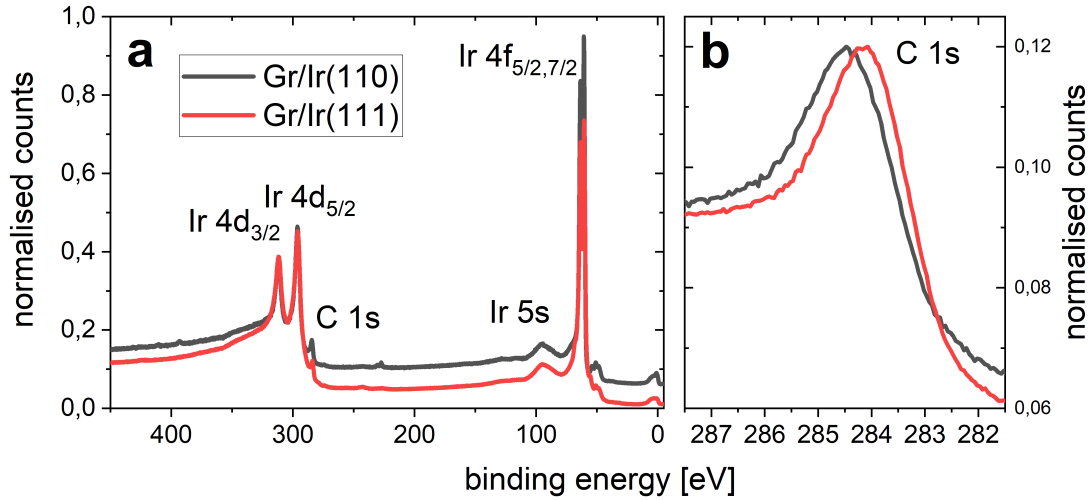


Figure A-4.: **a** Experimental XPS binding energies for Gr/Ir(110) and Gr/Ir(111) for $E_{\text{pass}} = 44$ eV and a step size of 0.25 eV. The peaks are assigned to their respective core levels and the Gr/Ir(110) spectra is shifted for better visibility. **b** Detailed scan of C 1s peak of Gr/Ir(110) and Gr/Ir(111) for $E_{\text{pass}} = 44$ eV and a step size of 0.1 eV.

Summarizing, one can state that Gr/Ir(110) is an interesting substrate with two-fold symmetry allowing global orientation of e.g. EuCot nanowires, but the strong interaction between the Ir(110) and Gr changes the Gr properties so significantly, that one may not view it as "quasi-freestanding" graphene anymore, which may explain the changes of the magnetic properties described in section 5.1.

A.2. X-ray Induced Oxidation of $4f$ Elements

The oxidation of $4f$ elements is a relevant issue in this work, as it always has to be taken into account when discussing the electronic and magnetic properties of structures including $4f$ elements. While all lanthanides favour the $3+$ oxidation state [107], Eu is also present in the $2+$ state, which is attributed to the half-filled $4f$ -shell of Eu^{2+} . This is also the reason, why Eu is more prone to oxidation than most of the other lanthanides. While regular UHV conditions are sufficient for most of the systems shown in this work, Eu based samples and TmCot nanowires, in which Tm is forced in the $2+$ state are critical concerning the UHV conditions. Especially the oxidation under permanent X-ray radiation is of special interest for us, as X-ray induced oxidation could be a relevant factor in our measurements [173].

To visualize and quantify the oxidation, we conducted XPS measurements on a simple model system of 4 ML Eu evaporated on a clean Ir(111) surface and watch the time evolution of the Eu $3d_{3/2,5/2}$ peak in a background pressure of $1 \cdot 10^{-9}$ mbar. The results of this measurement is presented in Fig. A-5.

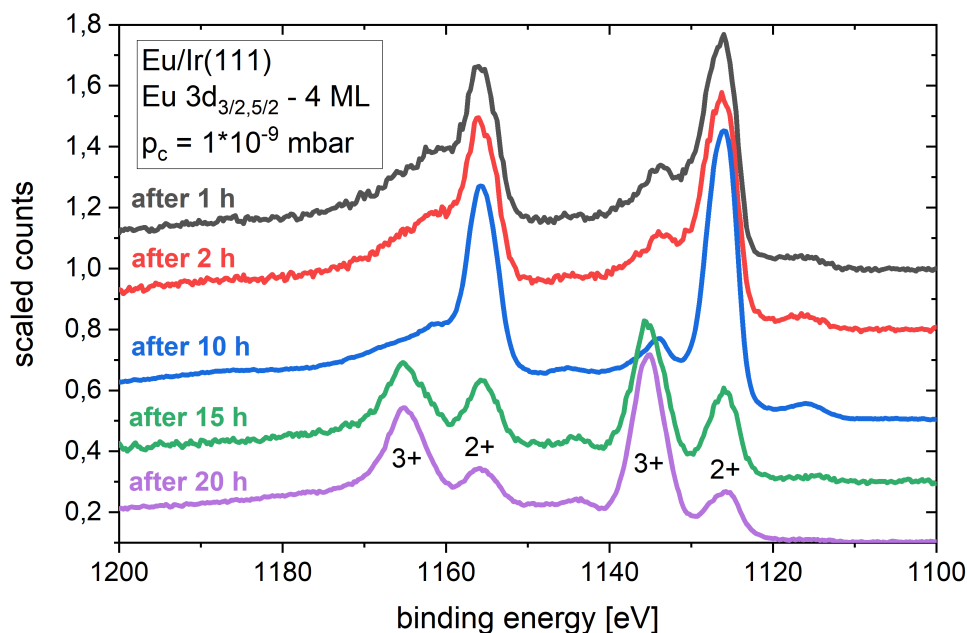


Figure A-5.: Time evolution of the Eu 3d_{3/2,5/2} XPS binding energies of 4 ML Eu on Ir(111) at a chamber background pressure of $1 \cdot 10^{-9}$ mbar. The edges and the oxidation states are indicated. $E_{\text{pass}} = 80$ eV and step size is 1 eV for 1h and 2 h, $E_{\text{pass}} = 44$ eV and step size is 0.25 eV for 10h, 15h, and 20h.

The measurements for one and two hours after the preparation show a clear 2+ state of the Eu on the sample. Even after 10 h of measurement, there is no significant 3+ contribution in the presented spectrum. The much better signal-to-noise ratio is contributed to the increased measurement time for this spectrum.

The situation changes for the measurement after 15 h. Here, a significant proportion of the spectra weight belongs to the 3+ state. After 20h, more than 75% of the spectral weight lies on the 3+ state, indicating a widely oxidised surface. The non-linear behaviour could be attributed to the properties of Eu. The first oxidation step of Eu is EuO, which still exhibits a 2+ oxidation state [174]. Further oxidation then leads to the energetically more favourable Eu₂O₃ exhibiting a 3+ oxidation state. Independent of this peculiarity of Eu, oxidation is a relevant factor for especially Eu-based samples. For other systems, like the Dy surface alloy, no change of the spectrum can be detected after even 24 h at similar conditions. It can be stated, that pressures below $1 \cdot 10^{-10}$ mbar allow measurements of up to 100 h without significant oxidation, which is more than enough for XPS and XANES measurements. These conditions have been present at all beamlines, besides VEKMAG, but the issues of the VEKMAG beamline have already been discussed in detail in section 5.3.

A.3. XPS Examination of the Chemical Structure of PEGMUA Coated Gold Nanoparticles

The work presented in this section is based on P. Hepperle, **A. Herman**, B. Khanbabaee, W. Baek, H. Nettelbeck, H. Rabus. XPS Examination of the Chemical Composition of PEGMUA-Coated Gold Nanoparticles [175]. I contributed the XPS measurements presented in this work.

Au nanoparticles (AuNPs) gathered wide interest as radiosensitizing agents in oncology, due to their physical properties and their biocompatibility [176, 177]. The local dose enhancement is based on their comparable greater interaction cross-section, compared to organic tissue [178]. In order to assure biocompatibility and prevent direct reactions with the metal, AuNPs are usually coated. In our case, the AuNPs are coated in PEGUMA. The thickness and structure of this coating are of high relevance, as it has to be thin enough, to allow electrons to pass through and thick enough to sufficiently cover the AuNPs. In order to study this system, we performed XPS measurements of spin-coated and drop-casted AuNPs samples and systematically sputtered the sample.

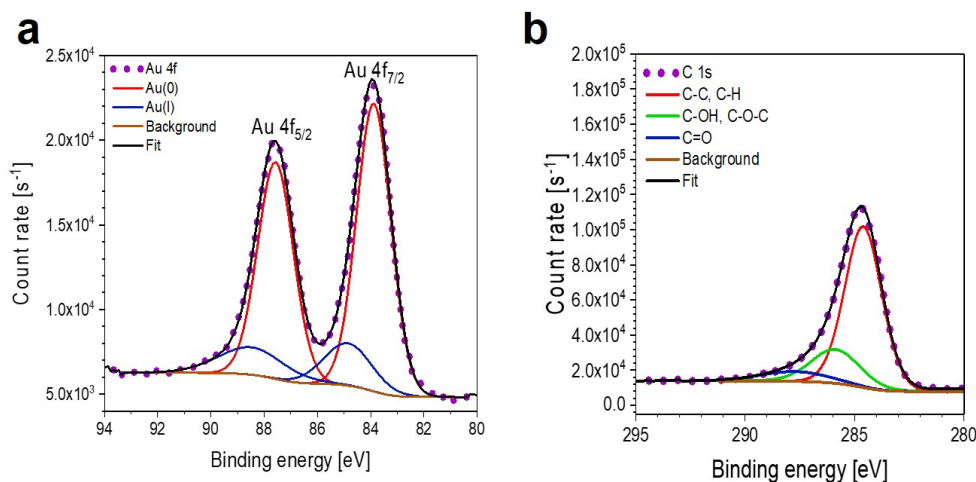


Figure A-6.: Experimental spectra and fitted components attributed to the **a** Au 4f core-level and **b** C 1s core level. Adapted from [175].

Fig. A-6 a presents the experimental spectra of the Au 4f_{7/2,5/2} edge as well as the fitted components. It is visible, that Au(0) is the most dominant peak, which is expected for metallic Au. The Au(I) contribution can be contributed to the Au surface atoms, which bind to the thiol-group of the coating molecule. The C 1s peak in Fig. A-6 b consist of various carbon contributions. The most dominant correlates to C-C bonding, whereas a significant amount of other bonds contribute to this spectrum. The overall distribution fits the expectations, besides the increased oxygen contribution. In order to get rid of

unfavourable oxygen contamination, the sample was sputtered by 3 keV Ar⁺. The resulting atomic percentages are presented in table **A-1**.

Peak	C 1s	O 1s	Au 4f	Cu 2p	S 2p
before spttering	86.1	12.4	1.1	0.3	0.1
after the 1st sputtering cycle (t=10 s)	93.3	3.3	3.0	0.3	
after the 2nd sputtering cycle (t =15 s)	94.4	2.3	3.0	0.3	
after the 3rd sputtering cycle (t = 60 s)	97.2	1.0	1.5	0.3	

Table **A-1**.: Atomic percentages of the main elements in the sample were determined from XPS peak areas. Adapted from [175].

While there is significant oxygen contamination in the initial sample, mild sputtering already reduces its proportion significantly. Further sputtering leads to a reduction of the coating molecules, which can be seen in the changes of the C 1s peak after sputtering [175], but does not affect the AuNPs yet. Increasing the fluence even further leads to sputtering of the AuNPs itself, as indicated by the decreasing Au proportion.

Another scope of the experiment was the evaluation of different deposition techniques, namely spin-coating and drop-casting. The analysis of the spectra revealed no differences in the chemical composition, but slightly lower oxygen contamination could be detected in the spin-coated sample.

In this work, we characterised AuNPs with PEGMUA coating for different deposition techniques. We could reveal the chemical composition as well as the oxygen contamination. By systematic sputtering, we were able to analyse the different contributions of this system.

A.4. Spin Crossover in a Cobalt Complex on Ag(111)

The work presented in this section is based on S. Johannsen, S. Ossinger, J. Grunwald, **A. Herman**, H. Wende, F. Tuzcek, M. Gruber, and R. Berndt. Spin Crossover in a Cobalt Complex on Ag(111) [179]. I contributed the XPS measurements to investigate the chemical composition of the molecules on the surface and their layer dependence.

Spin-crossover (SCO) compounds may change their spin state depending on parameters like temperature, light, and current. In the most studied Fe-based compounds, the low-spin (LS) to high-spin (HS) transition includes two electrons, whereas Co-based complexes just transfer a single electron from a t_{2g} to an e_g orbital. This results in much smaller changes in the structure. On metal surfaces, so far only Fe-based compounds have shown SCO properties. The interaction usually deviates from those of the bulk material.

In this work, the Co-based SCO compound $[\text{Co}(\text{H}_2\text{B}(\text{pz})(\text{pypz}))_2]$ has been synthesized and evaporated on an Ag(111) surface and its SCO properties have been investigated.

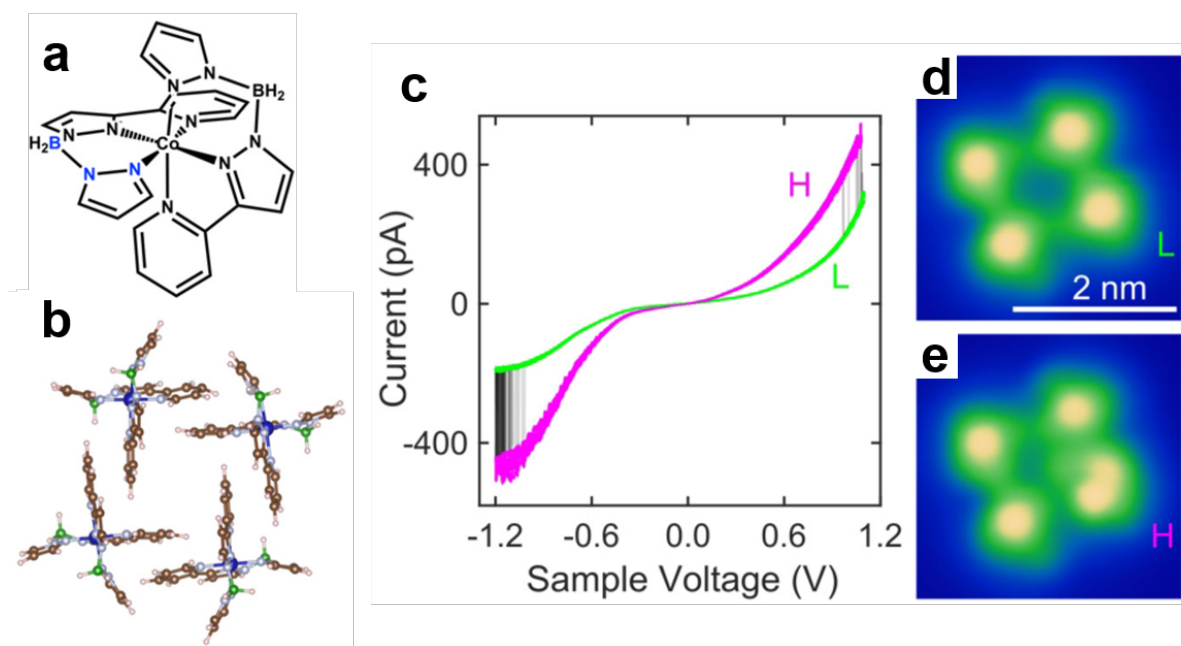


Figure A-7.: **a** Structure of $[\text{Co}(\text{H}_2\text{B}(\text{pz})(\text{pypz}))_2]$. **b** Ball model of tetramer predominantly forming at the surface. Co is indicated in blue, N in grey, C in brown, H in rose, and B in green. **c** Current-voltage data recorded from a molecule in a tetramer. The HS curve is given in purple, the LS in green. **d** STM topograph of a tetramer in the pristine LS state. **e** STM topograph of the tetramer after current injection to the molecule marked with L in **b**, leading to a HS state. Adapted from [179].

Fig. **A-7 a** displays the chemical structure of the SCO complex. On Ag(111), the preferably form tetramers, as indicated by the ball model in Fig. **A-7 b**. The current-voltage curve in Fig. **A-7 c** presents the switching behaviour. While there is no switching at small voltages, an abrupt transition between the two states is observed at $|V| > 1V$, which leads to a hysteresis. The effect of the current injection of the molecules is depicted in Fig. **A-7 d, e**. While the LS state ($S = 1/2$) is present in all four molecules in Fig. **A-7 d**, the situation changes after the current injection. As depicted in Fig. **A-7 e**, the spin of the affected molecule switches into the HS state ($S = 3/2$), which changes the appearance of the molecule in the STM topograph. This behaviour could be observed in Co compounds although the change in structure and therefore the expected lifetime of the excited states is very small. We attribute this to electron-induced spin state trapping (ELIESST), which is enabled by the tetramer formation.

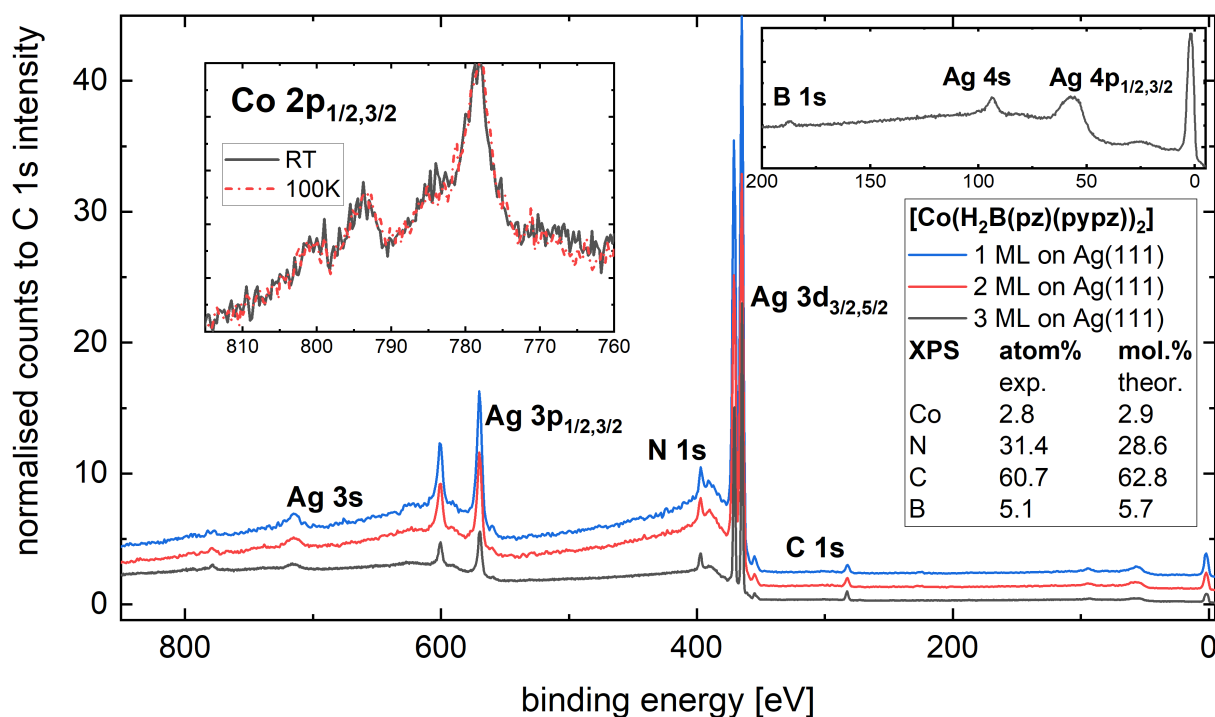


Figure **A-8.**: XPS overview spectra of $[\text{Co}(\text{H}_2\text{B}(\text{pz})(\text{pypz}))_2]$ on Ag(111) for three different thicknesses at room temperature. The relevant peaks are assigned. The left inset displays the $\text{Co } 2p_{1/2,3/2}$ edges of the 3 ML sample at room temperature and at 100 K. The zoom-in on the right shows the low energy area of 3 ML. The experimental atomic ratios are compared to the theoretical composition of the molecules. Provided for [179].

As discussed above, the substrate may have a strong influence on the spin-switching mechanism and the molecules. XPS measurements have been performed to answer two questions. Are the molecules present at the surface still intact and is there a layer dependence on the spin state of these molecules?

The spectra in Fig. **A-8** may answer those questions. First of all, the overview spectra do not show a significant change with the layer thickness, just the Ag edge intensity decreases with increasing layer thickness. The different signal to noise ratio is attributed to the different pass energy, 80 eV for 1 ML and 2 ML, 44 eV for 3 ML. Evaluating the atomic ratios shows, that the composition is as expected for the adsorption of $[\text{Co}(\text{H}_2\text{B}(\text{pz})(\text{pypz}))_2]$. There is neither a change of composition nor the electronic state for different layer thicknesses. The temperature dependence of the multilayer sample is presented in the inset. Within the error, there is no difference visible. These molecules are in the LS state for both temperatures, in line with the powder measurements.

Summarizing, these XPS measurements support the findings of the STM results and prove, that the temperature and thickness dependence is negligible for this system.

B. List of Beamtimes and Contributors

Beamtime/ Measurement	Proposal/ Main contributor	Assistance	Data evaluation	Year
SLS EuCot nanowires	H. Wende	S. Kraus, T. Michely, N. Rothenbach, K. Ollefs, J. Dreiser	A. Herman	04/2018
ARPES ASTRID EuCot	S. Kraus	A. Herman, M. Bianchi, R. Stan, A. Holt	S. Kraus	03/2019
BESSY TmCot	A. Herman	B. Eggert, T. Lojewski, L. Spieker, C. Luo, F. Radu, S. Thakur	A. Herman, L. Spieker	04/2019
SOLEIL TmCot	A. Herman	S. Kraus, L. Spieker, N. Rothenbach, F. Chouteikani	A. Herman, L. Spieker	07/2019
SLS Eu-TM-Cot surface alloys	A. Herman	S. Kraus, L. Spieker, T. Lojewski, J. Dreiser	A. Herman, L. Spieker	11/2019
BESSY Tb surface alloy	A. Herman	C. Pillich, N. Rothenbach, D. Günzing, C. Luo, F. Radu, S. Thakur	A. Herman	01/2020
XPS Au nanoparticles	P. Hepperle*	A. Herman*	P. Hepperle	05/2020
STM Köln Dy surface alloy	A. Herman*	S. Kraus*	A. Herman	07/2020
XPS EuCot BaCot	A. Herman*	S. Kraus*	S. Kraus, A. Herman	09/2020
BESSY TmCot Ho surface alloy	A. Herman	C. Pillich, J. Lill, D. Günzing, K. Chen, F. Radu, S. Thakur	A. Herman	10/2020
ALS Re-i-MAX	D. Günzing		A. Herman, D. Günzing	10/2021
XPS Co Spin crossover	A. Herman		A. Herman	12/2021
all other measurements	A. Herman	U. v. Hörsten	A. Herman	2018-22

* equal contribution

C. List of Publications

- **A. Herman**, S. Kraus, S. Tsukamoto, L. Spieker, V. Caciuc, T. Lojewski, D. Günzing, J. Dreiser, B. Delley, K. Ollefs, T. Michely, N. Atodiresei, H. Wende. Tailoring magnetic anisotropy by graphene-induced selective skyhook effect on 4f-metals [17]
- **A. Herman**, S. Kraus, S. Tsukamoto, L. Spieker, V. Caciuc, T. Lojewski, C. Pillich, D. Günzing, J. Dreiser, B. Delley, S. Thakur, C. Luo, K. Chen, F. Radu, K. Ollefs, T. Michely, N. Atodiresei, H. Wende. Tailoring the magnetic anisotropy of 4f-surface alloys by graphene adsorption – a systematic study [74] (in preparation)
- S. Kraus, **A. Herman**, F. Huttmann, M. Bianchi, R. Stan, A. Holt, S. Tsukamoto, J. Dreiser, K. Bischof, H. Wende, P. Hofmann, N. Atodiresei, and T. Michely. Uniaxially aligned 1D sandwich-molecular wires: electronic structure and magnetism [163]
- S. Kraus, **A. Herman**, F. Huttmann, C. Krämer, S. Tsukamoto, H. Wende, N. Atodiresei, and T. Michely. Selecting the Reaction Path in On-Surface Synthesis Through the Electron Chemical Potential in Graphene [164]
- S. Kraus, F. Huttmann, J. Fischer, T. Knispel, K. Bischof, **A. Herman**, M. Bianchi, R. Stan, A. Holt, V. Caciuc, S. Tsukamoto, H. Wende, P. Hofmann, N. Atodiresei, and T. Michely. Single-crystal graphene on Ir(110) [37]
- P. Hepperle, **A. Herman**, B. Khanbabaee, W. Baek, H. Nettelbeck, H. Rabus. XPS Examination of the Chemical Composition of PEGMUA-Coated Gold Nanoparticles [175]
- S. Johannsen, S. Ossinger, J. Grunwald, **A. Herman**, H. Wende, F. Tuczec, M. Gruber, and R. Berndt. Spin Crossover in a Cobalt Complex on Ag(111) [179]

D. Conference Contributions

- CENIDE Jahresfeier, Essen (2018), poster
- DPG Spring Meeting (SKM), Regensburg (2019), poster
- Psi-k workshop - Theory meets experiment in low-dimensional structures with correlated electrons, Prague (2019), talk
- German-Russian Travelling Seminar, Listwjanika (2019), talk
- CENIDE Jahresfeier, hybrid (2020), poster
- DPG spring meeting (SKM), online (2021), poster
- 3rd European Conference on Molecular Spintronics, Dortmund (2022), talk
- 5th European Workshop on Epitaxial Graphene and 2D Materials, Davos (2022), poster

E. Danksagung

First, I want to thank Heiko for giving me the possibility to write this thesis and for supervising my project. I would like to thank you, especially for the opportunity to freely develop my ideas and projects in terms of time and money.

Secondly, I want to thank Thomas for being my co-advisor and supporting me with ideas and great scientific discussions, leading to the solutions to many problems.

Furthermore, I would like to thank Stefan for the constant support and communication, working together to reveal the physics behind our investigated systems.

I would like to thank Nicolae for the support and explanations of the DFT calculation, although communication has been difficult some times.

I would like to especially thank Christiane and Uli, for doing an excellent job, and providing any help needed concerning paperwork and technical issues.

I also would like to thank all co-workers, collaborators, and beamline scientists mentioned in section B, without whom this work would not have been possible. I thank all the group members of the AG Wende and especially Lea, for the support of the data evaluation and Damian, Tobias, Johanna, Simon, and Cynthia for general support, providing data evaluation scripts, and proofreading my thesis.

In the end, I would like to thank my (soon) wife, family, and friends for keeping me on track and supporting me during this time.

I acknowledge financial support by DFG through the project WE 2623/17-1, and the scholarships acquired during this work by the HZB, SOLEIL, PSI, HERAEUS, The Czech Academy of Sciences, Aarhus University, and the German-Russian Travelling Seminar (BMBF, MSU, UFU, FAU, Uni Bayreuth).

F. Erlahrung gema Promotionsordnung

Die Gelegenheit zum vorliegenden Promotionsverfahren ist mir nicht kommerziell vermittelt worden. Insbesondere habe ich keine Organisation eingeschaltet, die gegen Entgelt Betreuerinnen und Betreuer fur die Anfertigung von Dissertationen sucht oder die mir obliegenden Pflichten hinsichtlich der Prufungsleistungen fur mich ganz oder teilweise erledigt. Hilfe Dritter wurde bis jetzt und wird auch kunftig nur in wissenschaftlich vertretbarem und prufungsrechtlich zulassigem Ausma in Anspruch genommen. Mir ist bekannt, dass Unwahrheiten hinsichtlich der vorstehenden Erklahrung die Zulassung zur Promotion ausschlieen bzw. spater zum Verfahrensabbruch oder zur Rucknahme des Titels fuhren konnen. Mit dieser Arbeit strebe ich die Erlangung des akademischen Grades Doktor der Naturwissenschaften (Dr. rer. nat.) an.

Alexander Herman

Bibliography

- [1] Skokov, K. & Gutfleisch, O. Heavy rare earth free, free rare earth and rare earth free magnets - Vision and reality. *Scripta Materialia* **154**, 289–294 (2018). URL <https://linkinghub.elsevier.com/retrieve/pii/S1359646218300599>.
- [2] Coey, J. Perspective and Prospects for Rare Earth Permanent Magnets. *Engineering* **6**, 119–131 (2020). URL <https://doi.org/10.1016/j.eng.2018.11.034>.
- [3] Feltham, H. L. & Brooker, S. Review of purely 4f and mixed-metal and 4f single-molecule magnets containing only one lanthanide ion. *Coordination Chemistry Reviews* **276**, 1–33 (2014). URL <https://linkinghub.elsevier.com/retrieve/pii/S0010854514001465>.
- [4] Tang, H., Mamakhel, M. A. H. & Christensen, M. Enhancing the coercivity of SmCo 5 magnet through particle size control. *Journal of Materials Chemistry C* **8**, 2109–2116 (2020). URL <http://xlink.rsc.org/?DOI=C9TC06137A>.
- [5] Donati, F. *et al.* Magnetic remanence in single atoms. *Science* **352**, 318–321 (2016). URL <https://www.science.org/doi/10.1126/science.aad9898>.
- [6] Zutic, I., Fabian, J. & Sarma, S. D. Spintronics: Fundamentals and applications. *International Journal of Medical Sciences* **9**, 492–497 (2004). URL <http://dx.doi.org/10.1103/RevModPhys.76.323.0405528>.
- [7] Woodruff, D. N., Winpenny, R. E. P. & Layfield, R. A. Lanthanide Single-Molecule Magnets. *Chemical Reviews* **113**, 5110–5148 (2013). URL <https://pubs.acs.org/doi/10.1021/cr400018q>.
- [8] Wäckerlin, C. *et al.* Giant Hysteresis of Single-Molecule Magnets Adsorbed on a Nonmagnetic Insulator. *Advanced Materials* **28**, 5195–5199 (2016). URL <https://onlinelibrary.wiley.com/doi/10.1002/adma.201506305>.
- [9] Hosoya, N. *et al.* Lanthanide Organometallic Sandwich Nanowires: Formation Mechanism. *The Journal of Physical Chemistry A* **109**, 9–12 (2005). URL <http://pubs.acs.org/doi/abs/10.1021/jp0452103>.

- [10] Xu, K., Cao, P. & Heath, J. R. Scanning Tunneling Microscopy Characterization of the Electrical Properties of Wrinkles in Exfoliated Graphene Monolayers. *Nano Letters* **9**, 4446–4451 (2009). URL <https://pubs.acs.org/doi/10.1021/nl902729p>.
- [11] Urdampilleta, M., Klyatskaya, S., Cleuziou, J.-P., Ruben, M. & Wernsdorfer, W. Supramolecular spin valves. *Nature Materials* **10**, 502–506 (2011). URL <http://www.nature.com/articles/nmat3050>.
- [12] Baltic, R. *et al.* Superlattice of Single Atom Magnets on Graphene. *Nano Letters* **16**, 7610–7615 (2016). URL <https://pubs.acs.org/doi/10.1021/acs.nanolett.6b03543>.
- [13] Campbell, V. E. *et al.* Engineering the magnetic coupling and anisotropy at the molecule–magnetic surface interface in molecular spintronic devices. *Nature Communications* **7**, 13646 (2016). URL <http://www.nature.com/articles/ncomms13646>.
- [14] Wende, H. *et al.* Substrate-induced magnetic ordering and switching of iron porphyrin molecules. *Nature Materials* **6**, 516–520 (2007). URL <http://www.nature.com/articles/nmat1932>.
- [15] Donati, F. *et al.* Correlation between Electronic Configuration and Magnetic Stability in Dysprosium Single Atom Magnets. *Nano Letters* **21**, 8266–8273 (2021). URL <https://pubs.acs.org/doi/10.1021/acs.nanolett.1c02744>.
- [16] Uldry, A., Vernay, F. & Delley, B. Systematic computation of crystal-field multiplets for x-ray core spectroscopies. *Physical Review B* **85**, 125133 (2012). URL <https://link.aps.org/doi/10.1103/PhysRevB.85.125133>.
- [17] Herman, A. *et al.* Tailoring magnetic anisotropy by graphene-induced selective skyhook effect on 4f-metals. *Nanoscale* **14**, 7682–7691 (2022). URL <http://xlink.rsc.org/?DOI=D2NR01458K>.
- [18] Huttmann, F. *et al.* Europium Cyclooctatetraene Nanowire Carpets: A Low-Dimensional, Organometallic, and Ferromagnetic Insulator. *The Journal of Physical Chemistry Letters* **10**, 911–917 (2019). URL <http://pubs.acs.org/doi/10.1021/acs.jpcllett.8b03711>.
- [19] Novoselov, K. S. *et al.* Electric Field Effect in Atomically Thin Carbon Films. *Science* **306**, 666–669 (2004). URL <https://www.science.org/doi/10.1126/science.1102896>.
- [20] Novoselov, K. S. *et al.* Two-dimensional gas of massless Dirac fermions in graphene. *Nature* **438**, 197–200 (2005). URL <http://www.nature.com/articles/nature04233>.

- [21] Class for Physics of the Royal Swedish Academy of Sciences. Scientific Background on the Nobel Prize in Physics 2010 GRAPHENE. *Graphene* **50005**, 0–10 (2010). URL <https://www.nobelprize.org/uploads/2018/06/advanced-physicsprize2010.pdf>.
- [22] Castro Neto, A. H., Guinea, F., Peres, N. M. R., Novoselov, K. S. & Geim, A. K. The electronic properties of graphene. *Reviews of Modern Physics* **81**, 109–162 (2009). URL <https://link.aps.org/doi/10.1103/RevModPhys.81.109>. 0709.1163.
- [23] Zhu, Y. *et al.* Graphene and Graphene Oxide: Synthesis, Properties, and Applications. *Advanced Materials* **22**, 3906–3924 (2010). URL <https://onlinelibrary.wiley.com/doi/10.1002/adma.201001068>.
- [24] Batzill, M. The surface science of graphene: Metal interfaces, CVD synthesis, nanoribbons, chemical modifications, and defects. *Surface Science Reports* **67**, 83–115 (2012). URL <http://dx.doi.org/10.1016/j.surfrep.2011.12.001>.
- [25] Coraux, J., N'Diaye, A. T., Busse, C. & Michely, T. Structural Coherency of Graphene on Ir(111). *Nano Letters* **8**, 565–570 (2008). URL <https://pubs.acs.org/doi/10.1021/nl0728874>.
- [26] Pletikosić, I. *et al.* Dirac Cones and Minigaps for Graphene on Ir(111). *Physical Review Letters* **102**, 056808 (2009). URL <https://link.aps.org/doi/10.1103/PhysRevLett.102.056808>. 0807.2770.
- [27] T N'Diaye, A. *et al.* Growth of graphene on Ir(111). *New Journal of Physics* **11**, 023006 (2009). URL <https://iopscience.iop.org/article/10.1088/1367-2630/11/2/023006>.
- [28] Gao, L., Guest, J. R. & Guisinger, N. P. Epitaxial Graphene on Cu(111). *Nano Letters* **10**, 3512–3516 (2010). URL <https://pubs.acs.org/doi/10.1021/nl1016706>.
- [29] Land, T. A., Michely, T., Behm, R. J., Hemminger, J. C. & Comsa, G. Direct observation of surface reactions by scanning tunneling microscopy: Ethylene→ethylidyne→carbon particles→graphite on Pt(111). *The Journal of Chemical Physics* **97**, 6774–6783 (1992). URL <http://aip.scitation.org/doi/10.1063/1.463655>.
- [30] Marchini, S., Günther, S. & Wintterlin, J. Scanning tunneling microscopy of graphene on Ru(0001). *Physical Review B* **76**, 075429 (2007). URL <https://link.aps.org/doi/10.1103/PhysRevB.76.075429>.
- [31] Martoccia, D. *et al.* Graphene on Ru(0001): a corrugated and chiral structure. *New Journal of Physics* **12**, 043028 (2010). URL <https://iopscience.iop.org/article/10.1088/1367-2630/12/4/043028>.

- [32] N'Diaye, A. T., Coraux, J., Plasa, T. N., Busse, C. & Michely, T. Structure of epitaxial graphene on Ir(111). *New Journal of Physics* **10**, 043033 (2008). URL <https://iopscience.iop.org/article/10.1088/1367-2630/10/4/043033>.
- [33] Busse, C. *et al.* Graphene on Ir(111): Physisorption with Chemical Modulation. *Physical Review Letters* **107**, 036101 (2011). URL <https://link.aps.org/doi/10.1103/PhysRevLett.107.036101>. 1105.3883.
- [34] Mittendorfer, F. *et al.* Graphene on Ni(111): Strong interaction and weak adsorption. *Physical Review B* **84**, 201401 (2011). URL <https://link.aps.org/doi/10.1103/PhysRevB.84.201401>.
- [35] Wang, X.-L., Dou, S. X. & Zhang, C. Zero-gap materials for future spintronics, electronics and optics. *NPG Asia Materials* **2**, 31–38 (2010). URL <http://www.nature.com/articles/am201027>.
- [36] Voloshina, E. & Dedkov, Y. Graphene on metallic surfaces: problems and perspectives. *Physical Chemistry Chemical Physics* **14**, 13502 (2012). URL <http://xlink.rsc.org/?DOI=c2cp42171b>. 1207.6335.
- [37] Kraus, S. *et al.* Single-crystal graphene on Ir(110). *Physical Review B* **105**, 165405 (2022). URL <https://link.aps.org/doi/10.1103/PhysRevB.105.165405>. 2109.04198.
- [38] Larciprete, R. *et al.* Oxygen Switching of the Epitaxial Graphene–Metal Interaction. *ACS Nano* **6**, 9551–9558 (2012). URL <https://pubs.acs.org/doi/10.1021/nn302729j>.
- [39] Herbig, C. *et al.* Mechanical exfoliation of epitaxial graphene on Ir(111) enabled by Br 2 intercalation. *Journal of Physics: Condensed Matter* **24**, 314208 (2012). URL <https://iopscience.iop.org/article/10.1088/0953-8984/24/31/314208>.
- [40] Leicht, P. *et al.* In Situ Fabrication Of Quasi-Free-Standing Epitaxial Graphene Nanoflakes On Gold. *ACS Nano* **8**, 3735–3742 (2014). URL <https://pubs.acs.org/doi/10.1021/nm500396c>.
- [41] Huttmann, F. *et al.* Magnetism in a graphene-4f-3d hybrid system. *Physical Review B* **95**, 075427 (2017). URL <https://link.aps.org/doi/10.1103/PhysRevB.95.075427>.
- [42] Decker, R. *et al.* Atomic-scale magnetism of cobalt-intercalated graphene. *Physical Review B* **87**, 041403 (2013). URL <https://link.aps.org/doi/10.1103/PhysRevB.87.041403>.

- [43] Vita, H. *et al.* Electronic structure and magnetic properties of cobalt intercalated in graphene on Ir(111). *Physical Review B* **90**, 165432 (2014). URL <https://link.aps.org/doi/10.1103/PhysRevB.90.165432>.
- [44] Schumacher, S., Förster, D. F., Rösner, M., Wehling, T. O. & Michely, T. Strain in Epitaxial Graphene Visualized by Intercalation. *Physical Review Letters* **110**, 086111 (2013). URL <https://link.aps.org/doi/10.1103/PhysRevLett.110.086111>.
- [45] Schumacher, S. *et al.* Europium underneath graphene on Ir(111): Intercalation mechanism, magnetism, and band structure. *Physical Review B* **90**, 235437 (2014). URL <https://link.aps.org/doi/10.1103/PhysRevB.90.235437>. 1409.4272.
- [46] Kralj, M. *et al.* Graphene on Ir(111) characterized by angle-resolved photoemission. *Physical Review B* **84**, 075427 (2011). URL <https://link.aps.org/doi/10.1103/PhysRevB.84.075427>.
- [47] Schröder, U. A. *et al.* Core level shifts of intercalated graphene. *2D Materials* **4**, 015013 (2016). URL <https://iopscience.iop.org/article/10.1088/2053-1583/4/1/015013>.
- [48] Pervan, P. *et al.* Li adsorption versus graphene intercalation on Ir(111): From quenching to restoration of the Ir surface state. *Physical Review B* **92**, 245415 (2015). URL <https://link.aps.org/doi/10.1103/PhysRevB.92.245415>.
- [49] Liebscher, W. & Fluck, E. *Die systematische Nomenklatur der anorganischen Chemie*, vol. 507 of *Lecture Notes in Economics and Mathematical Systems* (Springer Berlin Heidelberg, Berlin, Heidelberg, 1999). URL <http://link.springer.com/10.1007/978-3-642-56680-6>.
- [50] Shanavas, K. V., Popović, Z. S. & Satpathy, S. Theoretical model for Rashba spin-orbit interaction in d electrons. *Physical Review B* **90**, 165108 (2014). URL <https://link.aps.org/doi/10.1103/PhysRevB.90.165108>.
- [51] Russell, H. N. & Saunders, F. A. New Regularities in the Spectra of the Alkaline Earths. *The Astrophysical Journal* **61**, 38 (1925). URL <http://adsabs.harvard.edu/doi/10.1086/142872>.
- [52] Tiesinga, E., Mohr, P. J., Newell, D. B. & Taylor, B. N. CODATA recommended values of the fundamental physical constants: 2018. *Reviews of Modern Physics* **93**, 025010 (2021). URL <https://link.aps.org/doi/10.1103/RevModPhys.93.025010>.
- [53] Landé, A. Über den anomalen Zeemaneffekt (Teil I). *Zeitschrift für Physik* **5**, 231–241 (1921). URL <http://link.springer.com/10.1007/BF01335014>.

- [54] Skomski, R. *Simple Models of Magnetism* (Oxford University Press, USA, 2008).
- [55] Rinehart, J. D. & Long, J. R. Exploiting single-ion anisotropy in the design of f-element single-molecule magnets. *Chemical Science* **2**, 2078 (2011). URL <http://xlink.rsc.org/?DOI=c1sc00513h>.
- [56] Ishikawa, N., Sugita, M., Ishikawa, T., Koshihara, S.-y. & Kaizu, Y. Lanthanide Double-Decker Complexes Functioning as Magnets at the Single-Molecular Level. *Journal of the American Chemical Society* **125**, 8694–8695 (2003). URL <https://pubs.acs.org/doi/10.1021/ja029629n>.
- [57] Brown, S. D., Strange, P., Bouchenoire, L. & Thompson, P. B. J. 4f/5d hybridization in the heavy rare earth elements Er and Tm. *Physical Review B* **87**, 165111 (2013). URL <https://link.aps.org/doi/10.1103/PhysRevB.87.165111>.
- [58] Zhang, L. *et al.* Strong-correlated behavior of 4f electrons and 4f5d hybridization in PrO₂. *Scientific Reports* **8**, 15995 (2018). URL <http://www.nature.com/articles/s41598-018-34336-4>.
- [59] Guo, F.-S. *et al.* Magnetic hysteresis up to 80 kelvin in a dysprosium metallocene single-molecule magnet. *Science* **362**, 1400–1403 (2018). URL <https://www.science.org/doi/10.1126/science.aav0652>.
- [60] Gao, C. *et al.* Observation of the asphericity of 4f-electron density and its relation to the magnetic anisotropy axis in single-molecule magnets. *Nature Chemistry* **12**, 213–219 (2020). URL <http://dx.doi.org/10.1038/s41557-019-0387-6>.
- [61] Briganti, M. *et al.* Magnetic Anisotropy Trends along a Full 4f-Series: The f_n + 7 Effect. *Journal of the American Chemical Society* **143**, 8108–8115 (2021). URL <https://pubs.acs.org/doi/10.1021/jacs.1c02502>.
- [62] Ormaza, M. *et al.* High Temperature Ferromagnetism in a GdAg₂ Monolayer. *Nano Letters* **16**, 4230–4235 (2016). URL <https://pubs.acs.org/doi/10.1021/acs.nanolett.6b01197>.
- [63] Correa, A., Xu, B., Verstraete, M. J. & Vitali, L. Strain-induced effects in the electronic and spin properties of a monolayer of ferromagnetic GdAg₂. *Nanoscale* **8**, 19148–19153 (2016). URL <http://xlink.rsc.org/?DOI=C6NR06398E>.
- [64] Seidel, J. *et al.* Exchange Splitting of a Hybrid Surface State and Ferromagnetic Order in a 2D Surface Alloy. *ArXiv.1096.03780* **1** (2019). URL <http://arxiv.org/abs/1906.03780>. 1906.03780.

- [65] Corso, M., Fernández, L., Schiller, F. & Ortega, J. E. Au(111)-Based Nanotemplates by Gd Alloying. *ACS Nano* **4**, 1603–1611 (2010). URL <https://pubs.acs.org/doi/10.1021/nn901345s>.
- [66] Ormaza, M. *et al.* LaAu₂ and CeAu₂ surface intermetallic compounds grown by high-temperature deposition on Au(111). *Physical Review B* **88**, 125405 (2013). URL <https://link.aps.org/doi/10.1103/PhysRevB.88.125405>.
- [67] Que, Y. *et al.* Two-Dimensional Rare Earth–Gold Intermetallic Compounds on Au(111) by Surface Alloying. *The Journal of Physical Chemistry Letters* **11**, 4107–4112 (2020). URL <https://pubs.acs.org/doi/10.1021/acs.jpcllett.0c00981>.
- [68] Fernandez, L. *et al.* Influence of 4f filling on electronic and magnetic properties of rare earth-Au surface compounds. *Nanoscale* **12**, 22258–22267 (2020). URL <http://xlink.rsc.org/?DOI=D0NR04964F>.
- [69] Xu, C. *et al.* A two-dimensional ErCu₂ intermetallic compound on Cu(111) with moiré-pattern-modulated electronic structures. *Physical Chemistry Chemical Physics* **22**, 1693–1700 (2020). URL <http://xlink.rsc.org/?DOI=C9CP05585A>.
- [70] Mousavion, S. *et al.* Atomic and mesoscopic structure of Dy-based surface alloys on noble metals. *arXiv.2111.11877* (2021). URL <http://arxiv.org/abs/2111.11877>.
- [71] Przychodnia, M. *et al.* Controlled growth of Gd-Pt surface alloys on Pt(111). *Physical Review B* **105**, 035416 (2022). URL <https://link.aps.org/doi/10.1103/PhysRevB.105.035416>.
- [72] Mitryaev, A. A., Naumovets, A. G. & Fedorus, A. G. Surface alloy formation and two-dimensional vitrification in adsorbed monolayers on Molybdenum (112) surfaces. *Low Temperature Physics* **36**, 677–681 (2010). URL <http://aip.scitation.org/doi/10.1063/1.3490832>.
- [73] Kraus, S. *Nanostructures of Cyclooctatetraene with Rare Earth Metals : Growth and Magnetism*. Master thesis, Universität zu Köln (2017).
- [74] Herman, A. *et al.* Tailoring the magnetic anisotropy of 4f-surface alloys by graphene adsorption – a systematic study. *in preparation* (2022).
- [75] Que, Y. *et al.* On-Surface Synthesis of Graphene Nanoribbons on Two-Dimensional Rare Earth–Gold Intermetallic Compounds. *The Journal of Physical Chemistry Letters* **11**, 5044–5050 (2020). URL <https://pubs.acs.org/doi/10.1021/acs.jpcllett.0c01398>.

- [76] Ishikawa, N., Sugita, M., Ishikawa, T., Koshihara, S.-y. & Kaizu, Y. Lanthanide Double-Decker Complexes Functioning as Magnets at the Single-Molecular Level. *Journal of the American Chemical Society* **125**, 8694–8695 (2003). URL <https://pubs.acs.org/doi/10.1021/ja029629n>.
- [77] Shiddiq, M. *et al.* Enhancing coherence in molecular spin qubits via atomic clock transitions. *Nature* **531**, 348–351 (2016). URL <http://www.nature.com/articles/nature16984>.
- [78] Thiele, S. *et al.* Electrically driven nuclear spin resonance in single-molecule magnets. *Science* **344**, 1135–1138 (2014). URL <https://www.science.org/doi/10.1126/science.1249802>.
- [79] Němec, P., Fiebig, M., Kampfrath, T. & Kimel, A. V. Antiferromagnetic optospintronics. *Nature Physics* **14**, 229–241 (2018). URL <http://www.nature.com/articles/s41567-018-0051-x>.
- [80] Manipatruni, S. *et al.* Scalable energy-efficient magnetoelectric spin–orbit logic. *Nature* **565**, 35–42 (2019). URL <http://www.nature.com/articles/s41586-018-0770-2>.
- [81] Sessoli, R., Gatteschi, D., Caneschi, A. & Novak, M. A. Magnetic bistability in a metal-ion cluster. *Nature* **365**, 141–143 (1993). URL <http://www.nature.com/articles/365141a0>.
- [82] Goodwin, C. A. P., Ortu, F., Reta, D., Chilton, N. F. & Mills, D. P. Molecular magnetic hysteresis at 60 kelvin in dysprosocenium. *Nature* **548**, 439–442 (2017). URL <http://dx.doi.org/10.1038/nature23447>.
- [83] Gatteschi, D. & Sessoli, R. Quantum Tunneling of Magnetization and Related Phenomena in Molecular Materials. *Angewandte Chemie International Edition* **42**, 268–297 (2003). URL <https://onlinelibrary.wiley.com/doi/10.1002/anie.200390099>.
- [84] Wäckerlin, C. *et al.* Giant Hysteresis of Single-Molecule Magnets Adsorbed on a Nonmagnetic Insulator. *Advanced Materials* **28**, 5195–5199 (2016). URL <https://onlinelibrary.wiley.com/doi/10.1002/adma.201506305>.
- [85] Paschke, F. *et al.* Exceptionally High Blocking Temperature of 17 K in a Surface-Supported Molecular Magnet. *Advanced Materials* **33**, 2102844 (2021). URL <https://onlinelibrary.wiley.com/doi/10.1002/adma.202102844>.
- [86] Stepanow, S. *et al.* Spin and Orbital Magnetic Moment Anisotropies of Monodispersed Bis(Phthalocyaninato)Terbium on a Copper Surface. *Journal of the American Chemical Society* **132**, 11900–11901 (2010). URL <https://pubs.acs.org/doi/10.1021/ja105124r>.

- [87] Chen, C.-H. *et al.* Magnetic hysteresis in self-assembled monolayers of Dy-fullerene single molecule magnets on gold. *Nanoscale* **10**, 11287–11292 (2018). URL <http://xlink.rsc.org/?DOI=C8NR00511G>.
- [88] Rinehart, J. D., Fang, M., Evans, W. J. & Long, J. R. A N 2 3– Radical-Bridged Terbium Complex Exhibiting Magnetic Hysteresis at 14 K. *Journal of the American Chemical Society* **133**, 14236–14239 (2011). URL <https://pubs.acs.org/doi/10.1021/ja206286h>.
- [89] Liu, F. *et al.* Single molecule magnet with an unpaired electron trapped between two lanthanide ions inside a fullerene. *Nature Communications* **8**, 16098 (2017). URL <http://www.nature.com/articles/ncomms16098>.
- [90] Hübner, C., Baxevanis, B., Khajetoorians, A. A. & Pfannkuche, D. Symmetry effects on the spin switching of adatoms. *Physical Review B* **90**, 155134 (2014). URL <https://link.aps.org/doi/10.1103/PhysRevB.90.155134>. 1409.6541.
- [91] Urdampilleta, M., Klayatskaya, S., Ruben, M. & Wernsdorfer, W. Magnetic Interaction Between a Radical Spin and a Single-Molecule Magnet in a Molecular Spin-Valve. *ACS Nano* **9**, 4458–4464 (2015). URL <https://pubs.acs.org/doi/10.1021/acsnano.5b01056>.
- [92] Wang, J., Acioli, P. H. & Jellinek, J. Structure and Magnetism of V n Bz n +1 Sandwich Clusters. *Journal of the American Chemical Society* **127**, 2812–2813 (2005). URL <https://pubs.acs.org/doi/10.1021/ja043807q>.
- [93] Maslyuk, V. V. *et al.* Organometallic Benzene-Vanadium Wire: A One-Dimensional Half-Metallic Ferromagnet. *Physical Review Letters* **97**, 097201 (2006). URL <https://link.aps.org/doi/10.1103/PhysRevLett.97.097201>. 0510144.
- [94] Mokrousov, Y., Atodiresei, N., Bihlmayer, G. & Blügel, S. Magnetic anisotropy energies of metal–benzene sandwiches. *International Journal of Quantum Chemistry* **106**, 3208–3213 (2006). URL <https://onlinelibrary.wiley.com/doi/10.1002/qua.21139>.
- [95] Xiang, H., Yang, J., Hou, J. G. & Zhu, Q. One-Dimensional Transition Metal–Benzene Sandwich Polymers: Possible Ideal Conductors for Spin Transport. *Journal of the American Chemical Society* **128**, 2310–2314 (2006). URL <https://pubs.acs.org/doi/10.1021/ja054751i>.
- [96] Miyajima, K., Nakajima, A., Yabushita, S., Knickelbein, M. B. & Kaya, K. Ferromagnetism in one-dimensional vanadium-benzene sandwich clusters. *Journal of the American Chemical Society* **126**, 13202–13203 (2004). URL <https://pubs.acs.org/doi/10.1021/ja046151%2B>.

- [97] Morari, C., Allmaier, H., Beiuşeanu, F., Jurcuţ, T. & Chioncel, L. Electronic structure and magnetic properties of metallocene multiple-decker sandwich nanowires. *Physical Review B* **85**, 085413 (2012). URL <https://link.aps.org/doi/10.1103/PhysRevB.85.085413>. 1112.0183.
- [98] Masubuchi, T., Iwasa, T. & Nakajima, A. Multiple-decker and ring sandwich formation of manganese–benzene organometallic cluster anions: $\text{Mn}_n \text{Bz}_n^-$ ($n = 1\text{--}5$ and 18). *Physical Chemistry Chemical Physics* **18**, 26049–26056 (2016). URL <http://xlink.rsc.org/?DOI=C6CP05380G>.
- [99] Zhang, X. & Wang, J. Ab Initio Study of Bond Characteristics and Magnetic Properties of Mixed-Sandwich $\text{V}_n \text{Bz}_m \text{Cp}_k$ Clusters. *The Journal of Physical Chemistry A* **114**, 2319–2323 (2010). URL <https://pubs.acs.org/doi/10.1021/jp907834v>.
- [100] Zhang, X., Tian, Z., Yang, S.-W. & Wang, J. Magnetic Manipulation and Half-Metal Prediction of One-Dimensional Bimetallic Organic Sandwich Molecular Wires $[\text{CpTM}_1 \text{CpTM}_2]_\infty$ ($\text{TM}_1 = \text{Ti, Cr, Fe}$; $\text{TM}_2 = \text{Sc–Co}$). *The Journal of Physical Chemistry C* **115**, 2948–2953 (2011). URL <https://pubs.acs.org/doi/10.1021/jp109253a>.
- [101] Miyajima, K., Knickelbein, M. B. & Nakajima, A. Stern–Gerlach Study of Multidecker Lanthanide–Cyclooctatetraene Sandwich Clusters. *The Journal of Physical Chemistry A* **112**, 366–375 (2008). URL <http://pubs.acs.org/doi/abs/10.1021/jp0766196>.
- [102] Claus, K. H. & Krüger, C. Structure of cyclooctatetraene at 129 K. *Acta Crystallographica Section C Crystal Structure Communications* **44**, 1632–1634 (1988). URL <http://scripts.iucr.org/cgi-bin/paper?S0108270188005840>.
- [103] Karadakov, P. B. Aromaticity and Antiaromaticity in the Low-Lying Electronic States of Cyclooctatetraene. *The Journal of Physical Chemistry A* **112**, 12707–12713 (2008). URL <https://pubs.acs.org/doi/10.1021/jp8067365>.
- [104] Atodiresei, N. *et al.* Controlling the Magnetization Direction in Molecules via Their Oxidation State. *Physical Review Letters* **100**, 117207 (2008). URL <https://link.aps.org/doi/10.1103/PhysRevLett.100.117207>.
- [105] Yao, X., Yuan, S. & Wang, J. Theoretical Studies of Sandwich Molecular Wires with Europium and Boratacyclooctatetraene Ligand and the Structure on a H-Ge(001)- 2×1 Surface. *The Journal of Physical Chemistry C* **120**, 7088–7093 (2016). URL <https://pubs.acs.org/doi/10.1021/acs.jpcc.5b11660>.
- [106] Miyajima, K., Knickelbein, M. B. & Nakajima, A. Magnetic properties of lanthanide organometallic sandwich complexes produced in a molecular beam. *Polyhedron* **24**, 2341–2345 (2005). URL <https://linkinghub.elsevier.com/retrieve/pii/S027753870500361X>.

- [107] Fedushkin, I. L., Bochkarev, M. N., Dechert, S. & Schumann, H. A Chemical Definition of the Effective Reducing Power of Thulium(II) Diiodide by Its Reactions with Cyclic Unsaturated Hydrocarbons. *Chemistry - A European Journal* **7**, 3558 (2001). URL <http://doi.wiley.com/10.1002/1521-3765%2820010817%297%3A16%3C3558%3A%3AAID-CHEM3558%3E3.0.CO%3B2-H>.
- [108] Huttmann, F., Schleheck, N., Atodiresei, N. & Michely, T. On-Surface Synthesis of Sandwich Molecular Nanowires on Graphene. *Journal of the American Chemical Society* **139**, 9895–9900 (2017). URL <https://pubs.acs.org/doi/10.1021/jacs.7b03381>.
- [109] Cao, L., Wang, T. & Wang, C. Synthetic Strategies for Constructing Two-Dimensional Metal-Organic Layers (MOLs): A Tutorial Review. *Chinese Journal of Chemistry* **36**, 754–764 (2018). URL <https://onlinelibrary.wiley.com/doi/10.1002/cjoc.201800144>.
- [110] Urgel, J. I. *et al.* Quasicrystallinity expressed in two-dimensional coordination networks. *Nature Chemistry* **8**, 657–662 (2016). URL <http://www.nature.com/articles/nchem.2507>.
- [111] Parreiras, S. O. *et al.* Tuning the Magnetic Anisotropy of Lanthanides on a Metal Substrate by Metal–Organic Coordination. *Small* **17**, 2102753 (2021). URL <https://onlinelibrary.wiley.com/doi/10.1002/sml1.202102753>.
- [112] Umbach, T. R. *et al.* Ferromagnetic Coupling of Mononuclear Fe Centers in a Self-Assembled Metal-Organic Network on Au(111). *Physical Review Letters* **109**, 267207 (2012). URL <https://link.aps.org/doi/10.1103/PhysRevLett.109.267207>.
- [113] Ovanesyan, N. S., Nikitina, Z. K. & Makhaev, V. D. Ferromagnetism of localized and itinerant electrons in two-dimensional organometallic networks. *Bulletin of the Russian Academy of Sciences: Physics* **81**, 855–859 (2017). URL <http://link.springer.com/10.3103/S1062873817070206>.
- [114] Davisson, C. & Germer, L. H. The Scattering of Electrons by a Single Crystal of Nickel. *Nature* **119**, 558–560 (1927). URL <https://www.nature.com/articles/119558a0>.
- [115] Oura, K., Lifshits, V. G., Saranin, A. A., Zotov, A. V. & Katayama, M. *Surface Science: An Introduction* (Springer Berlin Heidelberg, Berlin, Heidelberg, 2013).
- [116] Binnig, G. and Rohrer, H. Scanning tunneling microscopy. *Helvetica Physica Acta* **55** (1982).
- [117] Fahrenndorf, S. *et al.* Accessing 4f-states in single-molecule spintronics. *Nature Communications* **4**, 2425 (2013). URL <http://www.nature.com/articles/ncomms3425>.

- [118] Voigtländer, B. *Scanning Probe Microscopy*. NanoScience and Technology (Springer Berlin Heidelberg, Berlin, Heidelberg, 2015). URL <http://link.springer.com/10.1007/978-3-662-45240-0>.
- [119] Willmott, P. *An Introduction to Synchrotron Radiation* (2011).
- [120] Rosenberg, R. A., Love, P. J. & Rehn, V. Polarization-dependent C(K) near-edge x-ray-absorption fine structure of graphite. *Physical Review B* **33**, 4034–4037 (1986). URL <https://link.aps.org/doi/10.1103/PhysRevB.33.4034>.
- [121] Rau, I. G. *et al.* Reaching the magnetic anisotropy limit of a 3 d metal atom. *Science* **344**, 988–992 (2014). URL <https://www.science.org/doi/10.1126/science.1252841>.
- [122] Henke, B. L., Knauer, J. P. & Premaratne, K. The characterization of x-ray photocathodes in the 0.1-10 keV photon energy region. *Journal of Applied Physics* **52**, 1509–1520 (1981). URL <http://aip.scitation.org/doi/10.1063/1.329789>.
- [123] Nakajima, R., Stöhr, J. & Idzerda, Y. U. Electron-yield saturation effects in L -edge x-ray magnetic circular dichroism spectra of Fe, Co, and Ni. *Physical Review B* **59**, 6421–6429 (1999). URL <https://link.aps.org/doi/10.1103/PhysRevB.59.6421>.
- [124] Praetorius, C. *XAS and XMCD as Local Probes for Kondo and Heavy Fermion Materials*. Ph.D. thesis, Julius-Maximilians-Universität Würzburg (2015).
- [125] Erskine, J. L. & Stern, E. A. Calculation of the M23 magneto-optical absorption spectrum of ferromagnetic nickel. *Physical Review B* **12**, 5016–5024 (1975). URL <https://link.aps.org/doi/10.1103/PhysRevB.12.5016>.
- [126] Schütz, G. *et al.* Absorption of circularly polarized x rays in iron. *Physical Review Letters* **58**, 737–740 (1987). URL <https://link.aps.org/doi/10.1103/PhysRevLett.58.737>.
- [127] Thole, B. T., Carra, P., Sette, F. & van der Laan, G. X-ray circular dichroism as a probe of orbital magnetization. *Physical Review Letters* **68**, 1943–1946 (1992). URL <https://link.aps.org/doi/10.1103/PhysRevLett.68.1943>.
- [128] Carra, P., Thole, B. T., Altarelli, M. & Wang, X. X-ray circular dichroism and local magnetic fields. *Physical Review Letters* **70**, 694–697 (1993). URL <https://link.aps.org/doi/10.1103/PhysRevLett.70.694>.
- [129] Teramura, Y., Tanaka, A., Thole, B. T. & Jo, T. Effect of Coulomb Interaction on the X-Ray Magnetic Circular Dichroism Spin Sum Rule in Rare Earths. *Journal of the Physical Society of Japan* **65**, 3056–3059 (1996). URL <http://journals.jps.jp/doi/10.1143/JPSJ.65.3056>.

- [130] Collins, S. P., Laundry, D., Tang, C. C. & van der Laan, G. An investigation of uranium M 4,5 edge magnetic X-ray circular dichroism in US. *Journal of Physics: Condensed Matter* **7**, 9325–9341 (1995). URL <https://iopscience.iop.org/article/10.1088/0953-8984/7/48/021>.
- [131] Nolting, F. *et al.* Direct observation of the alignment of ferromagnetic spins by antiferromagnetic spins. *Nature* **405**, 767–769 (2000). URL <http://www.nature.com/articles/35015515>.
- [132] Stöhr, J. . S. H. C. *From Fundamentals to Nanoscale Dynamics* (Springer-Verlag Berlin Heidelberg, Berlin, Heidelberg, 2006).
- [133] Hertz, H. Ueber einen Einfluss des ultravioletten Lichtes auf die electrische Entladung. *Annalen der Physik und Chemie* **267**, 983–1000 (1887). URL <https://onlinelibrary.wiley.com/doi/10.1002/andp.18872670827>.
- [134] Einstein, A. Über einen die Erzeugung und Verwandlung des Lichtes betreffenden heuristischen Gesichtspunkt. *Annalen der Physik* **322**, 132–148 (1905). URL <https://onlinelibrary.wiley.com/doi/10.1002/andp.19053220607>.
- [135] Nobuta, T. & Ogawa, T. Depth profile XPS analysis of polymeric materials by C60 + ion sputtering. *Journal of Materials Science* **44**, 1800–1812 (2009). URL <http://link.springer.com/10.1007/s10853-009-3274-5>.
- [136] Watts, J. & Wolstenholme, J. *An Introduction to Surface Analysis by XPS and AES* (2019).
- [137] Condon, E. U. & Shortley, G. H. *The Theory of Atomic Spectra* (Cambridge University Press, Cambridge, 1935).
- [138] Thole, B. T. *et al.* 3d x-ray-absorption lines and the 3 d 9 4 f n + 1 multiplets of the lanthanides. *Physical Review B* **32**, 5107–5118 (1985). URL <https://link.aps.org/doi/10.1103/PhysRevB.32.5107>.
- [139] Goedkoop, J. B. *et al.* Calculations of magnetic x-ray dichroism in the 3 d absorption spectra of rare-earth compounds. *Physical Review B* **37**, 2086–2093 (1988). URL <https://link.aps.org/doi/10.1103/PhysRevB.37.2086>.
- [140] de Groot, F. & Kotani, A. *Core Level Spectroscopy of Solids*, vol. 168 (CRC Press, 2008). URL <https://www.taylorfrancis.com/books/9781420008425>.
- [141] Retegan, M. Crispy: v0.7.3 (2021). URL <https://dx.doi.org/10.5281/zenodo.1008184>.

- [142] Stavitski, E. & de Groot, F. M. The CTM4XAS program for EELS and XAS spectral shape analysis of transition metal L edges. *Micron* **41**, 687–694 (2010). URL <https://linkinghub.elsevier.com/retrieve/pii/S0968432810001423>.
- [143] Delley, B. privat communication (2021).
- [144] SOLEIL. Deimos Beamline (2021). URL <https://www.synchrotron-soleil.fr/en/beamlines/deimos>.
- [145] Noll, T. & Radu, F. The Mechanics of the Vekmag Experiment. *Proceedings of MEDSI2016* 370–373 (2017).
- [146] BESSYII. VEKMAG (2021). URL https://www.helmholtz-berlin.de/pubbin/igama_output?modus=einzel&sprache=en&gid=1969&typoid=75136.
- [147] Piamonteze, C. *et al.* X-Treme beamline at SLS: X-ray magnetic circular and linear dichroism at high field and low temperature. *Journal of Synchrotron Radiation* **19**, 661–674 (2012). URL <http://scripts.iucr.org/cgi-bin/paper?S0909049512027847>.
- [148] Schumacher, S. *et al.* The Backside of Graphene: Manipulating Adsorption by Intercalation. *Nano Letters* **13**, 5013–5019 (2013). URL <https://pubs.acs.org/doi/10.1021/nl402797j>.
- [149] Kraus, S. *On-surface synthesis of sandwich-molecular wires*. Ph.D. thesis, Universität zu Köln (2021).
- [150] van Gastel, R. *et al.* Selecting a single orientation for millimeter sized graphene sheets. *Applied Physics Letters* **95**, 121901 (2009). URL <http://aip.scitation.org/doi/10.1063/1.3225554>. 0907.3580.
- [151] Friedrich, R., Caciuc, V., Atodiresei, N. & Blügel, S. Molecular induced skyhook effect for magnetic interlayer softening. *Physical Review B* **92**, 195407 (2015). URL <https://link.aps.org/doi/10.1103/PhysRevB.92.195407>.
- [152] Friedrich, R. *et al.* Creating anisotropic spin-split surface states in momentum space by molecular adsorption. *Physical Review B* **96**, 085403 (2017). URL <http://link.aps.org/doi/10.1103/PhysRevB.96.085403>.
- [153] Friedrich, R., Caciuc, V., Atodiresei, N. & Blügel, S. Exchange interactions of magnetic surfaces below two-dimensional materials. *Physical Review B* **93**, 220406 (2016). URL <https://link.aps.org/doi/10.1103/PhysRevB.93.220406>.

- [154] Callsen, M., Caciuc, V., Kiselev, N., Atodiresei, N. & Blügel, S. Magnetic Hardening Induced by Nonmagnetic Organic Molecules. *Physical Review Letters* **111**, 106805 (2013). URL <https://link.aps.org/doi/10.1103/PhysRevLett.111.106805>.
- [155] Baltic, R. *et al.* Superlattice of Single Atom Magnets on Graphene. *Nano Letters* **16**, 7610–7615 (2016). URL <http://pubs.acs.org/doi/10.1021/acs.nanolett.6b03543>.
- [156] Kappert, R. J. H., Vogel, J., Sacchi, M. & Fuggle, J. C. Linear-dichroism studies of thin Dy overlayers on Ni(110) and Cu(110) substrates. *Physical Review B* **48**, 2711–2720 (1993). URL <https://link.aps.org/doi/10.1103/PhysRevB.48.2711>.
- [157] Tripathi, S. XMCD investigation at M_{4,5} edges of the rare earth elements in high-performance permanent magnet. *PhD Thesis* (2018).
- [158] Grånäs, E. *et al.* Oxygen Intercalation under Graphene on Ir(111): Energetics, Kinetics, and the Role of Graphene Edges. *ACS Nano* **6**, 9951–9963 (2012). URL <https://pubs.acs.org/doi/10.1021/nn303548z>.
- [159] Schröder, U. A. *et al.* Core level shifts of intercalated graphene. *2D Materials* **4**, 015013 (2016). URL <http://stacks.iop.org/2053-1583/4/i=1/a=015013?key=crossref.d48154c3b537a0e53e906f8854852f6d>.
- [160] Anderson, N. A., Hupalo, M., Keavney, D., Tringides, M. & Vaknin, D. Intercalated rare-earth metals under graphene on SiC. *Journal of Magnetism and Magnetic Materials* **474**, 666–670 (2019). URL <https://doi.org/10.1016/j.jmmm.2018.11.007.1811.06111>.
- [161] Raman, K. V. *et al.* Interface-engineered templates for molecular spin memory devices. *Nature* **493**, 509–513 (2013). URL <http://www.nature.com/articles/nature11719>.
- [162] Candini, A. *et al.* Spin-communication channels between Ln(III) bis-phthalocyanines molecular nanomagnets and a magnetic substrate. *Scientific Reports* **6**, 21740 (2016). URL <http://dx.doi.org/10.1038/srep21740http://www.nature.com/articles/srep21740>.
- [163] Kraus, S. *et al.* Uniaxially Aligned 1D Sandwich-Molecular Wires: Electronic Structure and Magnetism. *The Journal of Physical Chemistry C* **126**, 3140–3150 (2022). URL <https://pubs.acs.org/doi/10.1021/acs.jpcc.1c10625>.
- [164] Kraus, S. *et al.* Selecting the Reaction Path in On-Surface Synthesis through the Electron Chemical Potential in Graphene. *Journal of the American Chemical Society* **144**, 11003–11009 (2022). URL <https://pubs.acs.org/doi/10.1021/jacs.2c04359>.

- [165] Teramura, Y., Tanaka, A., Thole, B. T. & Jo, T. Effect of Coulomb Interaction on the X-Ray Magnetic Circular Dichroism Spin Sum Rule in Rare Earths. *Journal of the Physical Society of Japan* **65**, 3056–3059 (1996). URL <http://journals.jps.jp/doi/10.1143/JPSJ.65.3056>.
- [166] Pivetta, M. *et al.* Measuring the Intra-Atomic Exchange Energy in Rare-Earth Adatoms. *Physical Review X* **10**, 031054 (2020). URL <https://doi.org/10.1103/PhysRevX.10.031054>.
- [167] Šrut Rakić, I. *et al.* Step-induced faceting and related electronic effects for graphene on Ir(332). *Carbon* **110**, 267–277 (2016). URL <https://linkinghub.elsevier.com/retrieve/pii/S0008622316307758>.
- [168] Goedkoop, J. B. *et al.* Calculations of magnetic x-ray dichroism in the 3 d absorption spectra of rare-earth compounds. *Physical Review B* **37**, 2086–2093 (1988). URL <https://link.aps.org/doi/10.1103/PhysRevB.37.2086>.
- [169] Kraus, S. privat communication (2021).
- [170] Atodiresei, N. privat communication (2021).
- [171] Vinogradov, N. A. *et al.* Controllable p-doping of graphene on Ir(111) by chlorination with FeCl₃. *Journal of Physics: Condensed Matter* **24**, 314202 (2012). URL <https://iopscience.iop.org/article/10.1088/0953-8984/24/31/314202>.
- [172] Herper, H. C., Vekilova, O. Y., Simak, S. I., Di Marco, I. & Eriksson, O. Localized versus itinerant character of 4f-states in cerium oxides. *Journal of Physics: Condensed Matter* **32**, 215502 (2020). URL <https://iopscience.iop.org/article/10.1088/1361-648X/ab6e92>.
- [173] Lebens-Higgins, Z. W. *et al.* Distinction between Intrinsic and X-ray-Induced Oxidized Oxygen States in Li-Rich 3d Layered Oxides and LiAlO₂. *The Journal of Physical Chemistry C* **123**, 13201–13207 (2019). URL <https://pubs.acs.org/doi/10.1021/acs.jpcc.9b01298>.
- [174] Schumacher, S. *et al.* Polar EuO(111) on Ir(111): A two-dimensional oxide. *Physical Review B* **89**, 115410 (2014). URL <https://link.aps.org/doi/10.1103/PhysRevB.89.115410>.
- [175] Hepperle, P. *et al.* XPS Examination of the Chemical Composition of PEG-MUA[U+2010]Coated Gold Nanoparticles. *Particle Particle Systems Characterization* 2200070 (2022). URL <https://onlinelibrary.wiley.com/doi/10.1002/ppsc.202200070>.

- [176] Giljohann, D. A. *et al.* Gold Nanoparticles for Biology and Medicine. *Angewandte Chemie International Edition* **49**, 3280–3294 (2010). URL <https://onlinelibrary.wiley.com/doi/10.1002/anie.200904359>.
- [177] Carnovale, C., Bryant, G., Shukla, R. & Bansal, V. Identifying Trends in Gold Nanoparticle Toxicity and Uptake: Size, Shape, Capping Ligand, and Biological Corona. *ACS Omega* **4**, 242–256 (2019). URL <https://pubs.acs.org/doi/10.1021/acsomega.8b03227>.
- [178] Li, W. *et al.* Intercomparison of dose enhancement ratio and secondary electron spectra for gold nanoparticles irradiated by X-rays calculated using multiple Monte Carlo simulation codes. *Physica Medica* **69**, 147–163 (2020). URL <https://linkinghub.elsevier.com/retrieve/pii/S1120179719305320>.
- [179] Johannsen, S. *et al.* Spin Crossover in a Cobalt Complex on Ag(111). *Angewandte Chemie International Edition* **134**, 1–8 (2022). URL <https://onlinelibrary.wiley.com/doi/10.1002/anie.202115892>.

DuEPublico

Duisburg-Essen Publications online

UNIVERSITÄT
DUISBURG
ESSEN

Offen im Denken

ub

universitäts
bibliothek

Diese Dissertation wird via DuEPublico, dem Dokumenten- und Publikationsserver der Universität Duisburg-Essen, zur Verfügung gestellt und liegt auch als Print-Version vor.

DOI: 10.17185/duepublico/76606

URN: urn:nbn:de:hbz:465-20220909-120214-1

Alle Rechte vorbehalten.